AN ELECTRICAL MICROCYTOMETER FOR PORTABLE BLOOD ANALYSIS IN GLOBAL HEALTH APPLICATIONS

BY

NICHOLAS NOEL WATKINS

DISSERTATION

Submitted in partial fulfillment of the requirements
for the degree of Doctor of Philosophy in Electrical and Computer Engineering
in the Graduate College of the
University of Illinois at Urbana-Champaign, 2012

Urbana, Illinois

Doctoral Committee:

Professor Rashid Bashir, Chair
Professor Brian Cunningham
Professor Kanti Jain
Adjunct Professor William Rodriguez, Harvard Medical School;
CEO, Daktari Diagnostics

ABSTRACT

For three decades the AIDS (Acquired Immune Deficiency Syndrome) pandemic has killed millions and currently affects tens of millions around the world. It has especially crippled resource-poor regions in the world such as sub-Saharan Africa, which contains two-thirds of the world's people living with AIDS. Antiretroviral therapy (ART) to combat the human immunodeficiency virus (HIV) has become more accessible to patients in these regions over the past several years, and has shown to improve the quality of their lives. However, the lack of objective diagnostics—CD4+ T lymphocyte counts—to determine when to start ART and to monitor its success hinders the effective use of treatment in these regions. The industry standard of flow cytometry to obtain CD4+ T cell counts is too taxing on the debilitated healthcare infrastructure of undeveloped nations because of its high cost, technical demands, and lack of portability. Therefore, there is an urgent need to develop a portable, robust, and affordable point-of-care (PoC) CD4+ T cell counter that can reach all HIV/AIDS patients, regardless of geography or socio-economical situation.

This dissertation addresses this great need through investigation of a miniaturized, portable PoC platform that can provide CD4+ T cell counts in less than 15 minutes. Standard microfabrication techniques have been used to create a microfludic biochip, which uses electrical impedance sensing to analyze small sample volumes ($\sim$10 μL) of blood. The biochip progressively gains more functionality during the study. First, a chip was designed to confirm that the electrical impedance pulse counting technique was a viable method to enumerate CD4+ T cells. Three-dimensional hydrodynamic focusing was used to take advantage of the laminar flow regime found in microfludics and increase the counting accuracy of the device. Second, a differential counting stage was added that selectively counted CD4+ T cells from leukocyte (*i.e.*, white blood cell) populations using immunoaffinity chromatography meth-

ods. Total leukocyte counts were obtained before and after the cells flowed through a CD4+ T cell depletion chamber. The difference between these two counts proved to be an accurate representation of the number of captured cells when verified with an optical control. Third, an erythrocyte (*i.e.*, red blood cell) lysis module was added, with which to perform accurate counts on unprocessed blood samples, verified with flow cytometry controls. The success of this final stage suggests that the technology described is a viable answer to bringing PoC CD4+ T cell counts into resource-poor regions. An advantage of this label-free technology is that it can be readily expanded to diagnose other diseases and conditions simply by altering the specificity of its depletion chambers to other cell types.

Although this dissertation focuses on the specific application of PoC AIDS diagnostics, it also addresses the fundamentals in microfluidic cytometry. The impedance responses of cells under various conditions were studied, including living cells, dead/dying cells, and cells undergoing chemical modification. Leukocyte subsets were distinguished based on their electrical properties found using multiple AC interrogation frequencies, confirming state-of-the-art findings in the literature. This multiple frequency technique gave a better understanding of the morphological and electrical characteristics of leukocytes, such as cell volume and membrane capacitance. Different electrical sensor designs were investigated to increase sensitivity and signal integrity, and to know cell flow direction through the counter. Various sensing channel designs were explored to determine the optimal balance between counting accuracy and fabrication complexity.

ACKNOWLEDGMENTS

First of all, I would like to thank my adviser, Professor Rashid Bashir, for his guidance, support, and friendship throughout my PhD studies. His passion for solving health problems using BioMEMS attracted me to his group and has opened up a world of possibilities for me to use my skills to help those in need. I am thankful for his discussion of various ideas in research, sharing wisdom regarding my future professional career, and discussing life's philosophies.

I acknowledge my doctoral committee members, Professor Brian Cunningham, Professor Kanti Jain, and Dr. William Rodriguez, for their involvement in my research and offering invaluable advice and suggestions to help broaden my view of research. I thank Professor Xuanhong Cheng from Lehigh University for sharing her insight, wisdom, and time in helping me better understand the dynamics of her previous research in CD4+ T cell capture and enumeration.

I would like to thank my colleagues in Professor Bashir's group who have been a source of friendship, support, wisdom, and lively discussions about research and non-research topics. I thank Gregory Damhorst, Umer Hassan, Jimmy Nee, Supriya Sridhar, Nicholas Won, Anna Czapar, and Adil Aghafor (Purdue University) for their direct involvement and assistance in my research. I especially would like to acknowledge Dr. Yi-Shao Liu, Bobby Reddy, Jr., Vincent Chan, Piyush Bajaj, and Dr. Kidong Park, as they transferred over to the University of Illinois from Purdue University with me, and have been with me for the major part—if not all—of my doctoral journey.

I acknowledge Sue Groves, Kelly Dyer, and others at the Carle Foundation Hospital Laboratory, who have graciously helped in providing control tests for my experiments. I also thank Breanne Stillwell, Pam Woo, and Dixie Heath at Carle's Research Tissue Repository, who helped provide convenient

phlebotomy services during a crucial period in my research. I also acknowledge Dr. Barbara Pilas at the University of Illinois Flow Cytometry Facility for sharing her help and wisdom in the practical and theoretical aspects of flow cytometry.

I thank my parents, Noel and Anne Watkins, for their continued support through my time in graduate school. Their prayers, encouragement, wisdom, and love helped boost my morale and carry me through the doldrums and difficulties inherent to graduate studies. I thank my sister, Stephani Sherman, for her encouraging spirit and support and my nephews, Scotty and Riley, for their enthusiasm and joy that helped cheer me up. I thank my wife's parents, Michael and Joyce Belobraydich, and her sisters, Rebecca and Corrie Belobraydich, for their encouraging words, kindness, friendship, and hospitality—the best in-laws anyone could ask for. I thank Marshall Crocker for his friendship and companionship going back to my days at Mississippi State Univeristy, and for helping me not take life too seriously. I acknowledge Chun-Li Chang and Helen Pai for their great friendship, kindness, and hospitality during my time at Purdue University and afterwards. I would like to thank David Krehbiel, Dr. Yuechao Zhao, and others at TCBC for their continued friendship and prayers during my time at the University of Illinois.

I give my deepest thanks to my lovely wife, Alysia, for her love, patience, prayers and support during the sometimes stressful portions of my doctoral studies—especially near the end. She made great sacrifices to support our family by adjusting to the hectic and eccentric lifestyle of a doctoral student, and I could not have made it without her companionship. I also thank our beautiful daughter, Eliana, for her joyful laughs, energy, and squeals of delight, which remind me there is life outside of the laboratory.

Finally, I thank my Creator for giving me the opportunity and the faculties to succeed in performing research at a world-class institute in the University of Illinois. I thank Him for the support and encouragement through the many people that he has placed in my life, and for showing me how to do things excellently through His example (Collosians 3:17, I Peter 2:21).

TABLE OF CONTENTS

CHAPTER 1

INTRODUCTION

The need for a portable AIDS (Acquired Immune Deficiency Syndrome) diagnostics platform is a crucial problem. Since its discovery in the early 1980s, AIDS has grown from a few isolated incidents to a pandemic that is currently affecting the lives of over 33.4 million people around the world. Sub-Saharan Africa has been hit hardest by the AIDS pandemic: it comprises 67% (22.4 million) of all infections and 70% (1.4 million) of annual deaths [1]. One of the major reasons for these staggering statistics besides the lack of education on the disease (e.g., its symptoms, how it is transmitted[1], and how to protect against transmission) is poor healthcare infrastructure from poverty. The governments within this region do not have the financial resources to pay for expensive equipment, facilities, and labor hours required to accurately detect and analyze the progression of HIV in millions of potential patients. In addition, only 3% of the world's healthcare workers are in this region, which contains 25% of the world's global burden of disease [2]. This problem is only compounded by the fact that 2 out of 3 inhabitants live in rural areas, unable to travel to urban sites that would provide these facilities and services [3]. The current situation is bleak: understaffed single-room facilities with inadequate equipment, resulting in inaccurate tests for only a fraction of those patients who need them. Antiretroviral therapy (ART) that uses a cocktail of drugs has been shown to improve the quality of life for those infected with the Human Immunodeficiency Virus (HIV), and global efforts increased the accessibility of such treatment 30-fold in sub-Saharan Africa between 2003 and 2008 [4–6]. However, the lack of objective diagnostic tests to determine when to start ART and to monitor its success hinders the effective use of treatment. Absent appropriate diagnostic tests, clinicians may rely on less accurate assessments, ranging from self-described symptoms or insensitive

[1]Known methods of HIV transmission: sexual intercourse, blood transfer, sharing needles, perinatal, and breast feeding.

laboratory tests. For example, patients undergoing treatment are asked a series of questions regarding how they feel to determine the effectiveness of the drug combination and how severe are the side effects—so-called "clinical monitoring." A quantitative test that is administered more frequently is necessary to maximize the effectiveness of the treatment and minimize detrimental side-effects.

An important quantitative HIV/AIDS diagnostic procedure is to obtain a patient's CD4+ T lymphocyte count [7–9]. CD4+ T lymphocytes, or simply CD4+ T cells[2], are a subset of leukocytes (*i.e.*, white blood cells) whose concentration has been shown to be inversely proportional to the progression of HIV in human patients. Flow cytometers using laser light scattering and laser-induced fluorescence principles are the current gold standard to provide accurate CD4+ T cell counts at high throughputs. However, the cost ($40,000 to over $125,000), technical operator and maintenance requirements, and lack of portability of such instruments are too taxing for the debilitated healthcare infrastructures of resource-poor regions.

A complementary approach to flow cytometry is to obtain the concentration of HIV RNA in human blood, known as a viral load test. This test, in conjunction with the CD4+ T cell count test, gives healthcare providers a better look at the current and future state of a patient's immune system, allowing for optimal secondary prophylaxis with ART. However, viral load tests demand the same resources as mentioned for the flow cytometers, and have also failed in penetrating developing regions of the world.

This problem has led to the investigation, detailed in this dissertation, of a miniaturized platform that would complement sub-Saharan Africa's (and any resource-poor region's) healthcare infrastructure: a portable, hand-held CD4+ T cell enumeration device that could be easily transported and operated by minimally trained workers even in the most desolate regions in Africa. This is realized using industry-standard microfabrication methods to create a microfluidic biochip that electrically counts the cells using samples only the size of a drop of blood ($\sim$10 μL). An initial biochip was developed to test whether electrically counting cells in a microfluidic environment was feasible. An improved biochip was then developed that showed the feasibility of selectively counting CD4+ T cells from a heterogenous population of

[2]Other common names for CD4+ T lymphocytes are CD4+ T cells and helper T cells.

leukocytes. A third and final chip was developed to selectively count CD4+ T cells from whole blood samples with the addition of a sample preparation module. The module, integrated within the chip, created a purified population of leukocytes by selectively lysing all erythrocytes (*i.e.*, red blood cells), which is crucial for accurate electrical CD4+ T cell enumeration.

This document is comprised of six chapters, including this introduction. Chapter 2 gives a succinct background on the mechanics of HIV/AIDS, the theory behind current methods and technologies used to diagnose and treat the disease. It then examines current trends in point-of-care (POC) HIV/AIDS diagnostics, focusing on microfluidic technologies with emphasis on electrical sensing methods. Figure 1.1 illustrates the content of the remaining chapters. Chapter 3 details the initial approach in portable HIV/AIDS diagnostics via a microfabricated electrical cell counter that uses 3-dimensional hydrodynamic focusing to increase the accuracy of the cell counts for purified CD4+ T cell populations. Chapter 4 shows the steps used to realize a chip that can selectively enumerate CD4+ T cells from purified leukocyte populations using an electrical differential counting technique. Chapter 5 provides the details in designing, fabricating, and testing the final chip design that enumerates CD4+ T cells from 10 μL whole blood samples via an additional erythrocyte lysis module—suggesting the differential counting technique is a valid approach to POC HIV/AIDS diagnostics. Future work, describing improvements on and expansion of the final differential counter, is listed in Chapter 6. Expansions considered are multiplexing the differential counting technique to simultaneously provide CD4+ and CD8+ T lymphocyte counts and to provide a complete blood count (CBC) of all major blood cell populations.

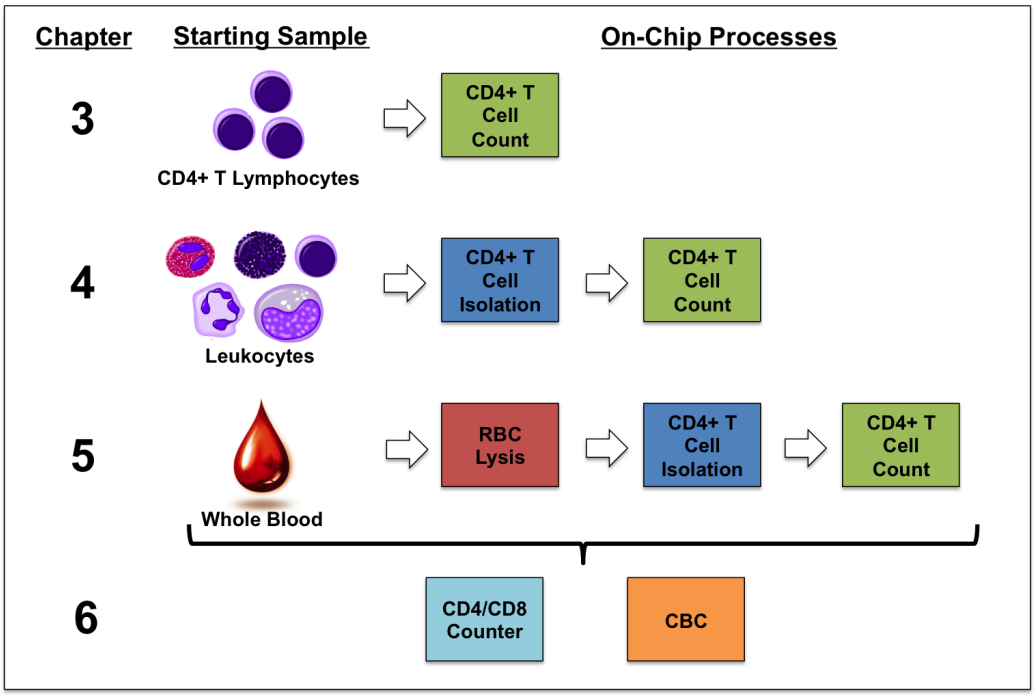

Figure 1.1: Graphical illustration of content covered in Chapters 3 – 6, showing the starting sample and subsequent on-chip processing to obtain CD4+ T cell counts. Chapter 6 proposes the expansion of the device described in Chapter 5 to realize a CD4+ and CD8+ T cell counter and a complete blood counter (CBC).

CHAPTER 2

METHODS IN AIDS DIAGNOSTICS

2.1 Introduction

This chapter provides a brief summary behind the mechanism of HIV infection and its deleterious effects on the human immune system. Current industry standards for AIDS analysis are discussed, followed by the most recent research in microfabricated lab-on-a-chip (LOC) systems, with special emphasis placed on electrical methods. A brief history of and theory behind electrical impedance sensing in fluidics will also be explored.

2.2 Composition of Human Blood

Blood is the essential substance in an organism that provides the necessary functions to sustain life through its circulatory system. Some of its most important functions include supplying oxygen and necessary nutrients to and removal of waste products from tissues and organs, regulating body temperature, supplying a chemical messaging pathway (e.g., hormonal secretion), and providing immunological response to pathogens, such as viruses and bacteria. These various functions make blood an extremely complex fluid: 55% is comprised of serum that contains thousands of different proteins that range in concentrations across 9 orders of magnitude ($mg{\cdot}mL^{-1}$ to $pg{\cdot}mL^{-1}$) [10] and the remaining 45% contains various blood cells of varying size, function, and concentrations. Table 2.1 notes the several different types of blood cells and their concentrations in healthy adult blood. Erythrocytes, or red blood cells (RBCs), are by far the most numerous of the blood cells and help transport carbon dioxide and oxygen to and from the lungs, respectively. Thrombocytes, or platelets, help stop bleeding by forming clots around wounded blood

vessels. Leukocytes, or white blood cells (WBCs), form the immune system, the body's dynamic and multi-layered defense system which protects against disease by attacking pathogens such as viruses, bacteria, fungi, and any other foreign entity. Special attention is directed toward one particular leukocyte, the helper T cell, which will be the main focus for the remainder of this chapter.

Table 2.1: Cell content of human blood. Concentrations and % total WBCs data are for healthy adults.

Cell Type	Main Functions [11]	#/μL [11]	Diameter (μm) [12]	% Total WBCs [12]
Erythrocytes (RBCs)	transport O_2 and CO_2	$5x10^6$	6–8	—
Thrombocytes (platelets)	initiate blood clotting	$3x10^5$	2–3 [13]	—
Leukocytes (WBCs)	immune defense	$4–11x10^3$	7–21	—
Neutrophils	phagocytose and destroy invading bacteria	$5x10^3$	10–12	54–62% [14]
Eosinophils	destroy larger parasites and modulate allergic inflammatory responses	$2x10^2$	10–12	1–6%
Basophils	release histamine in certain immune reactions	$4x10^1$	12–15	<1%
Monocytes	differentiate into tissue resident macrophages or dendritic cells	$4x10^2$	14–17	2–10%
Lymphocytes	(see below)	$3x10^3$	7–8	25–33%
B Cells	make antibodies	$2x10^3$	7–8	16–22%
T Cells	kill virus-infected cells and regulate activities of other leukocytes	$1x10^3$	7–8	8–11%
Natural Killer Cells	kill virus-infected cells and some tumor cells	$1x10^2$	7–8	0.8–1.1%

Helper T cells play a crucial role in the adaptive nature of the immune system by activating and directing other leukocytes toward a particular pathogen. Pathogens such as viruses and bacteria express particular proteins on their surfaces (antigens) that may be recognized by complementary proteins (antibodies) distributed throughout the blood. The antibodies specifically attach to the antigens, neutralizing the pathogens' attack method, eventually leading to the elimination of the pathogens by the immune system. If an invading pathogen containing antigens not known to the immune system, antigen presenting cells (APCs), such as macrophages, dendritic cells,

or B cells, engulf and digest (a process called phagocytosis) the pathogen and present the pathogen's epitope (portion of its antigen that is recognized by the immune system) to immature T cells within the lymph nodes. This activation process requires the use of two surface proteins on the T cell membrane, the T cell receptor (TCR) and the CD4 (cluster of differentiation 4) co-receptor, which amplifies the sensitivity of the interaction between the TCR and the epitope presented by the antigen presenting cell [15]. Through this process, the T cells learn about new pathogens, mature into helper T cells, and proliferate to effectively memorize the antigen to prepare for future invasions. Already mature Helper T cells (also called CD4 T cells because of their aforementioned CD4 co-receptors) will recognize this antigen on the surface of a B cell and activate the B cell to start producing antibody to the antigen.

2.3 Mechanisms Behind HIV/AIDS

HIV, more specifically HIV-1[1], is a retrovirus that is transmitted via bodily fluids (e.g., unprotected sexual intercourse, blood, breast milk, and vertical transmission from mother to child at birth). Once it enters the bloodstream, it targets the CD4 proteins expressed on leukocytes, such as macrophages, monocytes, dendritic cells, and especially helper T cells, which express substantially more of the protein on their surfaces. Figure 2.1 illustrates how HIV infects a CD4 T cell and uses the cell to replicate for viruses. Initially, an HIV virion attaches to the surface of the cell via the virus' gp120 protein, which complements the cell's CD4 receptor. This interaction facilitates further interaction of gp120 with other cell surface proteins, called chemokine receptors, creating a more substantial attachment. This allows HIV's gp41 protein to penetrate the cell's membrane. Subsequent folding of gp41 brings the virion close enough to fuse to the cell's membrane. This fusion delivers the virus' ribonucleic acid (RNA) and essential enzymes necessary for virus replication by the cell. The reverse transcriptase enzyme creates complementary single-stranded DNA (cDNA, or complementary deoxyribonucleic acid)

[1]Currently, two strains of HIV have been discovered, but HIV-1 is more common throughout the world and more heavily studied (HIV-2 is localized to West Africa as it is less infectious [16]).

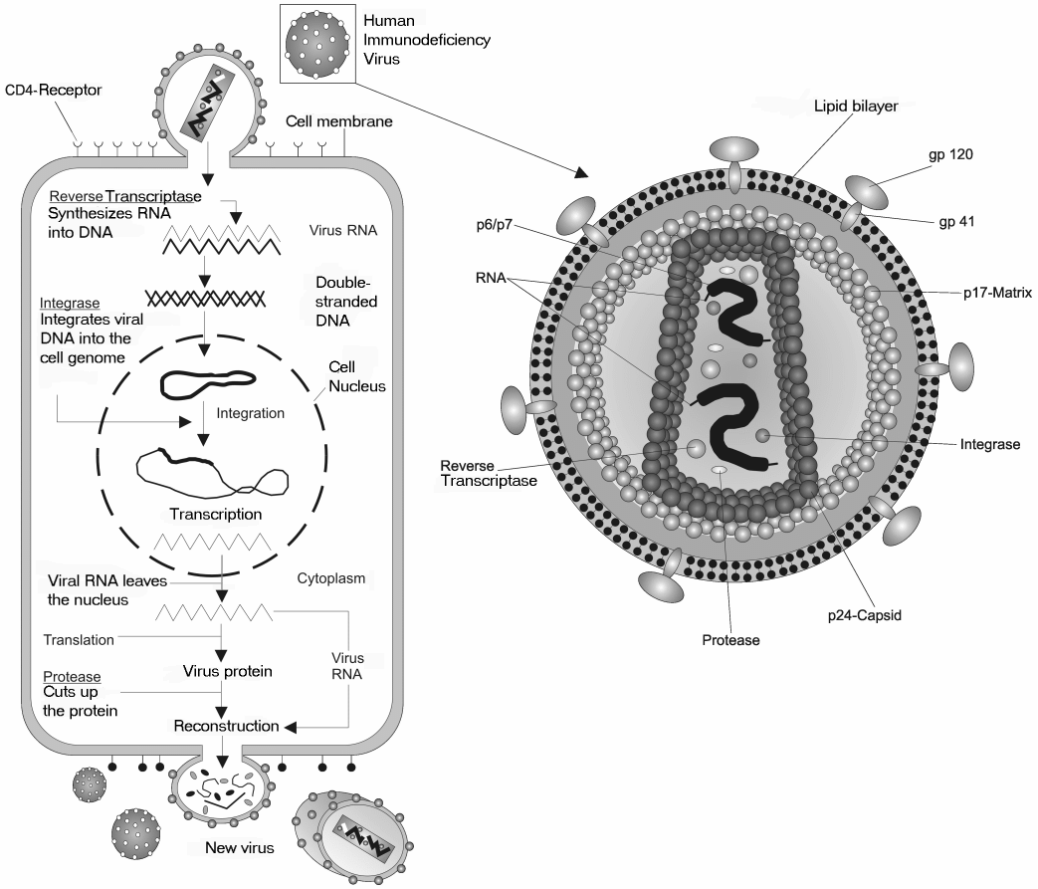

Figure 2.1: Mechanism in which an HIV virus infects a CD4 T cell, causing it to replicate more viremia [20].

which is then turned into double-stranded DNA (dsDNA) by the polymerase enzyme. Integrase then transfers the viral dsDNA into the cell nucleus and integrates it into the host cell's genome. This hijacks the cell to translate the viral genes through the same processes the cell uses to synthesize proteins. The virus proteins and newly replicated RNA are reconstructed into viral capsids that attach to the inner side of the cell's plasma membrane. Eventually, the newly constructed virus buds out through the cell membrane, ready to infect another CD4 T cell [17–19].

This process not only kills the host cells by increasing the likelihood of apoptosis (programmed cell death), but also triggers an immune response in the form of cytotoxic T cells, which kill the HIV-infected cells. The continual decimation of helper T cells will eventually lead to death of the individual because the essential role these cells have in the immune system. In reality, HIV does not directly kill a patient, but weakens the immune system enough

so that an opportunistic pathogen—that may be handled easily by a healthy immune system—would eventually cause death. For this reason, the Centers for Disease Control (CDC) defined AIDS as the point when the immune system cannot support itself, specifically when a patient has less than 200 CD4 T cells per microliter (cubic mm) of blood [21]. Without aid, a patient would soon die in the case of an opportunistic infection.

Figure 2.2 illustrates the relationship between the HIV viral load content (concentration of viral RNA in the blood) and the number of CD4 T cells throughout a patient's life since HIV acquisition. CD4 T cells start decreasing rapidly, even before the large spike in HIV viremia. Initially, the immune system responds to the infection and causes a sharp decrease in the number of HIV viremia. This results in a latent, chronic infection—a battle between the virus and host immune system that generally is waged for 8 to 10 years. Eventually, the helper T cell concentration becomes so low that the immune system cannot defend against opportunistic infections. This, coupled with rapid production of HIV viremia, causes death.

The availability of antiretroviral treatment (ART) continues to increase throughout the developing world. These drugs have proven to have a dramatic impact on health by specifically hindering HIV's aforementioned replication mechanisms [22]. For example, one drug may inhibit the attachment of HIV to the cell membrane, another would prohibit the reverse transcription of viral RNA into cDNA, and another may prevent the creation of viral proteins that would construct the new viral capsid. As a result, it is necessary to find the optimum combination of antiretroviral drugs to severely dampen the proliferation of HIV. This requires periodic and quantitative monitoring of a patient's immune system, which is not currently feasible in developing regions, especially sub-Saharan Africa.

2.4 Current AIDS Diagnostics Methods

Comprehensive diagnostic testing in HIV care involves three tests. A patient who is in a high-risk group for HIV or may have been exposed to HIV is screened for the presence of antibodies to HIV. These antibodies are created by the immune system in response to the presence of HIV, and can be detected in either blood or saliva. The antibodies may also be detected in

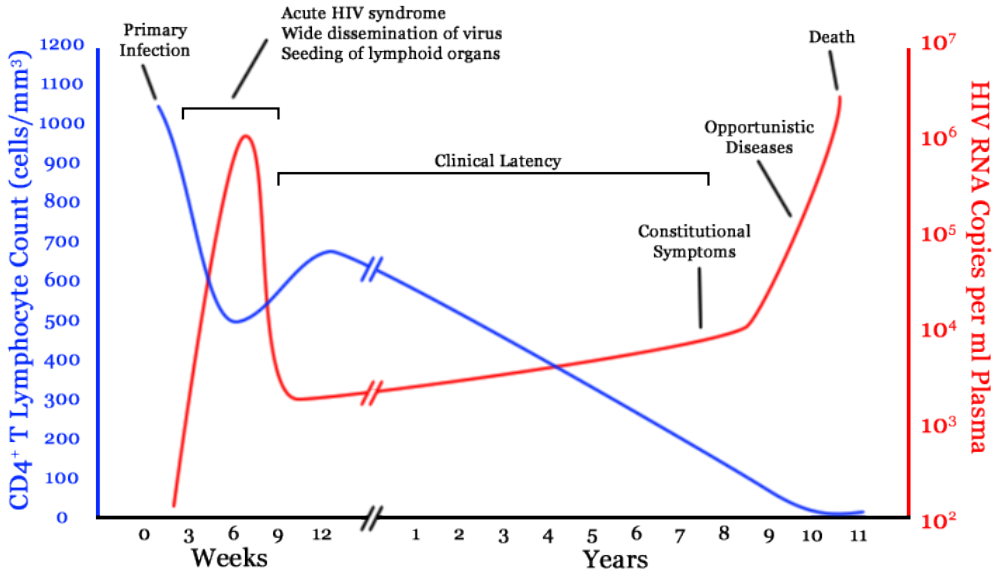

Figure 2.2: Common pattern of relationship between the concentration of CD4 (helper) T cells and HIV viral load over the life of individual. Adapted from [23].

urine, but this has proven more difficult. The antibody test may be coupled with other tests for confirmation, such as the Western Blot which uses gel electrophoresis to sense the proteins, directly testing for the HIV p24 antigen, and even a viral load test (see below) [24]. These tests serve as qualitative methods to determine the presence of HIV, and cannot give more information regarding the current state of a patient's immune system.

Ideally, once it is confirmed that a patient has contracted HIV, two tests are administered periodically: an absolute CD4 T cell count and a HIV viral load count. These tests are usually run in tandem, giving clinicians valuable quantitative information about the health of a patient's immune system (Fig. 2.2), enabling them to provide a tailored and optimized ART regimen. The following subsections detail each method.

2.4.1 Viral Load Test

A viral load test is used to estimate the concentration of circulating HIV in blood. Since the goal of ART is to reduce the amount of HIV in a patient, a viral load test gives a direct look at the effectiveness of treatment. All approved methods estimate HIV progression by quantifying the amount of viral RNA in

a known volume of blood (usually in units of RNA copies per mL). Currently, three proprietary methods exist: (1) using reverse-transciptase PCR (RT-PCR) to amplify the RNA (Amplicor® HIV-1 Monitor™by Roche) [25], (2) nucleic acid signal-based amplification (NASBA) using fluorescent beacons that only fluoresce when attached to viral RNA (NucliSens® HIV-1 QT by bioMerieux) [26, 27], and (3) specific immobilization of viral RNA and subsequent attachment to branched DNA (bDNA) fragments linked to light-emitting enzymes (Versant® HIV-1 RNA by Bayer) [28]. It has been reported that the aforementioned tests have the following detection limits: (1), 200 copies·mL^{-1} [27]; (2), 176 copies·mL^{-1} [29]; and (3), 500 copies·mL^{-1} [27]. These limits are the smallest detectable number of RNA copies, and show that these tests are capable of detecting the progress of HIV at its earliest stages and during effective ART.

The main reasons these testing systems have not penetrated the African continent successfully are their high cost ($15,000–35,000 for equipment and as much as $100 per patient test), need for special laboratory space, and requirement of highly-trained personnel in molecular biology. These requirements cannot be met by resource-poor regions; as a result, viral load tests are seldom used [30].

2.4.2 Absolute CD4+ T Cell Count

Helper T cells are enumerated using flow cytometers—the industry standard for cellular analysis—which use optical interrogation to analyze cell populations a single cell at a time. Figure 2.3 illustrates the fundamental components of a flow cytometer. Cell populations are hydrodynamically-focused into a single-file line to ensure cells are individually analyzed. Each cell is then optically interrogated by laser light as it passes through an aperture. This passage causes a perturbation in the light which is quantified by sensitive photodetectors through optical filters to determine a cell's various characteristics, which are saved in a data structure on a computer. Laser light scattering (LLS) is one perturbation that can determine a cell's size, current phase in growth cycle, and DNA content by observing the amplitude and direction that an applied laser light is scattered onto photodetectors [31]. For example, the amplitude of the forward scattering (FSC) photodetector

signal is generally proportional to a cell's size, while side scattering (SSC) signal from its photodetector determines the interior complexity of a cell (*e.g.*, nucleus and other organelles). Figure 2.4(a) illustrates how plotting FSC vs. SSC can discriminate among different cell and particle populations. Laser-induced fluorescence (LIF) is an important concept in flow cytometry that can be used to complement LLS [32–35]. One or more lasers of different wavelengths (colors) are used to excite fluorescent markers that specifically attach to a particular cell's surface receptor proteins. Each cell line has a unique combination and concentration of these receptors on its surface (this is similar to identifying a person via fingerprints). Therefore, a specific cell type can be determined by the intensity and color of fluorescent markers that specifically attach to a cell's surface receptors. This is shown in Fig. 2.4(a), where a helper T cell can be identified solely by fluorescence by three markers with three different colors. CD45 denotes the cell as a leuokocyte, CD3 narrows it down to a type of T cell, and CD4 ensures it is a helper T cell (or CD4+ T lymphocyte). Figures 2.4(b–d) illustrate the concept of isolating the helper T cell population using a combination of LLS and LIF gating: (b) Lymphocytes are isolated using the FSC vs. SSC plot, (c) only CD3+ lymphocytes (T cells) are selected from the total lymphocyte populations, and (d) helper T cells are identified as being CD4+ and CD14-. With the addition of fluorescent counting beads of a known concentration, it is possible to find the concentration of helper T cells in whole blood. The standard procedure for finding helper T cell concentration is to add fluorescent beads of a known concentration to the sample, and compare the number of helper T cell events to the bead events. A healthy adult will have approximately 600–1,000 helper T cells per microliter of blood, while someone infected with HIV, if not receiving treatment, will have counts less than 500, and eventually below 200—at which he or she would technically have AIDS.

Other forms of analysis can be performed to give an idea about a patient's health besides an absolute CD4 T cell count, such as finding the ratio of CD4+ T cells to CD8+ T cells, and finding the percentage of CD4+ T cells out of total lymphocytes or the entire white blood cell population. However, the current standard set by the World Health Organization emphasizes the absolute CD4 count.

Flow cytometry provides a versatile, accurate, and high-throughput platform for the diagnostics of AIDS. However, like viral load testing methods,

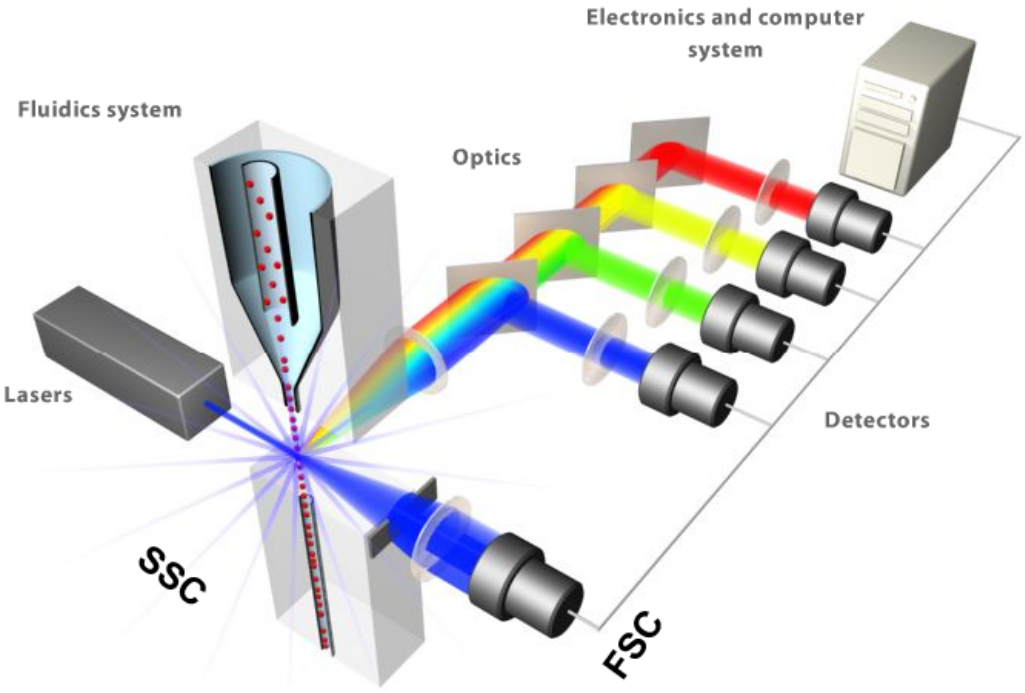

Figure 2.3: Components of a flow cytometer with laser light scattering and laster-induced fluorescence capabilities. Adapted from [36].

flow cytometry requires resources that hinders its penetration in developing nations [37]. They have a high initial cost (some approaching $125,000), need periodic maintenance (contracts can be $10,000/year) and repair, require operation by a trained technician, and lack portability due to sheer size, weight, and fragile optical components. Effort has been made to reduce the complexity, size, and cost of these machines to be more amenable for diagnostics in resource-poor regions. Table 2.2 lists some of the available systems with their cost, estimated cost per test, estimated throughput, and weight.

i+Med Laboratories offers a CD4+Select^{TM} reagent which provides CD4+ T cell counts and percentages at ∼$7 per test. Although it does not need a flow cytometer, it still requires the use of an automated hematology analyzer which can have an average cost of ∼$10,000 and a similar size to the products listed in Table 2.2 [39]. Depending on the analyzer used and number of technicians available, the throughput could be as high as 480 samples per eight-hour day.

Although an improvement, the listed systems still fall short in meeting the

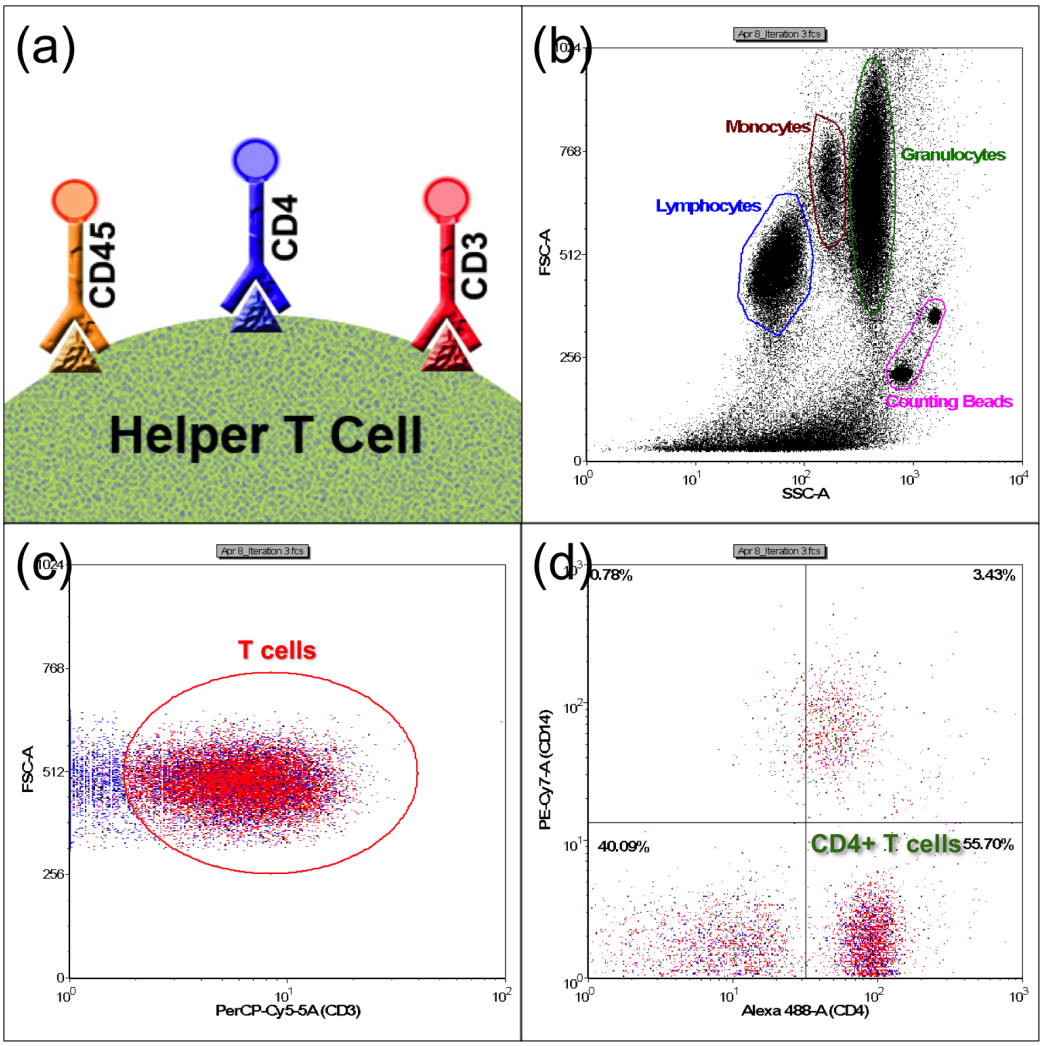

Figure 2.4: Concept of identifying helper T cells in whole blood samples (with lysed red blood cells): (a) the unique combination of surface markers coupled with fluorescent markers helps identify the helper T cell; (b) different white blood cell subsets can be discriminated in the FSC vs. SSC plot; (c) lymphocytes with CD3 marker attached are selected, denoting them as T cells; (d) different subsets of T cells are discovered by plotting CD4 vs. CD14 intensities, where helper T cells are CD4+ and CD14-.

Table 2.2: Specialized CD4 T cell enumeration systems currently available.

Product/ Manufacturer	System Cost	Cost/Test	Tests/Day	System Weight (lbs)
FACSCount/ Becton-Dickinson	$30,000	$5	300+	57
EasyCD4/ Guava Tech.	$45,000	$3	100–150	35
PointCare NOW/ PointCare Tech.	$15,000–20,000	$10	75	26.5
CyFlow SL_3/ Partec	$22,000	$2 [38]	250	33

needs for the undeveloped healthcare infrastructure of sub-Saharan Africa, as they are still too expensive, require maintenance and trained professional operators, and are too bulky and fragile to be portable. As a result, a truly mobile and accurate CD4 T cell enumeration platform that can reach all patients, regardless of geography and economic status, does not exist.

Manual CD4+ T cell counting options have been available for several years. Beckman Coulter offers a Coulter® Manual CD4 Count Kit (*i.e.*, "Cytospheres") which specifically labels CD4+ T cells with beads that are visible under a light microscope for ∼$11 per test. Invitrogen offers magnetic Dynabeads® which specifically attach to CD4+ T cells. With the help of an external magnet, the bead-cell complexes are separated from other cells and are counted under a light microscope for a per test cost of ∼$4. Although these tests are relatively inexpensive and provide CD4+ T cell counts which reasonably correlate with the flow cytometry standard, they still require a laboratory setting with a dependable electricity source (for the microscope and refrigerated storage) and skilled technicians. In addition, manual counting under a microscope is not only tedious and error-prone, but the time-consuming activity also has a low test throughput [40].

2.5 Lab-on-a-Chip Platforms for Global Health Diagnostics

For the past two decades, a promising solution to the predicament of not having a truly mobile and inexpensive CD4 T cell counter has been emerging.

There has been much interest in applying and modifying standardized integrated circuit (IC) fabrication processes to create microfluidic lab-on-a-chip (LOC) systems for point-of-care (PoC) diagnostics. LOC systems share the same advantages of IC fabrication: high yield, throughput, and repeatability via parallel fabrication of possibly hundreds of chips per substrate result in lower manufacturing costs. Other advantages of LOC systems: (1) they have an inexpensive per test cost because they require smaller reagent volumes (μL vs. mL), (2) their highly specialized application makes operation simple, enabling their use by less specially-trained healthcare workers, (3) they would have minimal, if any, operation and maintenance costs, (4) their small footprint creates mobile platforms that could go directly into a high-needs area, and (5) they would come in a one-time-use, disposable chip that would reduce biohazards. These advantages make it possible for LOC systems to penetrate undeveloped regions that do not have an established healthcare infrastructure.

The aforementioned IC processes can be used to create fluidic channels with dimensions much smaller than a human hair, creating a unique fluidic environment. The dimensionless Reynolds number (Re) gives the ratio of inertial to viscous forces in a fluid under specific conditions, and is defined in Equation (2.1):

$$Re = \frac{\rho V L}{\mu} \tag{2.1}$$

where ρ is fluid density, V is the mean fluid velocity, L is the characteristic linear dimension of the fluidic interface, and μ is the fluid's dynamic viscosity. Generally, Re >4,000 denotes turbulent flow that is chaotic while a fluid with Re <2,300 transitions into the laminar regime where fluid flow becomes more "smooth" and predictable [41]. In the case of microfluidic channels, L is small (micrometers), resulting in Reynolds numbers much lower than unity. In this special case, viscous forces dominate inertial forces, and the Navier–Stokes equation for fluidic motion can be greatly simplified into the Stokes equations, which describe a fluid whose flow is independent of time, meaning flow is highly consistent and predictable. This allows for the precise spatial manipulation of microscopic objects, such as biological cells, through networks of channels, chambers, and micro- or nanofabricated sensors that

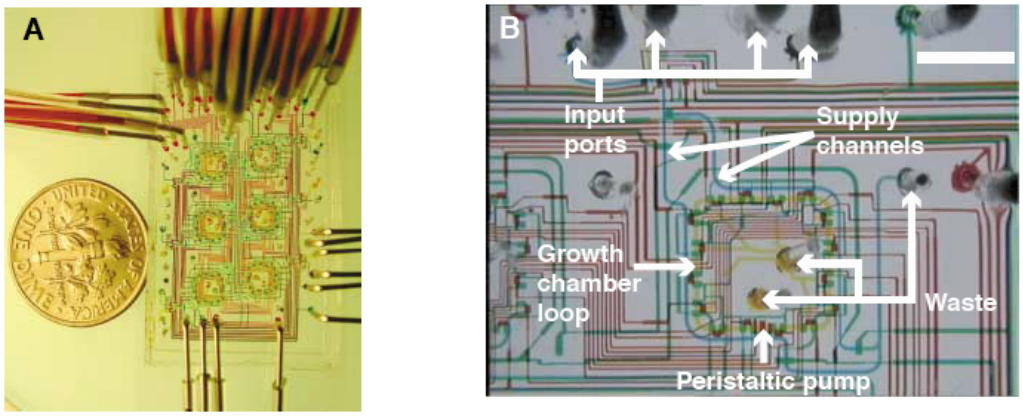

Figure 2.5: Microfluidic network for the long-term culturing of *E. coli*. (a) Size comparison of chip with a dime (18 mm in diameter). (b) Magnified view of fluidic network, which contains media supply channels, bacteria growth loop, and valves, forming an integrated peristaltic pumping system. Different channels are dyed with food coloring for illustration purposes. From [44]. Reprinted with permission from AAAS.

have a much higher sensitivity than macroscopic methods. The Quake group at Stanford University have pioneered and specialized in the manipulation of fluids and microorganisms in the microfluidic environment using microfabricated valves and pumps [42], sophisticated arrays for a microfluidic memory storage device [43], and microfluidic bioreactors that automatically regulated the cell density of *Escherichia coli* (*E. coli*) for long-term cell culture (see Fig. 2.5) [44].

Figure 2.6 illustrates one method of rapid fabrication of a microfluidics sensor: (a)–(d) shows the standard process for patterning microelectrode sensors on the surface of an oxidized silicon wafer, while (e)–(g) shows how a microfluidic channel is created by peeling off a cured polymer (such as polydimethylsiloxane, or PDMS) that has conformed to a micropatterned photoresist negative mold. The channel height depends on the thickness of the photoresist, which can be made less than 1 μm or more than 1 mm using different commercially available photoresists. The cured polymer and electrodes substrates are aligned and bonded (Fig. 2.6).

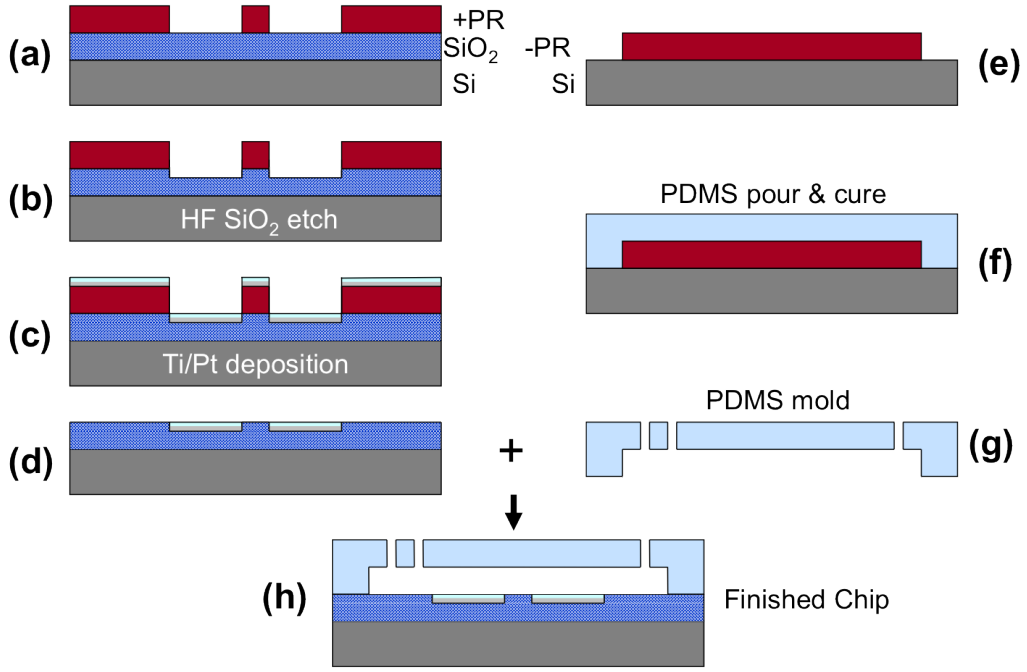

Figure 2.6: Rapid fabrication of a microfluidic sensor. (a) Photoresist is patterned on an oxidized silicon substrate. (b) Acid is used to etch a portion of the oxide, creating recesses. (c) Metal is deposited on the substrate. (d) The patterned resist is removed, lifting off the undesired metal, creating patterned electrodes. (e) A negative image of the fluidic channel is patterned on a silicon substrate. (f) Uncured PDMS is poured on the mold and cured. (g) The cured PDMS is pulled off the mold, and fluidic ports are punched before (h) bonding it to the electrodes chip.

2.5.1 Hand-held LOC Systems on the Market

One successful commercial LOC system for blood analysis is the Abbot Laboratories i-Stat® 1, which is a handheld unit ($10,000) that accepts one-time-use, disposable cartridges ($8–$40 each). Several cartridges are available that electrochemically test a few drops of patient blood for various factors, such as blood gas content, electrolytes, coagulation, and cardiac markers.

Recently, hand-held cellular analysis tools have entered the market. Invitrogen's Countess® Automated Cell Counter (∼$5,000 head unit with ∼$1 per test cost) analyzes homogenous cellular populations for concentration and viability using optics and image analysis algorithms. The Millipore Scepter™ resembles an over-sized micropipettor with single-use microfabricated tips that use the Coulter principle to electrically provide cell concentration and viability analysis. The Orflo® Moxi Z™ (∼$3,000) is another handheld Coulter counter unit which provides live/dead cell counts for less than $2 per test.

However, all aforementioned cellular analysis devices—intended to replace tedious and time-consuming manual cell counting using hemocytometers—require off-chip sample preparation and cannot differentiate among different cell types. As a result, much work remains to be done to create a diagnostics platform that can specifically enumerate cells in PoC situations (*i.e.*, CD4+ T cells). The following section details recent advancements in research to develop such a device.

2.5.2 Current Research in Cell Enumeration Systems

Many efforts have used fluorescent tagging and subsequent image processing to automatically enumerate CD4+ T lymphocytes in microchambers. Some designs relied on the even distribution of cells in a plastic chamber to produce accurate counts [45]. Others have used a microfabricated membrane to filter out erythrocytes, leaving leukocytes, which were fluorescently labeled [46]. Fluorescence detection was later enhanced by using quantum dots [47, 48], forming the technology behind LabNow, Inc. Immunospecific paramagnetic beads were used to bring fluorescently labeled CD4+ T cells into the focusing plane for analysis, reducing counting error [49, 50]. Cheng et al. have investigated CD4+ T cell capture by controlling shear stresses at the chamber

walls and enumerating cells using a cocktail of fluorescently labeled antibodies [51, 52]. They improved their design by including a monocyte depletion chamber to reduce the positive bias created at lower CD4+ T cell concentrations [53]. Beck *et al.* have eliminated the fluorescence labeling step required by the aforementioned methods by coating capture chambers with hydrogels containing fluorescent antibodies and drying them for storage [54]. During testing, blood enters the capture region, causing the hydrogel to swell and release the antibodies, specifically labelling CD4+ and CD8+ T cells. Subsequent fluorescent image cytometry is used to obtain the CD4+ and CD8+ T cell counts. The Alere Pima CD4 counter uses a similar method to label CD4+ T cells using cartridges containing a lyophilized antibody pellet, and has shown some success in field testing [54–57]. However, in some situations, it has operational costs similar to or more expensive than standard lab flow cytometric analysis [58].

The aforementioned optical methods require the use of lenses and focusing to analyze samples, but this can increase the cost and decrease the portability of the device. Gohring et al. quantified the antibody-mediated attachment of T cells by the amount of shift in the whispering gallery mode of an optofluidic ring resonator [59]. Moon et al. counted immobilized helper T cells by their shadows cast over a charge coupled device (CCD) by a white light source [60]. Wang et al. further simplified the optics by not requiring an external light source: immobilized CD4+ T cells were labeled with CD3-conjugated horeseradish peroxidase to facilitate a chemiluminescent reaction, which was amplified and quantified by a photodetector [61].

Electrical methods for enumerating CD4+ T lymphocytes prove to be promising due to the fact that they would not require optical components such as lenses, filters, light sources, photodetectors, and CCDs, which can be expensive, bulky, fragile, and require periodic maintenance. An electrical PoC solution could require only solid state components to electrically interrogate a sensing geometry, process sensor output, and provide input from and results to the user.

Mishra *et al.* used three-electrode cyclic voltammetry to estimate the number of CD4+ T cells that were selectively captured on a working electrode [62]. Jiang et al. have used this design as a building block to create an array of 200 of these electrochemical sensing regions, or pixels, conjugated with CD4 antibody. A pixel would be considered on when a CD4+ T cell was

captured, and a total cell count was the total number of on pixels [63].

Cheng *et al.* enhanced their CD4+ T cell capture device ([51,52]) by integrating impedance spectroscopy sensing into the capture channel to monitor the cell lysates [64]. T cells from whole blood were captured on-chip and lysed in a low-conductivity buffer, releasing intracellular ions into the bulk solution, thereby changing its conductance, which increased proportionally with cell concentration. The authors were able to correlate cell concentration with channel conductance with a detection sensitivity of 20 cells$\cdot\mu\mathrm{L}^{-1}$, eliminating the need of a microscope and manual cell counting. Daktari Diagnostics, Inc., has developed the Daktari CD4 counting platform based on this technology.

The lysate impedance method has shown to be the most promising technology to penetrate into resource poor regions, as it needs no off-chip sample preparation, requires only electrical means of interrogation, and is simple to operate. However, inherent drawbacks from measuring lysate impedance may reduce its efficacy. This technology assumes every patient's T cells contain similar ion concentrations, which may not be true, resulting in counting error. In addition, since the technology is sensitive to the concentration of ions, contamination from the sensor chip's materials and failure to wash away excess ions may reduce the system's counting resolution and dynamic range.

2.5.3 Microcytometry

A microfabricated flow cytometer (microcytometer) would combine the benefits of flow cytometry with that of LOC systems, resulting in a powerful AIDS diagnostics tool that could penetrate even the most impoverished regions in the developing world. Cells are counted one at a time as they flow through a small orifice, providing a counting accuracy that is superior to bulk counting methods.

Microcytometers can be divided into two groups based on their sensing techniques: optical and electrical, which are described in the following sections.

Optical

The mechanism behind optical microcytometry is similar to its macroscopic counterpart, and has been a research interest for many: LLS chips [65–68], LIF chips that use imaging software to count cells [69] or directly convert the fluorescence signal to an electrical signal using avalanche diodes [70–72], photomultiplier tubes [73–79], or PIN photodiodes [80]. Chen *et al.* combined LIF and LLS onto one platform using optical fibers, and could enumerate and discriminate between fluorescing and non-fluorescing beads [81]. Son *et al.* developed a method of detecting particles using a boron diffused resistor (BDR) and infrared (IR) diode. The particles would block the IR light which changed the effective resistance of the BDR [82].

Furthermore, others have used digital image processing to sort cells based on their size via pattern recognition or through fluorescent labels and sensing [83–85].

Wang *et al.* have developed a microfluidic chip which first labels CD4+ and CD8+ T lymphocytes (from buffy coat samples) on-chip using pneumatic vortexing before hydrodynamically focusing and LIF counting [86]. They were able to produce CD4/CD8 T cell ratios similar to that found using standard flow cytometry.

Electrical

We have chosen the electrical detection method for CD4 T cell enumeration because it would most likely provide the best penetration into the developing world. An electrical analog of optical microcytometers would likely prove to be more portable, cost effective, and less complicated. This is mainly due to the fact that an electrical microcytometer would provide both an electrical stimulus *and* electrical feedback for analysis. This would create a more streamlined setup that eliminates the need for expensive and bulky lasers, optics, and photodetectors and the requirement of complex image analysis software. The following is a brief history and theory behind the electrical enumeration and interrogation of cells, followed by more recent investigations in the microfabricated paradigm.

The invention of the Coulter Counter by Wallace and Joseph Coulter in the 1950s was the first major step in the electrical analysis of cellular popula-

tions. At the time, counting of biological cells and other particles was usually performed using colorimetry (color density of solution correlated with concentration of particles) or by manual counting under a microscope with a hemacytometer, which were somewhat inaccurate, time-consuming, and required highly-skilled technicians. The Coulter principle, illustrated in Fig. 2.7, allowed for automatic analysis of a particle population a single particle at a time. A known volume of particles is pulled by suction through a small aperture positioned between two electrodes with a constant voltage potential difference. This DC bias creates a Faradaic current that is temporarily blocked by the passing of a particle through the aperture, creating current pulses in time. The amount of current blocked (or the pulse peak amplitude) is directly proportional to the size of particle, resulting in a system that provides the size distribution of particle populations [87]. Equation (2.2) estimates the change in resistance, ΔR, caused by the passage of a particle of r_P through an aperture of cross-sectional area of A_C, in a solution that has resistivity of ρ_{sol} [88].

$$\Delta R = 2\rho_{sol}\left(\frac{arctan\left(r_P \Big/ \sqrt{\frac{A_C}{\pi} - r_P^2}\right)}{\pi\sqrt{\frac{A_C}{\pi} - r_P^2}} - \frac{r_P}{A_C}\right) \tag{2.2}$$

This not only can be used to obtain concentrations of populations, but also can discriminate among subpopulations based on particle size, surface charge, and mobility [89].

Microcytometers using the Coulter principle with DC voltage interrogation method have been reported [88, 91–94], but size-based analysis alone is not good enough to differentiate among different cellular populations of similar size. For example, not only are CD4+ T lymphocytes indistinguishable from other lymphocytes by size, but they are also similar in size to erythrocytes, which outnumber the T cells by a ratio of 5,000:1.

As an answer to this problem, investigators have used alternating field interrogation to differentiate among cell populations. H.P. Schwan's pioneering work in the field of dielectric spectroscopy showed that an impedance "signature" could be found for a particular cell population by varying the applied voltage signal's frequency and recording the resultant dielectric constant and conductivity [95–100]. Fig. 2.8 illustrates how the dielectric con-

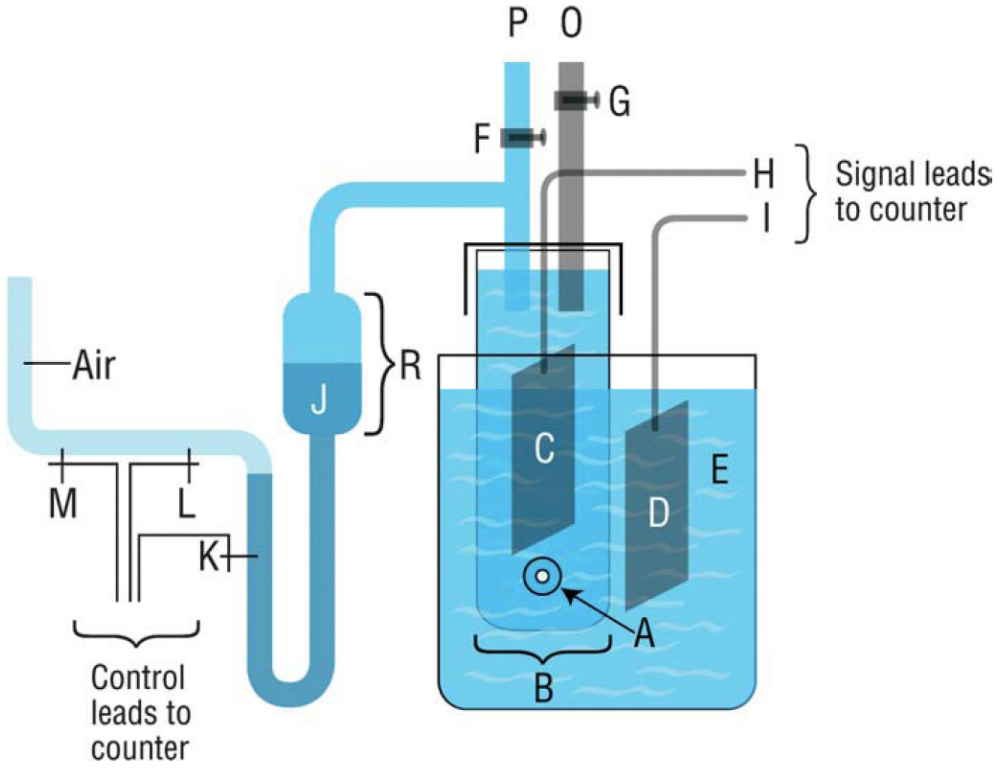

Figure 2.7: Coulter principle. A suction system draws particles in solution E through aperture A, causing a perturbation in the current flowing between electrodes C and D. B is a highly insulating glass cylinder which only allows current to pass through the aperture. A more detailed explanation can be found at the source, [90].

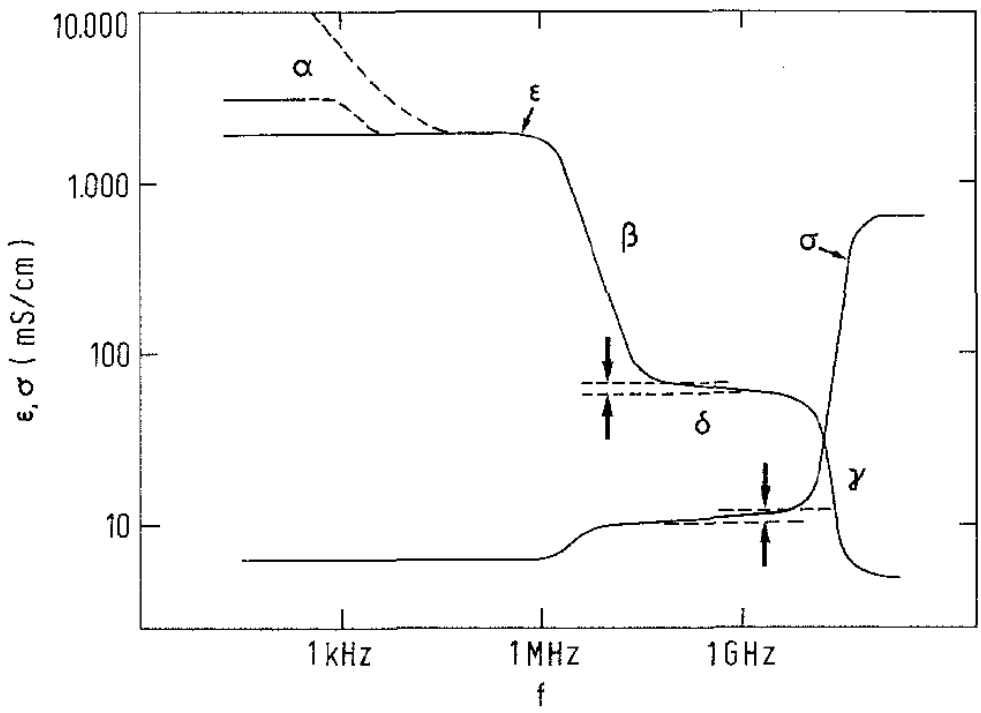

Figure 2.8: Relative permittivity, ε, and conductivity, σ, of blood cells, erythrocyte ghost cells, and *E. coli* bacteria of similar volume fraction. Respective dielectric dispersions are labeled (δ-dispersion is more subtle, and denoted by the arrows). All three populations had similar dielectric signatures, except in the α-dispersion regime, where all three populations could be distinguished: upper and lower dashed curves correspond to *E. Coli* and erythrocyte ghosts, respectively. From [99], used with permission; © 1983 Springer.

stant and conductivity of cellular populations are a function of frequency. The four drops (three distinct, one more subtle) in permittivity correlate with three different dispersion mechanisms from electrical relaxation phenomena. α-dispersion may be used to understand a cell's membrane conductivity [97]; β for membrane capacitance [100]; δ and γ for intracellular protein levels [95, 98, 99, 101]. For example, in Fig. 2.8 suspensions of blood, erythrocyte ghosts (internal contents replaced with buffer), and *Escherichia coli* bacteria each showed similar impedance signatures, except in the alpha dispersion regime, where they can be easily discriminated. Appendix A details how electrical characteristics of a cell can be extracted from its dielectric spectrum.

Coulter and Hogg were the first to apply this principle to enhance the

Coulter principle by simultaneously using DC and AC signals to distinguish between two similarly-sized particles of different composition, initiating the field of impedance flow cytometry [102]. Hoffman and Britt improved the sensing system to have multiple AC signals in addition to the DC signal to differentiate between plastic microbeads and mammalian cells [103, 104].

The benefits of impedance flow cytometry are enhanced in the microfluidic regime. Microfabricated electrodes and fluidic channels would decrease the sensing volume and increase the system's sensitivity to discriminate among different cell types. The advancement in electrical instrumentation has enhanced impedance sensing to be able to interrogate individual cells at many discrete frequencies. For example, Sun *et al.* simultaneously measured the impedance values of particles at 512 different frequencies via the Maximum Length Sequence (MLS) technique coupled with Fast Fourier transformations [105].

An understanding of the physics behind impedance microcytometry is necessary to fully appreciate its advantages over a standard Coulter design that only interrogates with a static field. Figure 2.9(a) represents a simplified circuit model of a cell in a microfabricated sensing region. The cell membrane is represented by capacitors (c_m) in series with its cytoplasm resistance (R_c). This agrees with the β-dispersion phenomenon previously described: higher frequencies will "short out" c_m, allowing the external electric field to penetrate the cell's interior, causing a sharp reduction in the cell's total impedance. R_{sol2} represents the resistance of the media around the cell (that was not displaced by the cell itself), R_{sol1} denotes the resistance between reference electrodes, and R_c is the cell's cytoplasm resistance. All three resistances can be estimated by

$$R = \frac{\rho_{sol} l}{A} \tag{2.3}$$

where ρ_{sol} is the solution resistivity (mostly dependent on ion concentration and mobility), l is the length of the conduction path in the solution, and A is the cross sectional area of the conduction path in the electrolyte. C_{dl} is double layer capacitance created by the accumulation of charge at the electrode-electrolyte interface, and is usually 20–50 $\mu\text{F}\cdot\text{cm}^{-2}$ (Fig. 2.10) [106].

Figure 2.9(b) illustrates the simulated complex impedance spectrum of

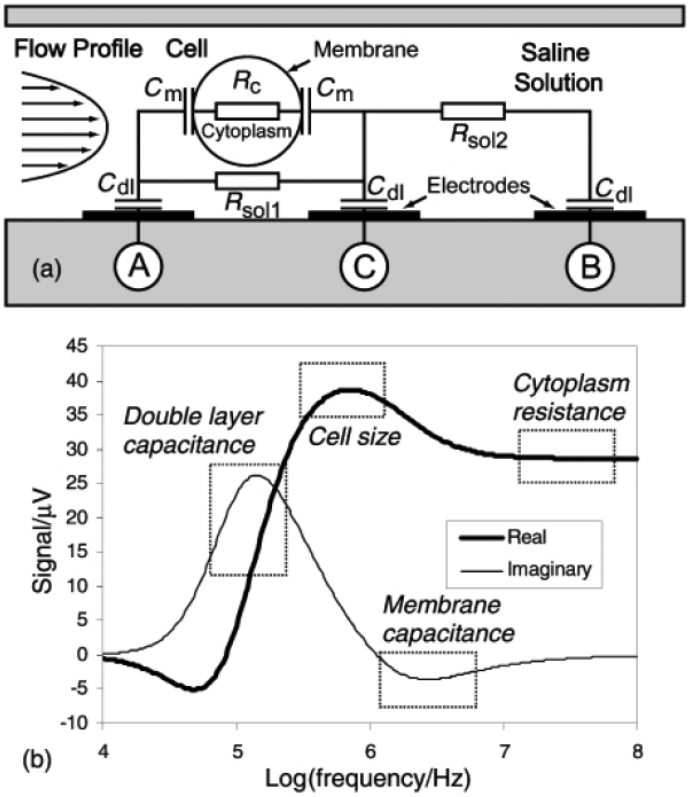

Figure 2.9: (a) Simplified electrical model of a cell within a measurement microchannel with reference electrodes. (b) Dependence of complex impedance on frequency, revealing various electrical characteristics of the cell. From [107] - Reproduced by permission of The Royal Society of Chemistry.

a 10 μm cell within the sensing region illustrated in (a). This shows how interrogating cells at different frequencies can potentially give valuable information that could be used to discriminate among different cell types, discern cell vitality, and observe cell growth cycles.

Impedance microcytometers have been developed to detect differences in modified cells. Cheung *et al.* were able to differentiate between erythrocytes and erythrocyte ghosts via impedance phase differences in addition to distinguishing between fixed and unmodified erythrocytes by observing changes in opacity (ratio of high and low frequency impedances) [110]. Kuttel *et al.* discriminated between healthy erythrocytes and those that were infected with *Babesia bovis*. The parasite modifies the dielectric properties of the cells' cytoplasm, which can be detected by using an 8.7 MHz interrogation signal [111]. Pierzchalski *et al.* could detect changes in the cell membrane

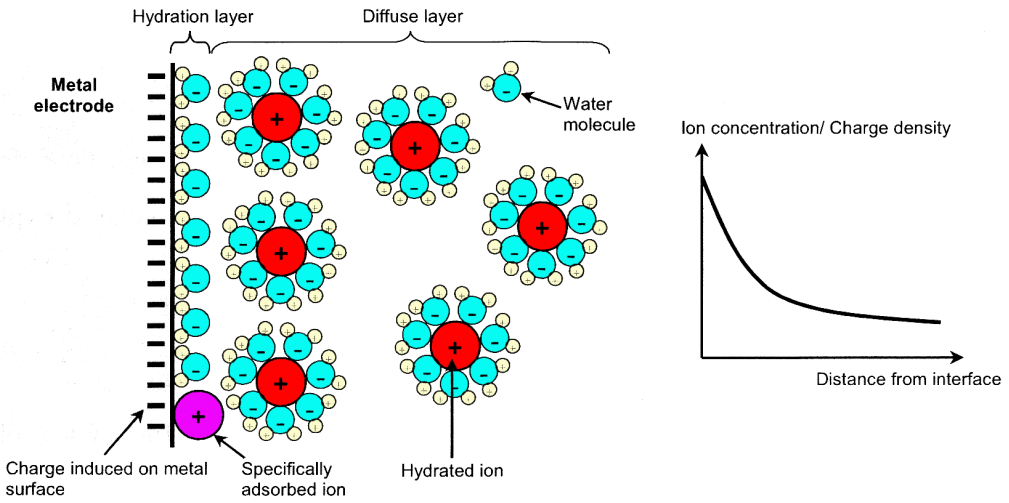

Figure 2.10: Electrical double layer formed around a negatively-charged electrode in ionic solution. Immediately upon electrode wetting, water molecules, which have a partial positive charge at their hydrogen atoms, form a barrier at the electrode-electrolyte interface, called the hydration layer (specifically adsorbed ions can also attach to the electrode surface). A second layer, called the diffuse layer, is comprised of hydrated ions that are more concentrated toward the electrode, creating a charge density gradient away from the interface. Applying an external potential to the electrodes will result in a change in electrode charge that is matched by the opposite charge in the electrolyte. Charge is accumulated and dissipated at the surface, similar to charging and discharging of a capacitor. [108, 109]. From [109], used with permission; © 2001 John Wiley and Sons.

potential of RN22 Schwann cells after modifying them in an ionophore solution [112].

Others have used impedance microcytometry to evaluate cellular processes. Schade-Kampmann *et al.* distinguished between dormant and budding *Saccharomyces* yeast cells. They also could electrically differentiate between healthy and apoptotic Jurkat E3.1 cells [113]. Pierzchalski *et al.* discriminated among live, necrotic, and apoptotic MCF-7 breast cancer cells based on their membrane capacitances at 4 MHz [112]. Cheung *et al.* noticed a decrease in impedance phase at 10 MHz correlated with cell death for homogenous populations of *Saccharomyces cerevisiae* yeast and *Bacillus megaterium* bacteria [114]. Sohn *et al.* monitored the life cycle of eukaryotic cells by observing their capacitance at 1 kHz. They were able to determine a cell's current growth phase by observing a positive linear relationship between the change in capacitance and a cells negatively-charged DNA content (Fig. 2.11) [115].

Differentiating among different cell types is critical to realize a practical PoC diagnostic platform. Schade-Kampmann *et al.* discriminated blood monocytes from differentiated dendritic cells in addition to 3T3-L1 fibroblasts from differentiated adipocytes [113]. Benazzi *et al.* distinguished among three algae (*Isochrysis Galbana*, *Rhodosorus m.*, and *Synechococcus sp.*) using a dual frequency measurement system [116]. Cheung *et al.* were able to discriminate among platelets and leukocytes from partially lysed erythrocytes and also sensed a difference in the impedance of HL-60 myoblast cells and differentiated macrophages [114]. Holmes *et al.* have developed an electrical microcytometer that can differentiate between different leukocyte subtypes, such as lymphocytes, monocytes, and neutrophils, solely on their impedance characteristics at two different frequencies (Fig. 2.12) [117, 118].

Although much advancement has been made in impedance microcytometry, it has still not proven to be sensitive enough to distinguish among different cells that may have similar electrical characteristics (cell size, membrane capacitance, cytosol conductivity, etc.). For example, CD4+ and CD8+ T lymphocytes have similar morphology, but perform different roles in the immune system. CD8+ T cells, or cytotoxic T cells, express the CD8 antigen on their membranes and attack and kill cells that are damaged, dysfunctional, or infected with a pathogen. CD4+ T cells, or Helper T cells, express the CD4 protein and do not directly attack other cells, but lead the immune

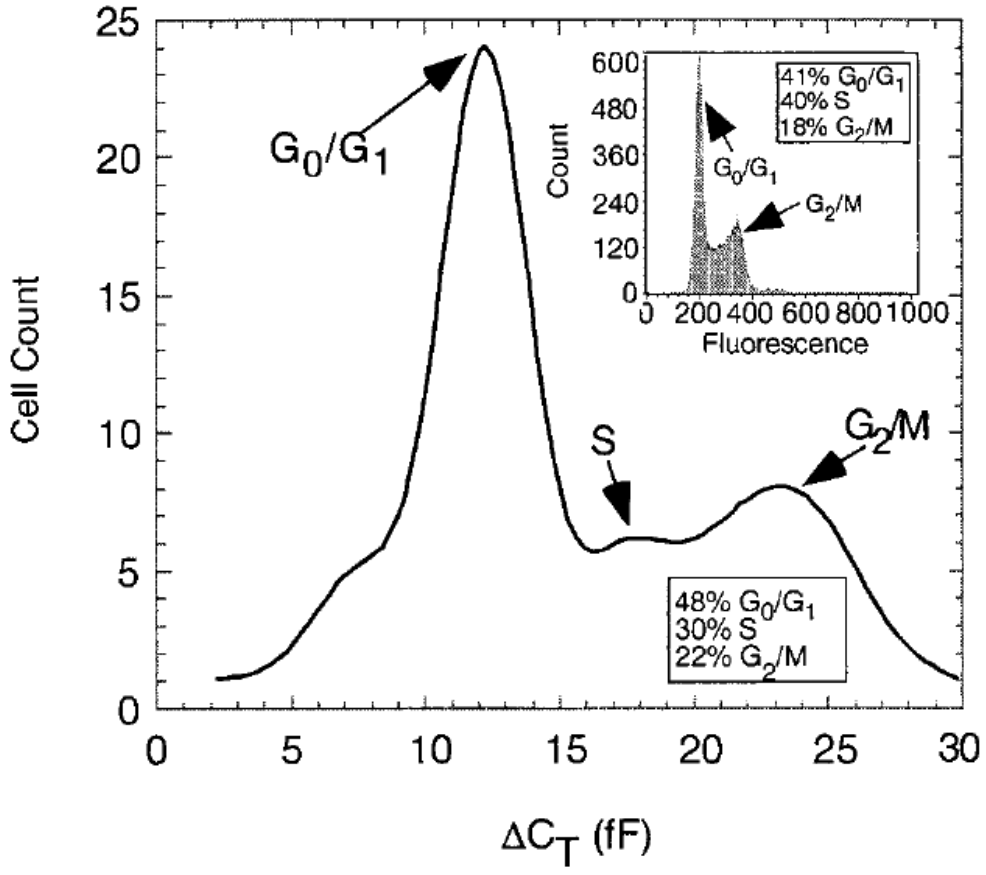

Figure 2.11: Growth cycle analysis of mouse myeloma cells (SP2/0) created by flowing the cell population through a capacitance sensing region in a microfluidic chip. The histogram shows the change in capacitance caused by cell passage. The inset graph from a flow cytometer's analysis of the same population shows good correlation with the chip's results. From [115], © 2000 National Academy of Sciences.

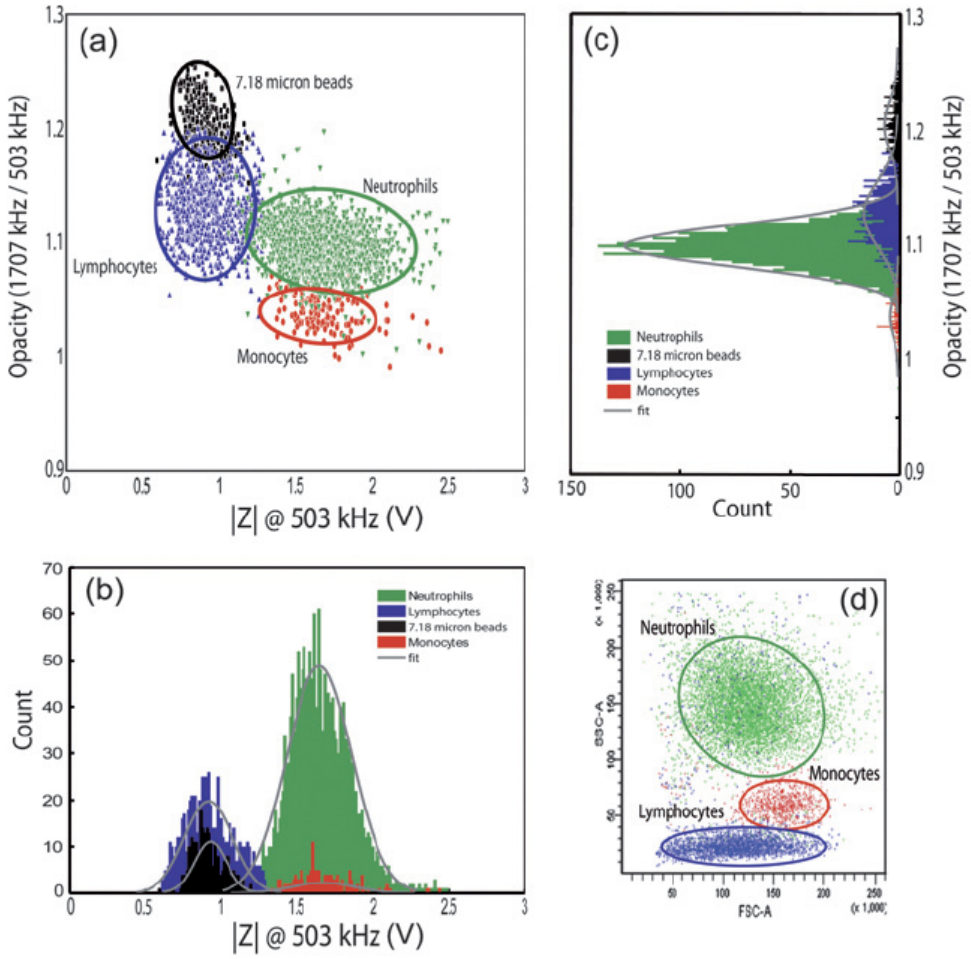

Figure 2.12: (a) Low frequency impedance vs. opacity (high frequency impedance / low frequency impedance) scatter plot illustrating electrical differentiation among different white blood cells types. (b) and (c) are impedance pulse height histograms for low frequency impedance and opacity data, respectively. (d) Forward vs. side scatter plot from flow cytometer for comparison. From [117] - Reproduced by permission of The Royal Society of Chemistry.

system's response by activating and directing other leukocytes to the source of the problem.

The few that have addressed this problem have enhanced the sensitivity of electrical interrogation of heterogenous populations through immunoaffinity assays. The highly specific affinity between a particular cell's surface antigen and its complementary antibody allows researchers to precisely target a particular cell type, given its targeted surface antigen is unique.

Wang *et al.* integrated a commercial metal oxide semiconductor field effect transistor (MOSFET) with optical fluorescence detection to determine the percent of CD4+ T cells among a total population of lymphocytes [119]. They have also created a similar system replacing the MOSFET with a two-stage differential amplification system [120, 121]. However, the added complexity of integrating both electrical and optical measurement systems may be prohibitive for PoC applications.

Holmes *et al.* were able to enhance electrical differentiation of CD4+ T cells from other leukocytes by specifically attaching 2.2 μm CD4 antibody-cojugated latex beads to the T cells to modify their high and low frequency characteristics (Fig. 2.13) [122]. They showed good correlation between their electrical chip-based method and the flow cytometry standard for the percentages of CD4+ T cells in white blood cell populations. However, the off-chip bead labeling steps they used would need to be integrated into the chip itself for this technology to be practical in resource-poor applications—but is difficult to perform in the laminar flow regime found at the microscale.

Some have used antibodies immobilized onto microfludic channel surfaces to facilitate a label-free method to distinguish cell types in heterogenous suspensions. Carbonaro *et al.* discriminated between CD34+ murine erythroleukemia (MEL) cells and human U937 cells by coating the counting channel with CD34 antibody [123]. The MEL cells interacted with the CD34 antibody, creating larger electrical pulse durations than the CD34- U937 cells that passed through the counter unaffected. As a result, the MEL cells could be distinguished from the U937 populations based on pulse duration. However, considerable overlap existed between the two populations, creating error in detection sensitivity.

Capturing cells of interest may eliminate the inherent error from modifying a cell's electrical characteristics or passage velocity characteristics, as both aforementioned methods could not distinguish the population of inter-

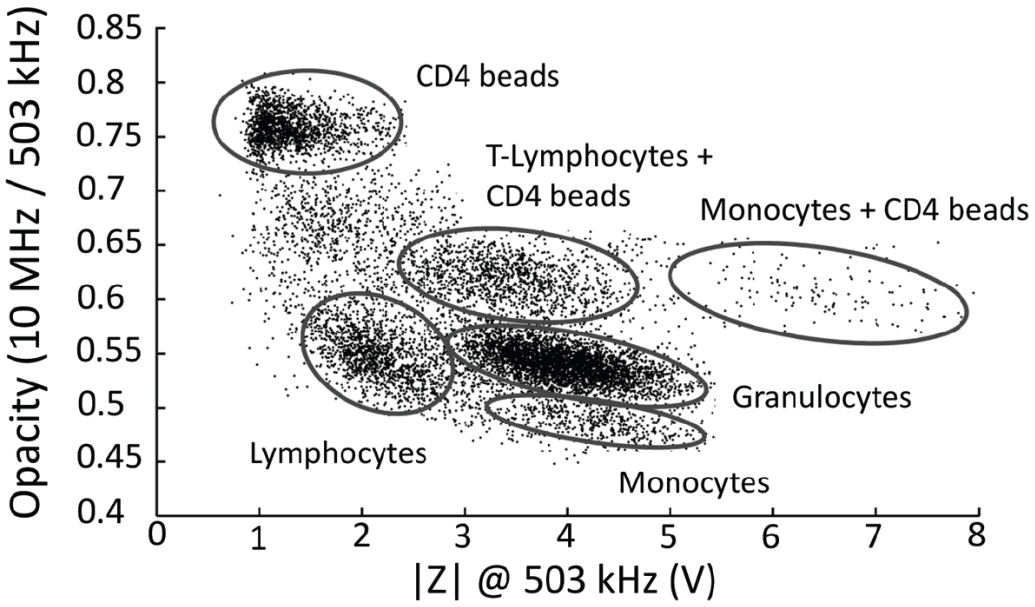

Figure 2.13: The attachment of 2.2 μm latex beads modifies the low frequency impedance and opacity (ratio of high and low frequency impedances) of CD4+ T cells enough to separate them from the other lymphocytes. Monocytes are also CD4+, but express it weakly and their larger size distinguishes them from the T cells. From [122] - Reproduced by permission of The Royal Society of Chemistry.

est enough from other cellular populations for practical portable diagnostics. Adams *et al.* developed a microfluidic platform which enumerated low concentrations of circulating tumor cells (CTC) using a chamber coated with antibodies specific to the cells [124]. Whole blood spiked with the CTCs was flown through the capture chamber, immobilizing the CTCs while the remainder of the blood washed out. A custom buffer was then flowed through the chamber to digest the antibodies and release the CTCs, which were then counted one-by-one at a Coulter sensor at the chamber's exit.

Chemical release of CD4+ T cells post capture has proven to be more difficult, as the cells may further bond to the substrate nonspecifically through membrane adhesion molecules. Zhu *et al.* have shown the capture and release of CD4+ T cells using electrochemical reactions on microfabricated electrodes; however some drawbacks are that some cell death occurs after T cell release ($\sim$10%) and agitation is needed to assist in electrochemical desorption, which is more difficult in the laminar flow regime found in a closed microfluidic chamber [125, 126]. In addition, mass production may be hindered by the fact that the capture region is limited to the area defined by the electrodes, requiring a PEG gel passivation layer elsewhere to prevent non-specific cell capture.

Gurkan *et al.* used a temperature responsive polymer to capture and release CD4+ T cells [127]. A capture chamber coated with poly(N-isopropylacrylamide) (PNIPAAm) was immobilized with CD4 antibody-Neutravidin complexes at 37 °C—when the polymer is hydrophobic and prefers interactions with the Neutravidin. CD4+ T cells are captured at the same temperature before washing away unbound cells and lysing erythrocytes. The CD4+ T cells are released by decreasing the chip's temperature below 32 °C, when the PNIPAAm layer becomes hydrophilic, releasing the antibody-Neutravidin complexes and thereby releasing the CD4+ T cells. They were able to release 59% of captured CD4+ T cells with high viability (94%). This method needs to address a few challenges before being a practical PoC device. This includes ensuring surface chemistry is preserved from manufacture to test (*i.e.*, storing the chips at $\sim$37 °C) and improving the release efficiency for accurate CD4+ T cell enumeration.

Instrument-Free CD4+ T Cell Diagnostics Since 2005, the Bill and Melinda Gates Foundation has been funding a CD4 initiative (centered at

Imperial College London) to create simple, power-free CD4+ T cell counting technologies that would lessen the costs of the tests and increase their penetration into resource-poor regions [128]. A semiquantitative immunochromatographic strip (ICS) being developed by The Burnet Institute compares the intensity of gold particles that are specifically attached to CD4+ T cells at a CD4 capture strip to a reference strip which has a similar intensity to a known concentration of CD4+ T cells [129]. Therefore, one can tell whether a patient has a CD4+ T cell count that is less than or greater than a crucial concentration. For example, a 2009 World Health Organization guideline for when to start ART is when CD4+ T cell concentrations become less than 350 cells$\cdot\mu\text{L}^{-1}$ [130]. Zyomyx has developed a device that uses the sedimentation of high density CD4 antibody-conjugated beads to estimate the concentration of CD4+ T cells from whole blood samples [129, 131]. These beads specifically attach to the CD4+ T cells and are sedimented with the help of a manually powered centrifuge. The height of sedimentation in the column is proportional to the concentration of CD4+ T cells, and is viewed through a window and compared to calibrated markings to give the CD4+ T cell count. The device also contains a chamber which used CD14-conjugated magnetic particles and a magnetic collar to deplete monocytes before the sedimentation step.

CHAPTER 3

A ROBUST ELECTRICAL MICROCYTOMETER WITH 3-DIMENSIONAL HYDROFOCUSING

3.1 Introduction

In this chapter, we present our initial approach in developing an electrical helper T cell counter for resource-poor regions in the world. As mentioned in Chapter 2, obtaining the concentration of human CD4+ T lymphocytes (helper T cells) is a necessary method to diagnose patients for AIDS and to give an accurate prognosis on the effectiveness of anti-retroviral drug treatment (ART). Here, we couple the AC impedance interrogation technique with 3-dimensional (3D) hydrodynamic focusing in a microfabricated flow cytometer (microcytometer). We study the effectiveness of the 3D hydrodynamic focusing mechanism through fluidic simulations and corresponding experiments to increase the signal-to-noise ratio of impedance pulses caused by particle translocation and to give the most accurate representation of particle size distribution. Helper T cell counts from the microcytometer are then compared with those found with the flow cytometer using sample volumes approximately the size of a drop of blood ($\sim$20 μL).

3.2 On-chip 3D Hydrodynamic Focusing

Figure 3.1(a) illustrates the concept of a microfabricated device with 3D hydrodynamic focusing that will be used to analyze blood cell populations. It is comprised of a hydrodynamic focusing region that manipulates cell position and an electrical interrogation region that counts individual cells. The electrical interrogation region is designed after the aforementioned Coulter principle. A low-frequency (50 kHz) AC voltage signal is applied across parallel, coplanar micro electrodes, resulting in parabolic current lines that

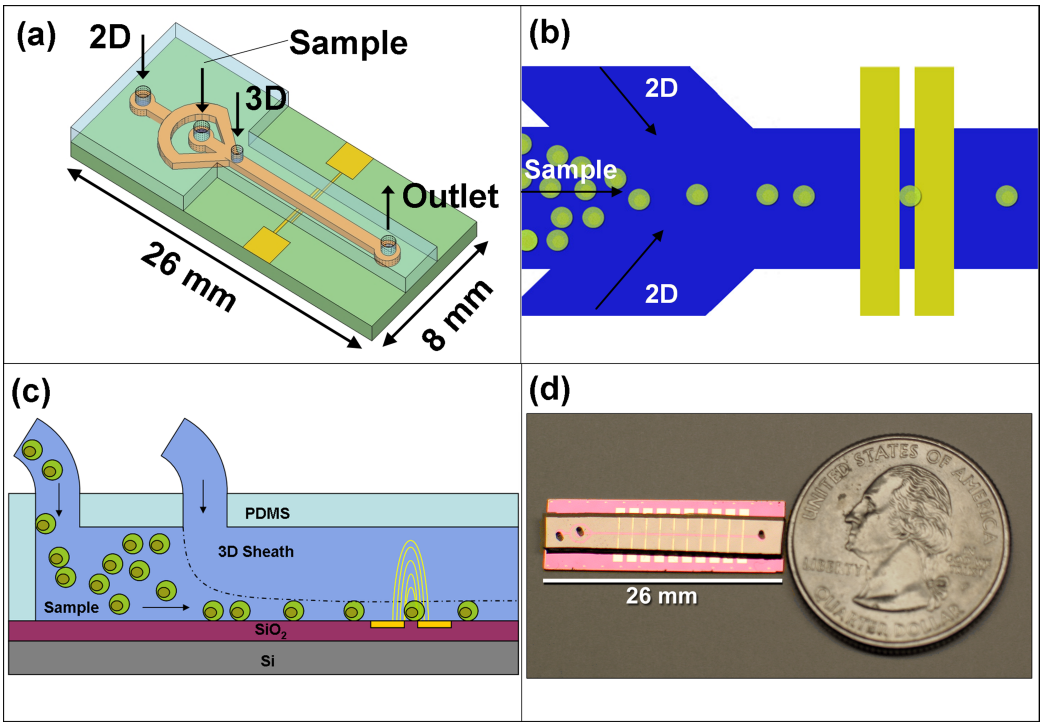

Figure 3.1: Concept of electrical microcytometer with 3D focusing mechanism. (a) Chip-level view of the 3D hydrodynamic focusing and electrical sensing region (not drawn to scale). (b) The 2D sheaths force particles in the sample stream to flow in a single-file manner and the (c) 3D sheath ensures the particles flow consistently close to the sensing electrodes. (d) Size comparison of chip to a quarter dollar. From [133] - Reproduced by permission of The Royal Society of Chemistry.

extend upwards toward the top of the channel. A cell or other particle passing through this region will either enhance or block current, depending on the relative conductivity of the particle to the surrounding medium. This will temporarily change the effective impedance of the sensing region, resulting in an impedance pulse with a width corresponding to the particle translocation time. In this study, cells are treated as non-conducting spheres at 50 kHz, which is well below the characteristic frequency, f_C, of a cell's membrane ($>$ 2 - 3 MHz) [95, 132]. Cell passage will increase the impedance of the sensing region similar to the polystyrene particles also used in this investigation. Therefore, particle size (or conversely, the volume of conductive buffer displaced by the particle) will dominate the impedance pulse amplitude.

Hydrodynamic focusing is a simple but elegant mechanism used in flow cytometry to ensure accurate population analysis by forcing particles to flow

in a single-file and spatially consistent manner through the sensing region. This reduces the possibility of coincidence events, where multiple particles simultaneously pass through the sensing region, and decreases signal inaccuracies from variance in particle translocation position [134]. Hydrodynamic focusing relies on the concept of laminar fluid flow where a fluid's viscous forces dominate its inertial forces, creating a predictable and stable flow in which multiple streams flow adjacently with little or no mixing. The low Reynolds number associated with microscale fluidic channels creates an ideal environment for laminar flow, even at relatively high fluid velocities (in our case, up to 26 cm·s^{-1} with a total flow rate of 100 μL·min^{-1}). We take advantage of this property to ensure cells and other particles flow in a single-file manner and consistently in close proximity to the sensing electrodes. Figure 3.1(b) illustrates how we first force particles into a single-file line via lateral sheath flows. Although this 2D focusing mechanism greatly reduces the probability of coincidence events, the system still suffers inaccuracy from the variance of pulse amplitude from particles passing through the sensing region at varying heights [107]. To solve this problem, we subsequently use a third sheath to vertically confine the sample stream close to the sensing electrodes, completing the 3D focusing mechanism (Fig. 3.1(c)). This increases the impedance pulse signal-to-noise ratio by forcing cells to pass through the highest current line density nearest the electrodes. It also better represents the size distribution of a particle population by eliminating the variance in particle translocation height (e.g., larger particle passing farther from electrodes may block the same amount of current as a smaller particle passing closer to the electrodes). Therefore, one can confidently assume pulse height is directly proportional to particle size.

An optimal sheath-to-sample flow rate ratio (R) is necessary to create a sample stream core that is the approximate dimensions of the cells or other particles of interest. R is generally defined as

$$R = \frac{F_{SHEATH}}{F_{SAMPLE}} \tag{3.1}$$

where F_{SHEATH} and F_{SAMPLE} are the sheath and sample infusion flow rates, respectively. Specifically, R_{2D} represents the flow rate ratio of the laterally confining sheaths (split from same inlet) to the sample, while R_{3D} represents the flow rate ratio of the vertically confining sheath to the sample. We use

simulations to optimize R_{2D} and R_{3D} for the enumeration of helper T cell concentrations and confirm the results experimentally.

3.3 Materials and Methods

3.3.1 Microcytometer Fabrication

Electrodes Layer

The substrate containing the stimulating/sensing electrodes was fabricated using standard photolithography and metal lift-off techniques (Fig. 3.2). A 4" Si wafer was piranha cleaned (H_2O_2:H_2SO_4, 1:1) and baked on a hotplate at 120 °C for 15 minutes before wet oxidation at 1150 °C to obtain a SiO_2 thickness of 0.6 μm (not shown in figure). AZ-1518 positive photoresist (AZ Electronic Materials, Charlotte, NC) was spun on the wafer at 4,000 rpm for 40 s, soft baked on a hotplate at 90 °C for 5 minutes, aligned with the electrodes mask and exposed for 20 s under a Canon PLA501F 4" mask aligner (Canon Corp., Tokyo, Japan). The photoresist was then developed in AZ Developer (AZ Developer:DI water, 1:1) for 1 minute, rinsed thoroughly with DI water for 2 minutes, dried with N_2, and hard baked at 110 °C for 2 minutes (Fig. 3.2(a)). The wafer was submerged in buffered HF acid (BHF; 6:1) to etch 300 nm of the exposed SiO_2 and create recesses for the electrodes (Figure 3.2(b)). After thorough rinsing with DI and N_2 drying, electrodes were created by depositing a 30 nm adhesion layer of Ti and subsequent 270 nm layer of Pt using an Airco FDC 1800 electron beam evaporator (Airco-Temescal, Berkeley, CA) (Figure 3.2(c)). The wafer was then placed in acetone overnight to remove the underlying photoresist and lift off the unnecessary metal, resulting in the desired recessed electrode pattern (Fig. 3.2(d). Wafers were diced using a Disco DAD-6TM dicing saw (Disco Hi-Tec America, Raleigh, NC). The recessed electrodes ensured optimal bonding of the fluidic layer (described below) by eliminating the abrupt step height of the electrodes.

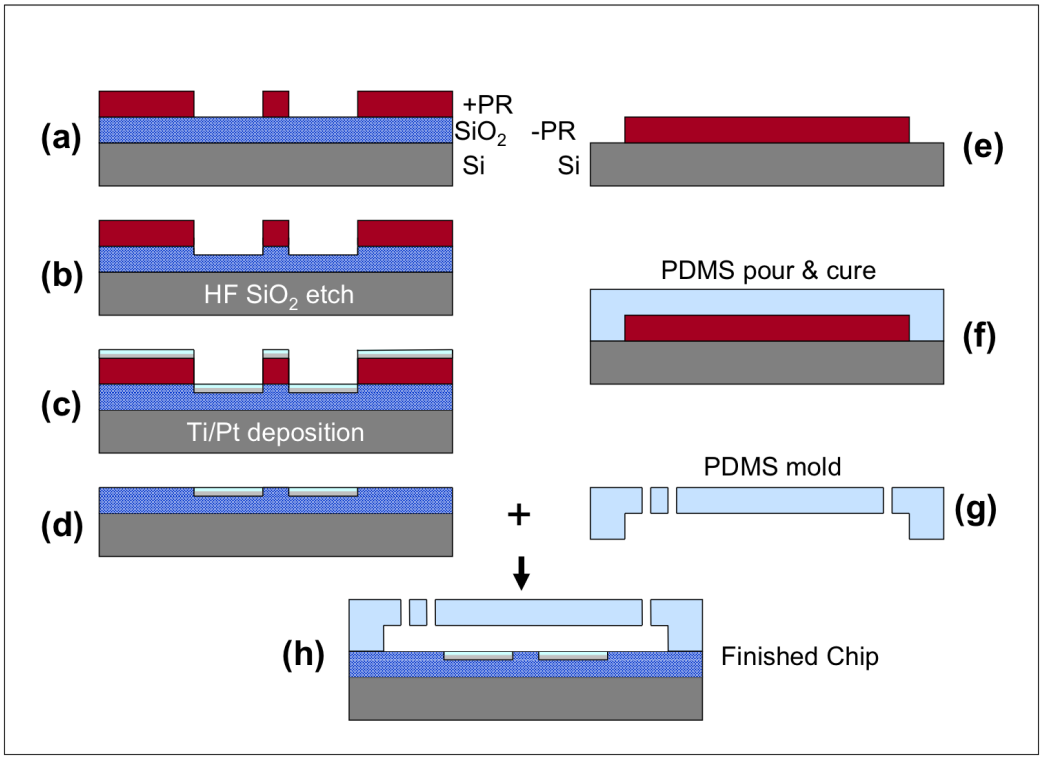

Figure 3.2: Fabrication process flow for both electrical sensing (left) and microfludics (right) layers, covalently coupled by oxygen plasma bonding of the PDMS and SiO_2 surfaces (not drawn to scale). From supplemental materials from [133] - Reproduced by permission of The Royal Society of Chemistry.

Fluidic Channels Layer

The microfluidic channels were created by a standardized and rapid technique using a thick negative photoresist (SU-8; Microchem Corp., Newton, MA) and a biocompatible polymer, Polydimethylsiloxane (PDMS; Dow Corning, Midland, MI). A 4" Si wafer was piranha cleaned and baked at 120 °C for 15 minutes before spinning on SU-8 negative photoresist to a thickness of 30 μm. After soft-baking (65 °C for 3.5 minutes, then 95 °C for 9 minutes), the wafer was exposed for 22 s under the 5" mask aligner and submerged in SU-8 Developer for 4 minutes, rinsed with isopropyl alcohol, and hard baked at 120 °C for 20 minutes (Fig. 3.2(e)). A positive mold of the 32 μm-high channels was created by pouring uncured PDMS (10:1 ratio of pre-polymer to curing agent) onto the negative SU-8 mold and polymerizing it for 8 hours at 65 °C (Fig. 3.2(f)). After curing, PDMS dies were cut out, peeled off, and holes corresponding to the sheath inlet, sample inlet, and output were punched out using a customized syringe needle (Fig. 3.2(g)). A hermetic seal between the PDMS and substrate was formed by oxidizing both with O_2 plasma (200 W, 1 Torr, 35 s) in a barrel etcher followed by quick alignment of channels to electrodes and bonding (Fig. 3.2(h)). Cured PDMS dies were cut out and holes corresponding to the 2D and 3D sheath inlets, sample inlet, and outlet were punched out using customized syringe needles. A hermetic seal between the PDMS and substrate was formed by oxidizing both with O_2 plasma in a barrel etcher followed by quick alignment of channels to electrodes and bonding. The plasma creates silanol groups on the PDMS which makes it hydrophilic, enabling it to covalently bond with the SiO_2 layer on the substrate [135]. Microbore tubing was inserted into the three inlets and sealed with epoxy to create a fluidic pathway between the chip and three Harvard syringe pumps (Harvard Apparatus, Holliston, MA), enabling independent control over each inlet infusion rate. Tubing was also inserted into the waste port to ensure proper containment of biological waste.

3.3.2 Electrical Impedance Sensing Setup

Figure 3.3 illustrates the experimental setup used to hydrodynamically manipulate and electrically interrogate cell and particle populations. The SR

850 lock-in amplifier (Stanford Research Systems, Inc., Sunnyvale, CA) was used to apply a 4 V (rms) internally-referenced 50 kHz sinusoidal signal across the resistor R and the platinum electrodes (14 μm wide, 7 μm gap). The value of R was chosen to match the impedance value of the channel sensing region at 50 kHz in order to facilitate the highest sensitivity when a cell or particle perturbs it. An Agilent 4284 LCR meter (Agilent Technologies, Inc., Palo Alto, CA) was used to find the impedance spectrum of the electrodes in PBS for the 10^2 to 10^6 Hz frequency range, and an R value of 10 kΩ was obtained. Real (X) and Imaginary (Y) impedance signals were exported from the lock in amplifier and recorded in binary format on a computer running NI LabVIEW via a PCI-6221 DAQ card (National Instruments, Austin, TX). Matlab (The MathWorks, Natick, MA) was used to convert the NI binary file into a text format to be read in by the Axon Clampfit 10 software (Molecular Devices, Sunnyvale, CA). Clampfit was used to adjust the baseline of the impedance signal, filter out excess noise, and analyze the impedance pulses using the threshold search method. This method only records a pulse when its amplitude is at least the same as the trigger level (in our case, set as a multiplicative factor of the standard deviation of the noise of the baseline signal without cells or particles). Three syringe pumps were used to independently control the sample, 2D sheath, and 3D sheath inlet flow rates in order to facilitate and investigate the 3D hydrodynamic focusing of particles and cells. A sensitive Pixera Penguin 600CL CCD camera (Pixera Corporation, San Jose, CA) coupled to a Nikon Eclipse E600FN microscope (Nikon Instruments, Inc., Melville, NY) was used to observe cells and beads passing through the sensing region, ensuring particles were being focused and that impedance pulses were from particle passage.

3.3.3 Simulations of 2D and 3D Focusing of Sample Stream

The FLUENT Computational Fluid Dynamics simulation package (ANSYS, Lebanon, NH) was used to find the optimal flow rate ratios between the sample inlet and each of the 2D and 3D sheath inlets. Experiments, described below, were performed to evaluate the accuracy of the 2D and 3D focusing simulations.

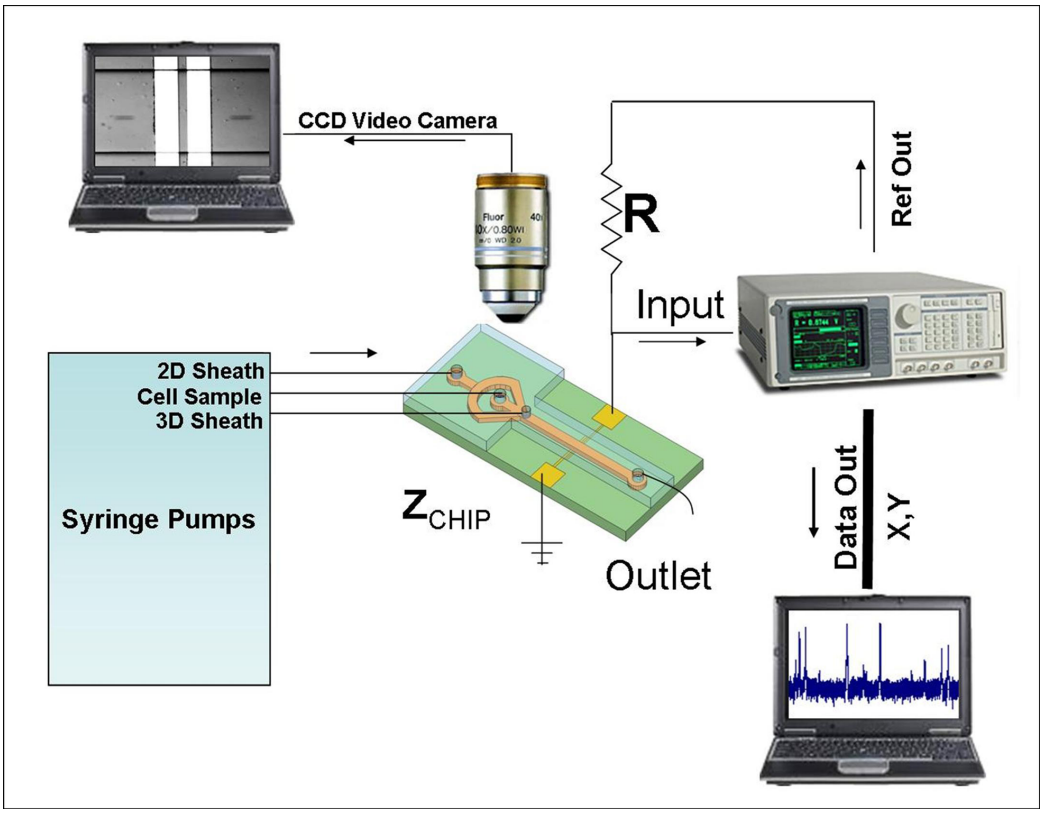

Figure 3.3: Experimental setup: syringe pumps control sample and sheath flows through the sensing region, which is connected to the external circuit via micro-manipulators (not shown). From [133] - Reproduced by permission of The Royal Society of Chemistry.

3.3.4 2D Focusing of Sample Stream of Trypan Blue

The optimal R_{2D} was obtained experimentally by independently varying the infuse rates of the 2D sheath and sample inlet syringe pumps. Trypan Blue dye was infused into the sample inlet to distinguish the sample flow stream from the sheath flow streams. The sample stream width was precisely measured by analyzing micrographs taken using a digital video camera coupled to a microscope. This analysis was performed on a chip with a glass substrate to enhance the contrast of the sample stream via microscope backlight. No 3D sheath inlet was punched into the PDMS microfluidics layer.

3.3.5 3D Focusing of Polystyrene Particles

The optimal 3D sheath flow rate ratio was experimentally found by focusing 7.32 μm polystyrene microparticles (Bangs Laboratories, Inc., Fishers, IN) by varying R_{3D} and observing the change in the average and distribution of impedance pulse heights. R_{2D} was locked at the optimal ratio found in the 2D Trypan Blue experiment. The total flow rate was locked at a constant value to ensure constant bead velocity through the sensing region for all 3D flow ratios because it was found that the average pulse heights would decrease for increasing bead velocities (unpublished data). The shorter pulses in the time domain from faster bead velocities result in a broader spectrum of frequency components that are lower in amplitude; eventually, the higher frequency components are clipped out by the lock-ins low pass filter. The microbeads were diluted in phosphate buffered saline (PBS), sonicated for 5 minutes to reduce bead aggregates, and infused into the sample port at a flow rate of 4 μL$\cdot$min^{-1} with a total flow rate (2D sheath + 3D sheath + sample) of 100 μL$\cdot$min^{-1}.

3.3.6 CD4+ T-Lymphocyte Concentration Comparisons

It is imperative that the microfabricated chip can reliably provide cell counts that are comparable to the industry standard method of flow cytometry. In this study, we compared our device to the Becton Dickinson LSR II Flow Cytometer (Becton Dickinson, Franklin Lakes, NJ) by analyzing varying dilutions of cultured 8E5/LAV cells, a human lymphoblastic cell line from

ATCC (Manassas, VA). Cells were cultured two to three times a week in RPMI-1640 media (ATCC) with 10% fetal bovine serum (Fetalplex, Gemini Bio-Products, West Sacramento, CA) and kept in a 5% CO_2 incubator at 37 °C. Various dilutions of the lymphoblasts were created by the following method. Approximately 10 mL of 8E5/LAV cell suspension was spun down into a pellet using an Eppendorf 5810R refrigerated centrifuge (Eppendorf International, Hamburg, Germany) at 4 °C and 200 x g for 10 minutes. The pellet was resuspended in PBS + 1% bovine serum albumin (BSA), pelleted a second time, and resuspended in 1 mL PBS + 1% BSA to obtain a high concentration of cells (5 x 10^6 mL^{-1}). A dilution series was then created to give concentrations ranging from 10^3 to 5 x 10^6 cells·mL^{-1}. Cells were kept on ice during the entire experiment. Each dilution was then injected into the sample inlet via syringe pump at a rate of 4 $\mu L \cdot min^{-1}$ with the 2D and 3D sheath pumps infusing PBS at their respective optimal rates. Cell concentration was found by dividing the number of pulses by the known amount of sample volume flown during a 5 minute time period (20 μL total volume flown). The BD LSR II flow cytometer was then used to obtain the concentration of aliquots from the same dilutions. A known volume of a known concentration of FITC fluorescent beads (Bangs Laboratories) was mixed with each cell dilution. The beads were gated on the FITC channel with an event stop value of 10,000 total beads. Cellular events were gated based on their forward scattering (FSC) and side scattering (SSC) characteristics. Cell concentrations were calculated by the ratio of cellular events to bead events, multiplied by the known concentration of counting beads.

3.4 Results and Discussion

3.4.1 Optimal Flow Ratios for 2D and 3D Focusing of Particles

A 3D representation of the fabricated 200 μm wide and 32 μm high microchannels was constructed using hexahedral cells[1] (∼175,000) in the Gambit mesh generation software (ANSYS) and imported into FLUENT. A vol-

[1]To avoid ambiguity, the "cell" referenced in this section refer to discrete volumes used in finite element modeling, unless otherwise noted.

ume of fluid (VOF) multiphase model was constructed assuming laminar, incompressible, immiscible, and isothermal flows as well as a no-slip condition at all sidewalls. The optimal R_{2D} was obtained by performing multiple simulations with R_{2D} ranging from 1 to 16 with the 3D sheath flow velocity set to 0. After 2,500 iterations, the sample stream width, W_S, was determined by measuring the width of cells which contain at least a 50% volume fraction of the fluid from the sample fluid.[2]

Experiments were performed to compare W_S dependence on R_{2D} from the simulation results using Trypan Blue dye to distinguish the sample flow stream from the sheath flow streams. 50% (v/v) Trypan Blue and DI water were infused into the sample and sheath inlet ports, respectively. Infusion rates for both sample and 2D sheath pumps were varied to match the flow rate ratios in the simulations. Micrographs were taken 30 s after changes in R_{2D} to ensure the system was stable. W_S values were obtained by comparing the dyed stream to the known channel width. Figure 3.4 illustrates the positive correlation between the sample stream and the flow rate ratio. A lower flow rate ratio results in more sheath volume at the channel junction, which displaces the sample stream and causes it to become thinner. A R_{2D} ratio of 8 gives a W_S of 12.3 μm, which proves to be the optimal focusing condition for the cultured lymphoblasts. This is similar to the simulated results of 12 μm for the same R_{2D} ratio, as shown in Fig. 3.5(a). Figure 3.5(h) shows the decaying exponential dependence of W_S on R_{2D} and the strong agreement between the experimental and simulated results. This consistency ensures that cells of particular size can be predictably focused into a single-file line at the corresponding flow rate ratio.

The optimal R_{3D} was obtained through simulations by locking R_{2D} at 8, and varying R_{3D} from 1 to 16. Figure 3.5(h) illustrates the decaying exponential dependence of sample stream height, H_S, on R_{3D}. Figure 3.5(f) shows that an R_{3D} of 8 gave the optimal H_S of $\sim$10 μm, creating a sample stream core with the same dimensions of blood cells. This size ensured cells and particles would stay in close proximity to the sensing electrodes but was large enough to keep them within the sample flow stream. Experiments were performed to test the accuracy of these simulations as well as the reliability of our 3D focusing mechanism. Polystyrene beads were injected into the sample

[2]The volume fraction of a cell is the percentage of cell volume that contains the phase of interest.

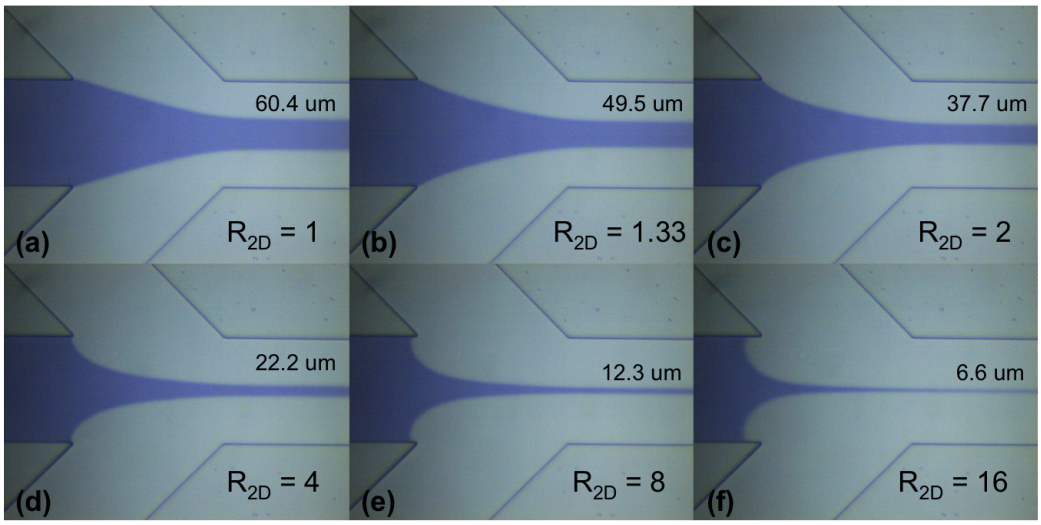

Figure 3.4: Micrographs of 2D focusing region with Trypan blue sample for various R_{2D} values. From supplementary materials from [133] - Reproduced by permission of The Royal Society of Chemistry.

inlet at identical R_{2D} and R_{3D} values to those tested in FLUENT, and 5 minutes of impedance data was recorded (20 μL). Clampfit was used to record and analyze pulses that were at least four times the standard deviation of the baseline noise. Figure 3.6(a) illustrates how bead impedance pulses become more uniform with $R_{3D} = 8$, (iii), versus no 3D focusing, (ii), showing that the beads were indeed flowing closer to the electrodes at a higher consistency. This can be quantitatively reflected in the increase in mean and decrease in standard deviation of the pulse amplitude for a duration of 4 s from (ii) to (iii). Figure 3.6(b) shows the percentage change, $\%\Delta\mu_Z$, in average pulse height for varying R_{3D} values and the corresponding percent change in standard deviations, $\%\Delta\mu_Z$, for the entire 5 minutes of analysis. $\%\Delta\mu_Z$ is the normalized difference between average pulse height amplitudes for $R_{3D} > 0$ (μ_X) and $R_{3D} = 0$ (μ_0), and is defined as

$$\%\Delta\mu_Z = \frac{\mu_X - \mu_0}{\mu_0} \tag{3.2}$$

$\%\Delta\sigma_Z$ is calculated in the same way, but replacing μ_X and μ_0 with σ_X and σ_0, respectively. The positive correlation between pulse amplitude and R_{3D} for $R_{3D} = 1$ to 8 shows that the beads were successfully being manipulated to flow closer to the sensing electrodes and block a higher percentage of current. It was found that $R_{3D} = 8$ resulted in the largest increase of average

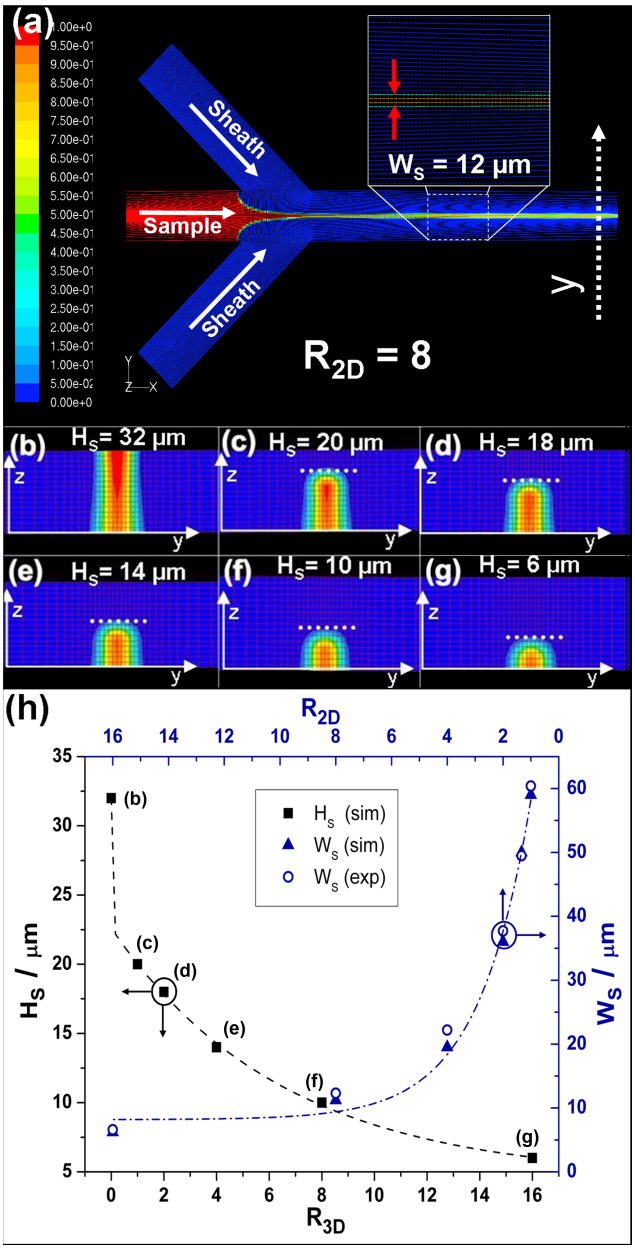

Figure 3.5: (a) FLUENT simulation of 2D hydrofocusing of the sample stream for $R_{2D} = 8$, giving an optimal sample stream width of 12 μm. (b - g) Height profile of sample stream for R_{3D} values of 0, 1, 2, 4, 8 16, respectively; profile was taken parallel to the Y axis, as denoted in (a). (h, top and right axes) Comparison between experimental (open circles) and simulated (solid triangles) results for W_S for various R_{2D} values; dash-dot line represents exponential fitting of simulated data ($R^2 = 0.992$). (h, bottom and left axes) Sample stream height dependence on R_{3D} from simulations with labels linking points to corresponding simulations in (b - g); dashed line represents two-phase exponential association fitting ($R^2 = 0.999$). Adapted from [133].

pulse amplitude (44.4%) and largest decrease in pulse amplitude standard deviation (15.4%) versus no 3D focusing. $R_{3D} = 16$ resulted in a decrease in mean amplitude and increase in standard deviation most likely because the sample stream height was too small ($\sim$6 μm in simulations, Fig. 3.5(g)) to consistently contain the 7.32 μm particles. Its 30.8% increase in standard deviation over no 3D focusing ($R_{3D} = 0$) could be from the fact that many particles could not stay within the sample stream and were forced into the sheath at varying heights above the electrodes. Figure 3.6(c) compares the pulse height distributions between beads undergoing no 3D focusing and optimal focusing ($R_{3D} = 8$). The differences between the pulse distributions show that the optimal 3D focusing of the particles results in a better representation of particle size distribution. In the case of no 3D focusing, the pulse distribution is of decaying exponential nature. Optimal focusing results in a Gaussian distribution, which is expected for the discrete-sized microparticles with a mean diameter. This eliminates pulse amplitude ambiguity caused by variance in particle translocation height above the sensing electrodes. Figure 3.6(d) shows the pulse duration histogram for no 3D focusing and optimal 3D focusing. Optimal 3D focusing gives a larger average duration because particles are flowing closer to the electrodes, where the field line distribution covers more distance in the direction of particle flow. The 39.9% decrease in standard deviation at optimal focusing conditions further supports that the beads were translocating at a more consistent height above the electrodes.

3.4.2 T Cell Concentration Comparison

T cell counts using the electrical microcytometer were compared against the BD LSR II flow cytometer for concentrations ranging over three orders of magnitude (10^3 to 2 x 10^6 cells$\cdot$mL^{-1}) with the majority of concentrations within the critical range of < 500 cells$\cdot\mu$L^{-1} for HIV/AIDS diagnostics. 20 μL of each sample was analyzed by the microcytometer under optimal 3D focusing conditions ($R_{2D} = R_{3D} = 8$). Clampfit was used to obtain each sample concentration by denoting a cellular event as a pulse that was at least five times the standard deviation of the baseline noise. As a control, aliquots from the same samples were then analyzed by the LSR II flow cytometer. Figure 3.7 compares the LSR II data, (a), with that of the microcytometer, (b). The

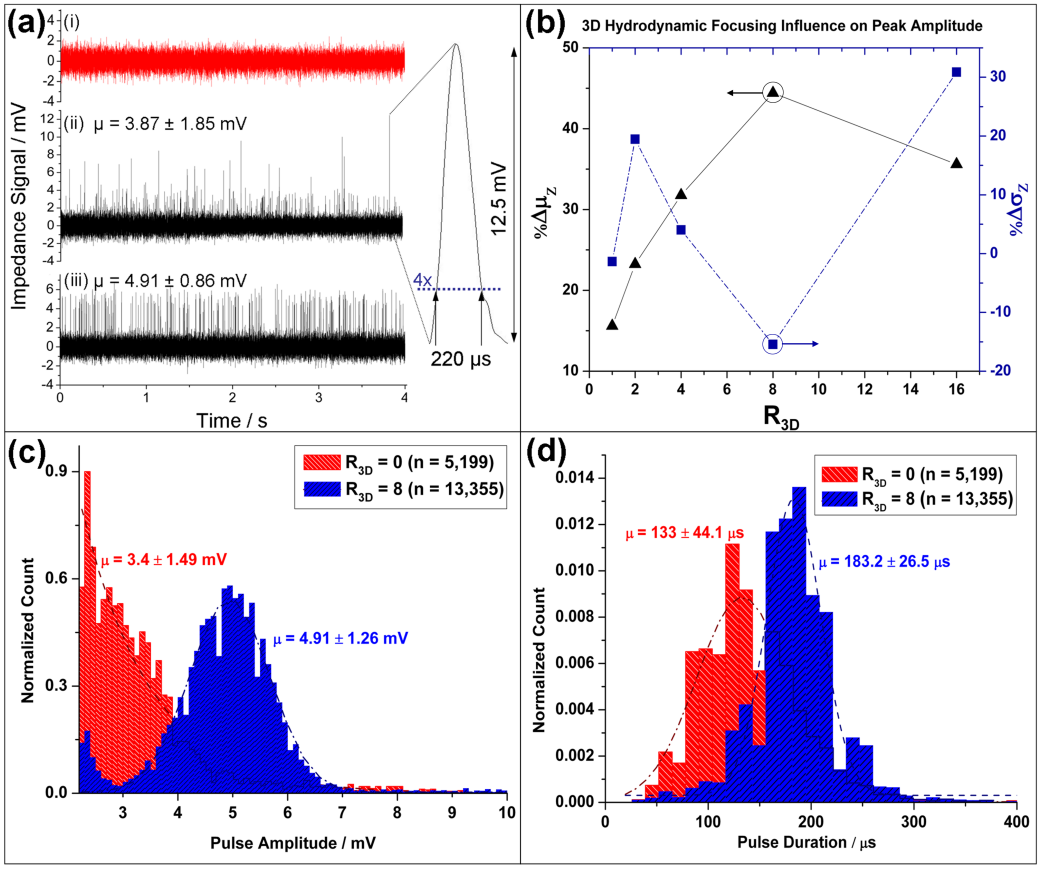

Figure 3.6: Effect of 3D focusing of 7.32 μm polystyrene particles on electrical analysis. (a) (i) Baseline impedance signal (no beads), (ii) signal with beads and no 3D focusing ($R_{3D} = 0$) with pulse amplitude statistics for 4 s duration, and (iii) signal with beads and optimal 3D focusing (R_{3D}= 8) with pulse amplitude statistics. (a, inset) Magnification of a single impedance pulse and the concept of threshold analysis using a trigger that is four times the standard deviation of the noise in (i); pulse duration is calculated from the intersection of the pulse with the trigger, while pulse magnitude is simply the maximum height within the pulse duration. (b) Percent change in mean pulse magnitude, $\%\Delta\mu_Z$ (triangles, solid line), and standard deviation, $\%\Delta\sigma_Z$ (squares, dash-dot line), relative to $R_{3D} = 0$ for various R_{3D} values. Number of triggered events (R_{3D} value in parentheses): n = 5,199 (0), n = 17,157 (1), n = 11,106 (2), n = 11,869 (4), n = 13,355 (8), and n = 3,457 (16). (c) Pulse height distribution comparison between $R_{3D} = 0$ and $R_{3D} = 8$; statistics shown are from raw data; curve fitting is used to show how the distribution drastically changes from decaying exponential for $R_{3D} = 0$ ($R^2 = 0.95$) to Gaussian for $R_{3D} = 8$ ($R^2 = 0.97$). (d) Pulse duration (relative to 4x trigger level) distribution comparison between $R_{3D} = 0$ and $R_{3D} = 8$; statistics shown are from Gaussian curve fittings ($R^2 = 0.94$ for $R_{3D} = 0$ and $R^2 = 0.92$ for $R_{3D} = 8$). For both (c) and (d), an outline of the $R_{3D} = 0$ distribution is shown when it is overlapped by the $R_{3D} = 8$ distribution. From [133] - Reproduced by permission of The Royal Society of Chemistry.

FSC histogram in Fig. 3.7(a) shows the cell size distribution found using the flow cytometer, which can be compared to the pulse height histogram of the electrical microcytometer in (b). There is a noticeable difference between the two histograms in that the FSC histogram contains a secondary peak, which denotes live cells. As previously mentioned, in impedance spectroscopy, cells are treated as non-conducting spheres at frequencies well below f_C. Frequencies higher than f_C effectively short the capacitance of the cell membrane via relaxation mechanisms (β-dispersion) [95], which allows for the investigation of the internal electrical characteristics of the cells such as cytoplasm conductivity and DNA content that could give more insight into whether a cell was alive or dead. In our case, the cells are treated as non-conducting spheres. Therefore, it was necessary to gate whole cells in the LSR II data for a fair comparison with the data from the electrical counter, as illustrated in the inset of Fig. 3.7(a).

The following is our logic in gating whole cells for the flow cytometry data. In flow cytometry, the magnitude of forward scattering depends proportionally on cell size and refractive index, while side scattering depends on the complexity of the cells interior (e.g., granularity) [134]. A whole cell that is dead or dying will have a compromised membrane, allowing surrounding media to enter, which effectively reduces the refractive index of the cell and the level of forward scattering. Side scattering will roughly remain unchanged between living and dead/dying cells because cellular contents still remain intact inside the membrane. Therefore, whole cellular events are gated on the entire FSC range and the limited SSC range ($\sim$375 arbitrary units) as depicted in regions 1 and 2 in the inset of Fig. 3.7(a).

The inset of Fig. 3.7(b) represents the relationship between impedance pulse height and pulse width (measured with respect to 5x trigger) for the microcytometer. It is interesting to note that we observed two different populations for cells analyzed by the electrical microcytometer, which could not be distinguished by the aforementioned pulse height histogram. The events in region 1 show a strong positive correlation between the peak amplitude and duration, which is expected for non-conducting spheres. However, the events in region 2 show a higher variance in duration over a smaller amplitude range. We postulate that these are dead or dying whole cells with compromised membranes or ionic channels. These cells cannot be modeled as non-conducting particles, as electrical conduction can take place within

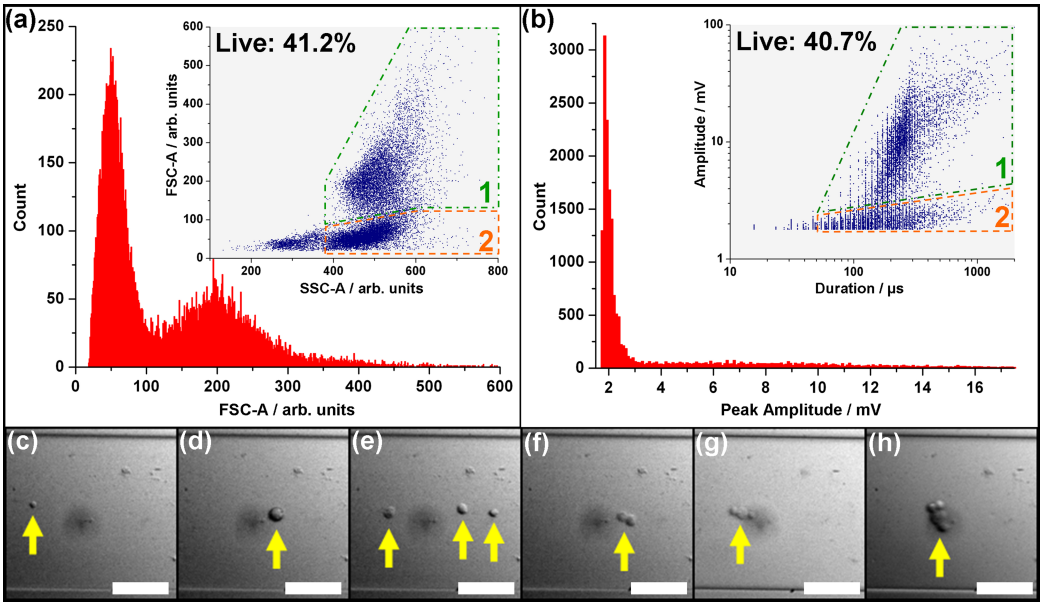

Figure 3.7: Comparison between the analysis of aliquots from the same sample of helper T cells by flow cytometer and electrical microcytometer. (a) LSR II flow cytometer analysis; FSC histogram relates cell size distribution while the inset FSC vs. SSC scatter plot illustrates the two sub-populations of whole cells: living (region 1) and dead/dying (region 2). (b) Electrical microcytometer analysis; pulse amplitude histogram shows cell size distribution; inset scatter plot shows relationship between cell translocation time and peak amplitude, and distinguishes between live (region 1) and dead/dying (region 2) cells. The percent of live whole cells was calculated by dividing the number of events in region 1 by the total number of whole cells (regions 1 and 2). (c - h) Micrographs of focused helper T cells illustrating their large size variation: (c) healthy cell (8.7 μm in diameter), (d) dead/dying cell (18.2 μm), (e) multiple cells flowing in a single-file manner, and clumps of cells as (f) doublets, (g) triplets, and (h) quadruplets. White scale bars are 75 μm. From [133] - Reproduced by permission of The Royal Society of Chemistry.

the cell, reducing the effective impedance of the cell. The large variance in duration in this region can be explained by the fact that the cells were undergoing apoptosis and increased in size. This will increase the translocation time of the cells, but will have little effect on pulse amplitude because of the cells' compromised membranes. Using this theory, we found that the fraction of live T cells found by the microcytometer matched closely with that of the LSR II flow cytometer for a aliquots from the same sample (40.7% vs. 41.2%, respectively). Figure 3.7(c - h) illustrates how cell size can vary from 8.7 μm with a healthy T cell (c), to over twice as large during apoptosis (d), or even larger via clumping of multiple cells (f - h).

Figure 3.8 shows the correlation of 13 concentration values found from the electrical microcytometer and the LSR II flow cytometer. Each point represents one particular dilution that was measured by both methods. The microcytometer proved to perform well for the whole range of concentrations tested, especially in the critical concentration range of < 500 cells$\cdot\mu\mathrm{L}^{-1}$ ($\mathrm{n} = 11$; $\mathrm{R}^2 = 0.95$), even considering that measurements were taken from different aliquots of the same dilution and includes inherent pipetting error.

3.5 Conclusions

We have investigated a microfabricated AC impedance analysis system for the electrical counting of CD4+ T lymphocytes for point-of-care blood analysis. The two-stage 3D focusing mechanism was easily fabricated using a single microfluidics layer, and ensured cells and particles flowed in a single-file line and consistently close to the sensing electrodes. This not only enhanced the sensitivity of the devicegiving CD4+ T lymphocyte counts comparable to an industry standard flow cytometer—but ensured accurate representation of the size distribution of the population, which can help differentiate among different cell types in heterogeneous populations and aid in understanding cell growth cycles in homogenous populations. In addition, we found that it has the capability to differentiate between live cells and those with compromised membranes, providing the possibility of on-chip live/dead cell counts. A simple-to-use handheld device can be realized via a simplified chip or IC-based lock-in amplifier and a miniaturized pumping system. This design will provide an inexpensive and reliable back end to a totally autonomous blood

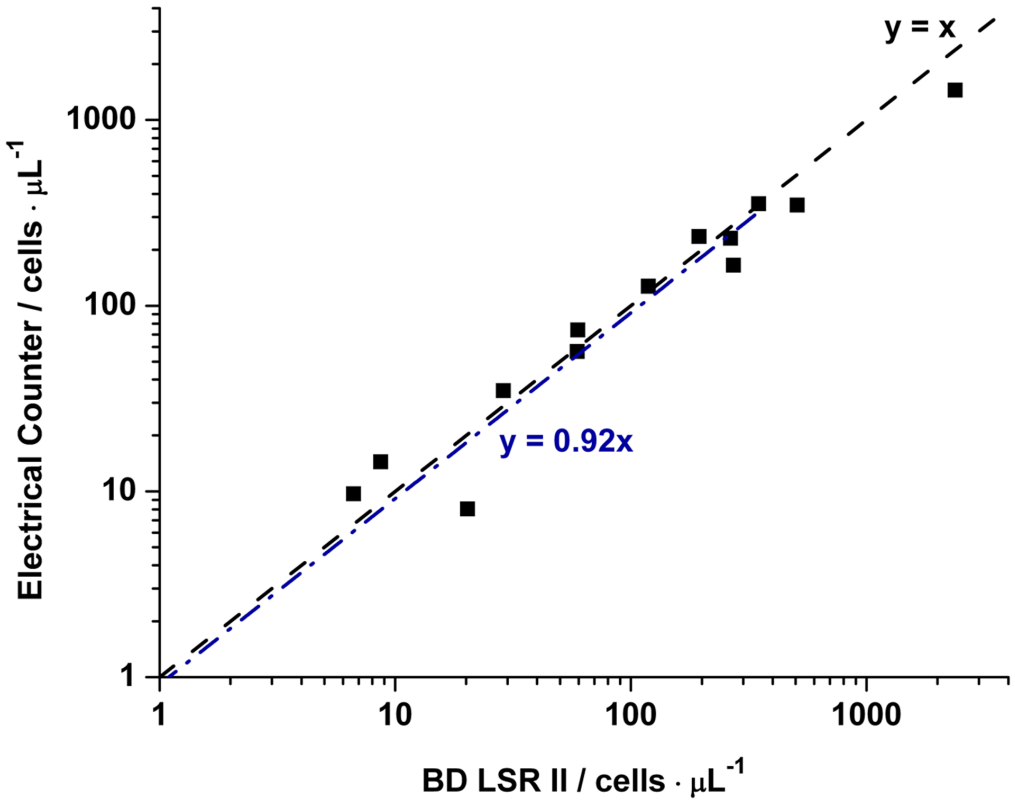

Figure 3.8: Concentration comparison between the electrical counter and the LSR II flow cytometer for the full range of the 13 concentrations analyzed (10 to 2,000 cells·μL^{-1}). The dash-dot line is a linear regression for the 11 samples ($R^2 = 0.95$) within the critical range (< 500 cells·μL^{-1}) and indicates good correlation between the two methods. The dashed line denotes 1:1 correlation between both analysis methods. From [133] - Reproduced by permission of The Royal Society of Chemistry.

cell counter which selectively isolates and subsequently counts a specific cell type for analysis of various diseases.

CHAPTER 4

ELECTRICAL DIFFERENTIAL COUNTER FOR CD4+ T LYMPHOCYTES

4.1 Introduction

The previous chapter showed that it is feasible to obtain accurate counts for homogenous populations of cultured CD4+ T lymphocytes using electrical impedance sensing in a microfabricated biochip [133]. However, a next major step toward a practical point-of-care (PoC) device was needed to selectively enumerate the T cells among the various cell types found in blood. This chapter describes one method in obtaining an absolute CD4 T cell count using a differential counting method with two electrical impedance sensors.

Specifically, we have developed a microfabricated biochip that enumerates CD4+ T lymphocytes from leukocyte populations obtained from partially-processed human blood samples (erythrocytes are lysed off-chip) using electrical impedance sensing and immunoaffinity chromatography. T cell counts are found by obtaining the difference between the number of leukocytes before and after depleting CD4+ T cells with immobilized antibodies in a capture chamber. This differential counting technique has been validated to analyze physiological concentrations of leukocytes with an accuracy of $\sim$9 cells$\cdot\mu$L^{-1} by passivating the capture chamber with bovine serum albumin. In addition, the counter provided T cell counts which correlated closely with an optical control ($R^2 = 0.997$) for CD4 cell concentrations ranging from approximately 100 to 700 cells$\cdot\mu$L^{-1}. We believe that this approach can be a promising method for bringing quantitative HIV/AIDS diagnostics to resource-poor regions in the world.

4.2 Principle

Figure 4.1(a) depicts the microfabricated differential counting device that uses affinity chromatography, electrical impedance sensing, and a reverse-flow method to selectively enumerate CD4+ T cells. The main feature of the chip is its large capture chamber, which is conjugated with anti-human CD4 antibody to selectively isolate and deplete all CD4+ T cells from the heterogeneous leukocyte population, which we have described previously [51]. Monocytes also express the CD4 antigen and bind to the capture region, but can be removed by the application of a controlled shear stress, as monocytes contain an order of magnitude less CD4 surface antigen than T cells [51,136, 137]. The electrical sensors are designed to count individual cells using the Coulter principle, where the passage of a cell perturbs the electrical current within an orifice, creating a distinct impedance pulse. The chip contains two such counters, both configured to measure the relative impedance change caused by the passage of a cell. Specifically, each counter is comprised of three electrodes, configured so that the impedance signal between electrode pairs B and C is subtracted from the signal between pairs A and B (4.1(b, right panel)). This self-referencing design is valuable in impedance spectroscopy in microfluidics [107,138]—and is especially useful in our case, as it identifies which direction cells are flowing within the chip. A single cell entering the chip through the entrance port creates an up-down pulse pair, while cells exiting back out of the entrance port create down-up pulse pairs (Fig. 4.1(b-c, right panel)).

Figure 4.1(b-d) illustrates the reverse-flow differential counting method used to obtain accurate and objective cell counts. Red blood cells from whole blood samples are lysed off-chip, and a pure leukocyte population is injected into the chip's entrance. All white blood cells are counted as they pass through the entrance counter and enter a chamber functionalized with CD4 antibody. This capture chamber depletes CD4+ T cells from the leukocyte population (Fig. 4.1(b)). Flow direction is reversed once cells are detected at the exit counter, and uncaptured or non-specifically bound cells are washed back out of the chip's entrance after being enumerated again by the entrance counter (Fig. 4.1(c)). Figure 4.1(d) depicts a completed experiment in which the capture chamber contains only specifically bound CD4+ cells. The differential count depicts the number of captured CD4+ T lym-

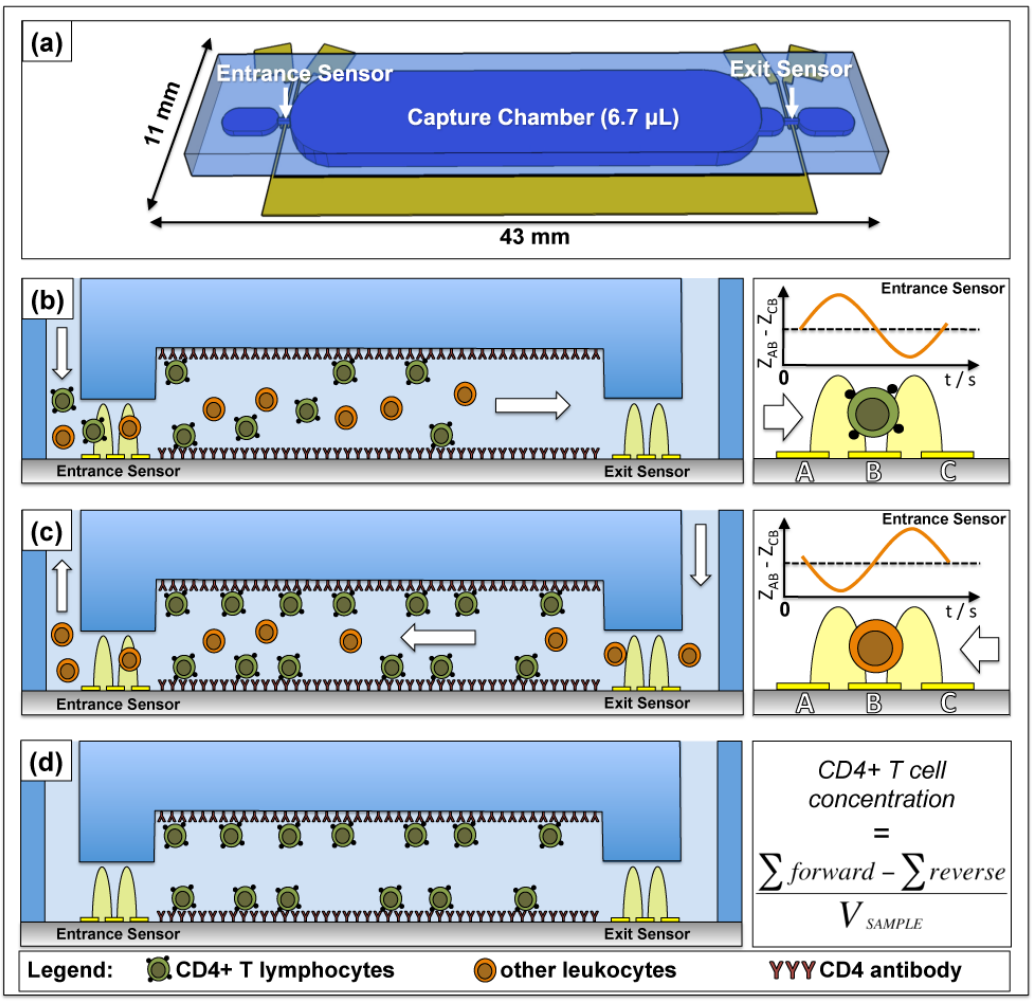

Figure 4.1: Principle of electrical differential counting of CD4+ T cells. (a) Graphically-rendered image depicting the chip's geometry, specifically its two electrical counters and capture chamber. (b-d) Cross-sectional views of the chip during an experiment: (b) forward flow direction to obtain total leukocyte count at the entrance counter, (c) reverse flow direction and enumeration of uncaptured cells after leukocytes reach the exit sensor, and (d) finished experiment after all unbound leukocytes are washed from the capture chamber. The concentration of CD4+ cells can be obtained simply by normalizing the differential count by the known sample volume (d, right panel). The right panels of (b) and (c) illustrate how cell flow direction at the entrance counter can be determined by the change in pulse signature polarity, with the pulse signature changing from up-down (b) to down-up (c) in time. From [139] - Reproduced by permission of The Royal Society of Chemistry.

phocytes by obtaining the difference between the forward and reverse counts. Actual helper T cell concentrations can simply be found by normalizing this difference to the volume of sample flown into the chip.

Although this application is focused on CD4+ T cell enumeration for HIV/AIDS diagnostics, it can be expanded to analyze other cell types simply by choosing different capture antibodies for the particular cell surface antigen of interest.

4.3 Materials and Methods

4.3.1 Channel and Sensor Design

Each counter was comprised of a 15 μm-wide and 15 μm-high microchannel that funneled the cells over three 10 μm-wide platinum electrodes (with 10 μm spacings). The counting channel dimensions were chosen to be large enough to facilitate leukocyte passage without clogging (leukocytes have an average diameter of $\sim$13 μm) [140], but small enough to ensure the cells flowed past the electrodes in a single-file manner with small variation in passage height to ensure consistent enumeration of cells [107,133]. The counting electrodes' dimensions were chosen to provide adequate spatial resolution (50 μm) and to create a sensing region volume of $\sim$11 pL (50 μm x 15 μm x 15 μm), both to ensure coincident events would not occur for leukocyte concentrations up to $\sim$9 x 10^4 cells$\cdot\mu$L^{-1}, well above the 4 11 x 10^3 cells$\cdot\mu$L^{-1} physiological range found in humans [11].

The 50 μm height of the capture region was chosen to provide a large enough sample volume of $\sim$7 μL for an accurate depiction of a patient's health and to ensure proper shear stresses at the fluid-wall interface for optimal CD4+ T cell capture. According to Cheng et al., a shear stress greater than 3 dyn$\cdot$cm^{-2} resulted in less effective CD4+ T cell capture [51]. The equation

$$\tau_w = \frac{6\mu Q}{h^2 w_1} \tag{4.1}$$

can be used to estimate the shear stress at the walls of a rectangular mi-

crofluidic channel of a constant width, ω_1, where μ is the dynamic viscosity of the fluid, Q is the volumetric flow rate, and h is the height of the channel [141]. This shows the sensitive, inverse-squared relationship between the channel height and the shear stress at the chamber's floor and ceiling. If the capture chamber remained the same height as the counter channels (15 μm), the capture chamber would give a shear stress of over 5.5 dyn·cm^{-2} at Q = 5 μL·min^{-1}, which would be over the aforementioned 3 dyn·cm^{-2} upper boundary. However, a 50 μm capture chamber height significantly reduces the average shear stress to 0.5 dyn·cm^{-2}, greatly increasing the interactions between the cells' surface antigens and the immobilized Ab, which facilitate cell capture. The 34 mm capture chamber length ensured sufficient interaction time (∼80 s at sample flow rate of 5 μL·min^{-1} for flowing in a single direction).

Three-dimensional hydrodynamic focusing was desired, as it may result in an increase in impedance pulse signal-to-noise ratio and lessen the possibility of clogging [133]. However, it would have effectively increased the entrance flow rate (∼125 μL·min^{-1} for a 5 μL·min^{-1} cell sample flow rate), resulting in a capture chamber shear stress of 11.1 dyn·cm^{-2}, which is well beyond the maximum to facilitate CD4 T cell capture. In addition, the cell passage time through the 15 μm x 15 μm counter pore at this flow rate would result in transition times faster than 90 ns, which is well below the minimum transition time of ∼2 μs that can be resolved using the lock-in amplifier described in the experimental section. As a result, samples were filtered before infusion into the chip to prevent clogging the 15 μm counting pores. It was found that the 15 μm counting pore height was small enough to ensure cells passed consistently close to the coplanar sensing electrodes to create accurate particle size distributions [133].

4.3.2 Differential Counter Fabrication

Fabrication of the differential counter is illustrated for one counter region in Fig. 4.2(a-g).

The electrical sensing layer was fabricated using the standard metal lift-off process. A 4" glass wafer (Pyrex 7740) was first spin-coated with LOR2A liftoff resist (Microchem Corp., Newton, MA), soft-baked at 183 °C for 5

minutes and then coated with Microposit S-1805 photoresist (Rohm and Haas Electronic Materials, Marlborough, MA). After another soft-bake at 110 °C for 90 s, the wafer was aligned to the electrodes mask on a Quintel Q7000 mask aligner and exposed for a total dose of 2.8 mJ·cm^{-2}. The wafer was then placed on a 110 °C hotplate for a 60 s post-exposure bake before being immersed into Microposit MF CD-26 developer (Rohm and Haas Electronic Materials) for 80 s and rinsed with DI water for 2 minutes (Fig. 4.2(a)). The wafer was then de-scummed in an O2 plasma system for 20 s before being placed in a CHA SEC-6000 evaporator (CHA Industries, Fremont, CA) for the deposition of 25 nm of Ti adhesion layer, followed by a 75 nm Pt conduction layer (Fig. 4.2(b)). The undesired metal was lifted off by placing the wafer in a 70 °C bath of Microchem Remover PG for 15 minutes, creating the necessary conduction paths for the counters (Fig. 4.2(c)).

The multi-height fluidics layer was created by fabricating a negative image of the desired channels using Microchem SU-8 25 photoresist. SU-8 25 was spun on a 4" Si wafer to a height of 15 μm, and was pre-baked in two steps for 2 minutes at 65 °C and then 95 °C for 5 minutes. The wafer was then aligned and exposed to a mask defining all of the fluidic channels, including the capture region, counters, sample inlet and outlet, and antibody functionalization ports (Fig. 4.2(d)). A second layer of SU-8 was spun on to obtain a total thickness of 50 μm for the entire wafer, and was pre-baked first at 65 °C for 5 minutes and then 95 °C for 15 minutes. The wafer was then exposed to a second mask that only defined the capture chamber, allowing it to have a height of 50 μm, compared to the other fluidic regions of 15 μm in height. The wafer was developed in Microchem SU-8 developer for 2 minutes at room temperature, rinsed with isopropyl alcohol, and hard-baked at 125 °C for 15 minutes (Fig. 4.2(e)). Poly(dimethylsiloxane) (PDMS), 1:10 ratio of curing agent to base, was poured over the negative mold and allowed to cure overnight at 65 °C (Fig. 4.2(f)). The polymerized mold was peeled off, and ports were punched for all inlets and outlets using a blunt syringe needle.

A sealed fluidic chip was completed by aligning and bonding the electrode sensing layer to the fluidics layer after oxygen plasma activation in a barrel etcher (Fig. 4.2(g)). Teflon microbore tubing was used to make fluidic connections among the chip, valves, and syringe pumps.

Figure 4.2(h) compares the footprint of the completed chip to a U.S. dime, suggesting that the device could be manufactured as a single-use, disposable

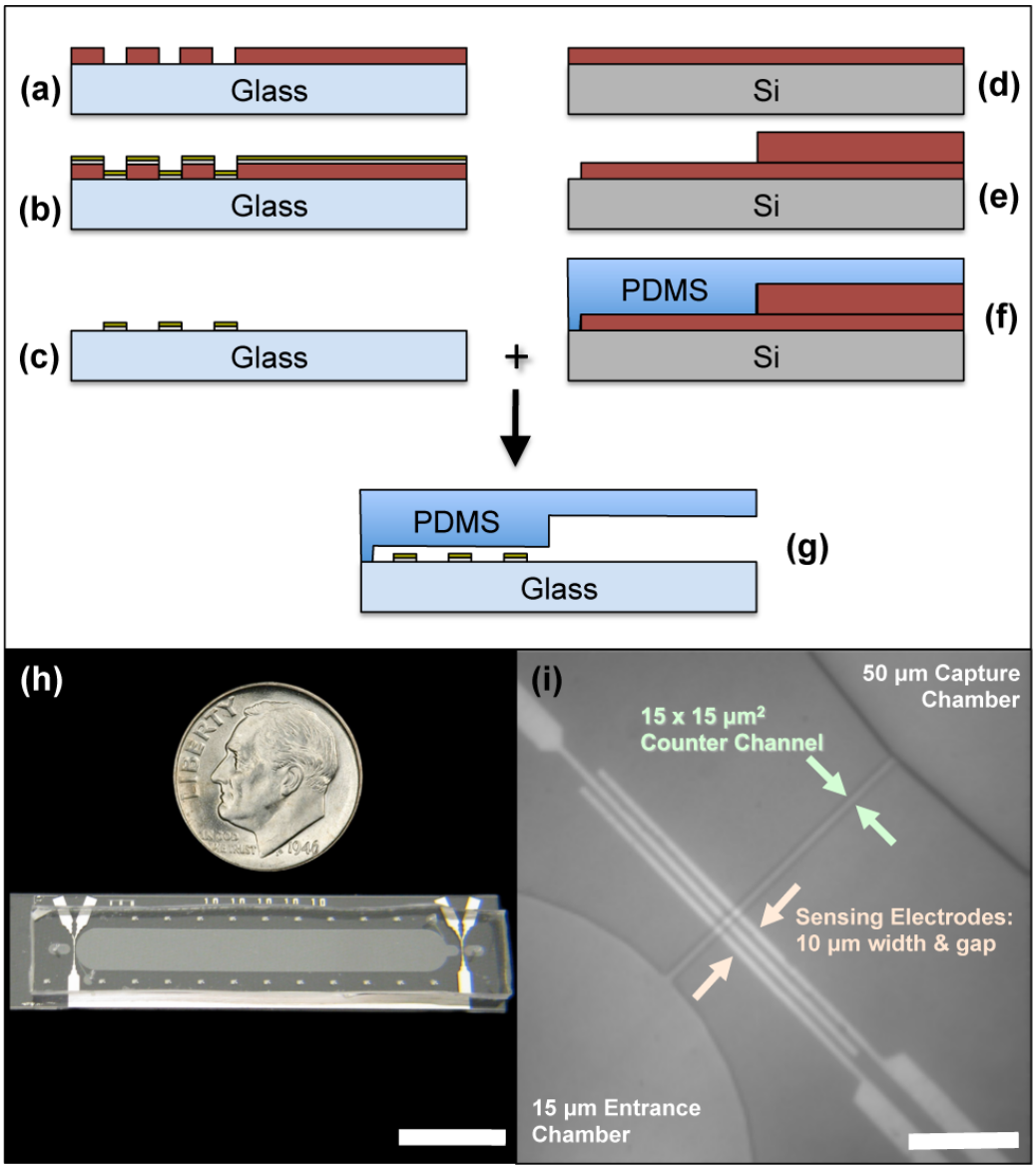

Figure 4.2: (a - g) Microfabrication process flow for the electrical differential counter chip. (h) Fabricated chip compared to the size of a U.S. dime (scale bar length is 10 mm). (i) Micrograph of an entrance counter region, depicting the three-electrodes setup, narrow counter channel, and 50 μm-high capture chamber (scale bar length is 100 μm). From [139] - Reproduced by permission of The Royal Society of Chemistry.

chip. Figure 4.2(i) is a micrograph of the entrance counter region.

4.3.3 Obtaining Purified Leukocytes from Whole Blood

Red blood cells were lysed before flowing samples through the differential counter chip, as the concentration of erythrocytes would be too high to analyze at the desired flow rates and could also introduce additional counting error. On the day of the experiment, 4 mL samples of whole blood from healthy donors were collected in EDTA-coated Vacutainer tubes (BD Biosciences, Franklin Lakes, NJ). Twelve mL of lysis solution (0.12 % (v/v) formic acid and 0.05% (w/v) saponin in DI) was added to 1 mL of whole blood and incubated for 6 seconds with agitation. Lysis was immediately stopped by the addition of quenching solution (5.3 mL of 0.6% (w/v) sodium carbonate and 3% (w/v) sodium chloride in DI) [117]. The solution was centrifuged for 5 minutes at 200 x gravity at room temperature, supernatant was aspirated, and the leukocyte pellet was resuspended in 5 mL PBS + 1% (w/v) bovine serum albumin (BSA). The suspension was centrifuged again and resuspended in 1 mL PBS + 1% BSA, giving the physiological concentration of white blood cells. The volume of resuspension PBS was also varied to provide different leukocyte concentrations. The saponin/formic acid lysing method was chosen because it proved to be the most rapid and effective erythrocyte lysis technique and ensured cell sample concentrations were low enough to be successfully analyzed by the electrical counter (see 4.3.5). However, this aggressive lysing method has been known to differentially damage the membrances of leukocyte subtypes with possible loss of viability [117]. Flow analysis showed that the saponin/formic acid lysis agent did decrease the total leukocyte concentration when compared to a commercially available solution (BD Pharm LyseTM, BD Biosciences), but T lymphocyte and monocyte populations were not affected. This held true even for varying the duration of incubation in the lysis solution (3 s to 18 s). Leukocyte vitality was preserved by resuspending the cells in a PBS + 1% BSA solution immediately after halting the lysis process with the quenching solution.

4.3.4 Experimental Setup and Reverse-Flow Differential Counting Technique

Figure 4.3 illustrates the experimental setup and process used to differentially count CD4+ T cells. The process can be split into two segments: forward flow (Fig. 4.3(1)) and reverse-flow analysis (Fig. 4.3(2)). A Harvard Apparatus (Holliston, MA) PicoPlus syringe pump injected a constant stream of leukocytes into the chip through the entrance counter at 5 μL·min^{-1} to create a forward count of all leukocytes. The enumerated cells entered the CD4 capture chamber and were depleted of CD4+ T cells. Forward flow continued until cells were detected at the exit counter. At this time, flow direction was reversed by switching the entrance and exit valves and by initiating the PBS + 1% BSA solution wash pump at 5 μL·min^{-1}. The unattached leukocytes were washed back out the capture chamber and entrance counter to be enumerated, creating a reverse count. The total number of captured CD4+ T lymphocytes could be simply calculated by subtracting the reverse count from the forward count.

Counting was performed using a Zurich Instruments (Zurich, Switzerland) HF2LI dual lock-in amplifier which injected a 5 V (rms) 1.1 MHz AC signal into the entrance and exit counters (*VOUT_1* and *VOUT_2*, respectively). Relative impedance was measured using three microelectrodes set up in a Wheatstone bridge configuration, balanced with 10 kΩ resistors (R) and a 68 pF capacitor. For each counter, the voltage signal across each resistor was subtracted (*i.e.*, *V2 – V1*, or *V4 – V3*) using a differential preamplifier before entering the lock-in's input. An increased sensitivity and stable impedance signal were two of the benefits of this balancing bridge method, but the major advantage of the three-electrode configuration was that one could precisely and accurately determine when the forward counting stopped and reverse counting started, as already described.

The bridge potential difference signals for the entrance and exit counters were input into the HF2LI, and the impedance magnitude and phase angle (R and θ, respectively) were output to a computer for real-time observation and recording of data at a 200 kHz sampling rate using a National Instruments (Austin, TX) PCI-6351 DAQ card and Lab-VIEW software. The data was imported into and analyzed with Clampfit software. Impedance pulses were counted using a threshold detection method, and forward and reverse counts

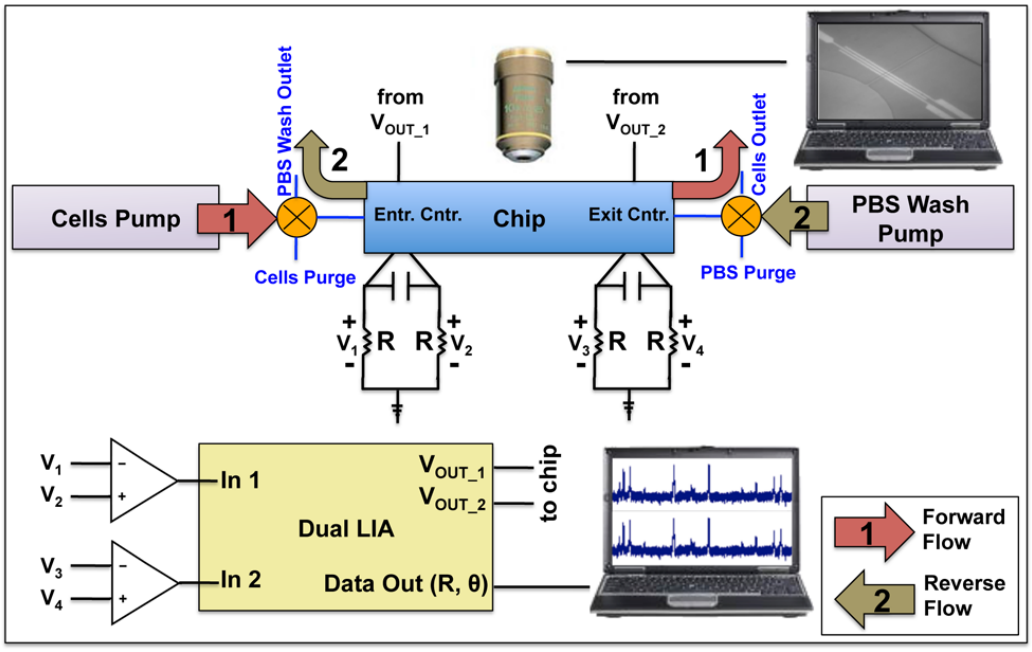

Figure 4.3: Experimental setup and process for electrical differential counting of CD4+ T cells. A dual lock-in amplifier is used to inject an AC signal and monitor its change through the chip's counter regions, which are balanced by a Wheatstone configuration. Process: (1) the cells pump injects leukocytes into the chip (forward direction) to be enumerated at the entrance counter; (2) after cells are sensed at the exit counter, both valves are switched to reverse flow direction and the PBS wash pump purges the capture chamber of uncaptured cells, which are enumerated again by the entrance counter. From [139] - Reproduced by permission of The Royal Society of Chemistry.

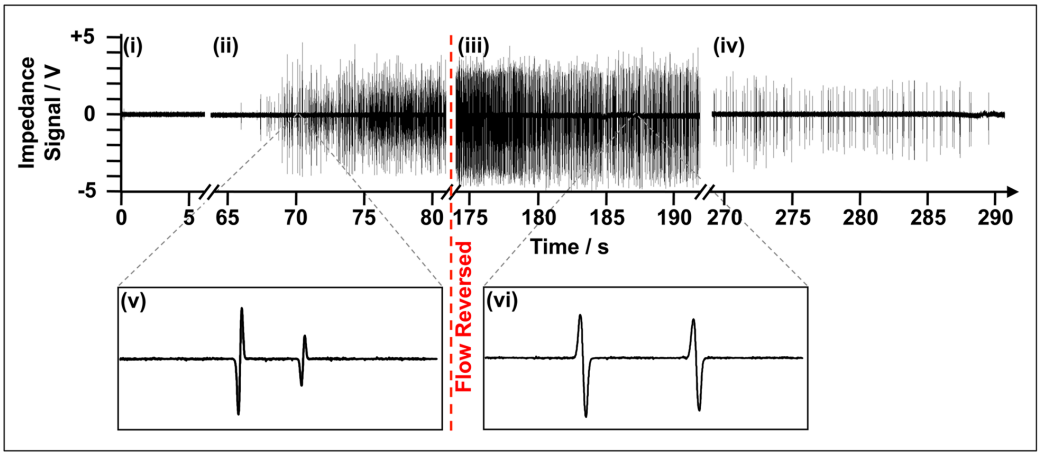

Figure 4.4: Impedance data of the entrance counter for the entire duration of a reverse-flow differential counting experiment. The data can be separated into four regimes: (i) no cells present, (ii) cells beginning to enter the chip's entrance, (iii) just after reversing flow and counting cells exiting back out the entrance, and (iv) near the end of purging the capture chamber of uncaptured cells. Magnifications of the impedance signal during forward (v) and reverse flow (vi) show how pulse signature polarity can be used to ensure when reverse counting begins. From [139] - Reproduced by permission of The Royal Society of Chemistry.

were compared.

Another computer connected to a digital camera on a Nikon Eclipse E600FN microscope (Nikon Instruments, Inc., Melville, NY) was used to observe cell passage through the channels as well as cellular interactions with the capture chamber's walls.

Figure 4.4 shows an example of the reverse-flow differential counting method from actual experimental data. Flow reversal caused impedance pulses to invert polarity from down-up (v) to up-down (vi), exhibiting a straightforward method to differentiate between cells entering and exiting the chip.

4.3.5 Maximum Pulse Density Limit

It is imperative that the differential counter can analyze physiological concentrations of white blood cells ($\sim$1 x 10^4 cells$\cdot\mu L^{-1}$) flowing at the desired rate of 5 – 10 μL$\cdot$min^{-1}. This flow rate range would provide as rapid sample analysis as possible, given the limitations of (1) creating a capture chamber shear stress < 3 dyn$\cdot$cm^{-2}, (2) ensuring the capture chamber volume is

large enough to contain an adequate sample volume ($\geq$ 5 μL), (3) creating a capture chamber (and chip) footprint that would be amenable to PoC applications (smaller than a microscopy slide, $\sim$75 mm x $\sim$25 mm), and (4) ensuring the pulses are not attenuated by the lock-in amplifier's low pass filter (in our case of AC analysis). In the last case, as flow rate is increased, impedance pulses become shorter in duration and contain mostly frequency components that exceed the filter's bandwidth. These components are attenuated, resulting in diminished pulses that cannot be detected above the baseline noise level.

A maximum pulse density (pulses$\cdot$s^{-1}) must be found to test whether the electrical counters can accurately count physiological concentrations of leukocytes at the aforementioned flow rate range. Some limiting factors for accurate counting in any electrical cytometer are (1) the concentration of cells in the sample, (2) the speed in which they flow through the sensor, and (3) the measurement system's sampling frequency. As the concentration of cells increases at a constant flow rate, the duration between passage events decreases. Eventually, the concentration becomes high enough where two cells will be in the same sensing region, creating coincidence events that cause two impedance pulses to overlap. For a finite sampling frequency–even if the cells are not coincident within the sensing region–a high enough velocity will eventually cause overlap of the pulses from two subsequent cell passages.

Hence, we found the maximum pulse density by flowing increasing concentrations of blood cells into the chip until noticeable pulse overlap occurred (*i.e.*, an up-down or down-up pulse signature was not completed before another cell passed through the sensing region).

4.3.6 Direct-Flow Differential Technique

The described reverse-flow differential counting technique was implemented in response to problems found using a simpler flow-through method, where flow was constant in one direction and *both* entrance and exit sensors were used to *quantify* the number leukocytes before and after depletion of CD4+ T cells, respectively (Fig. 4.5). The difference in the electrical characteristics between each counter and its respective external circuitry made it impossible to objectively compare the counting results between both counters. Although

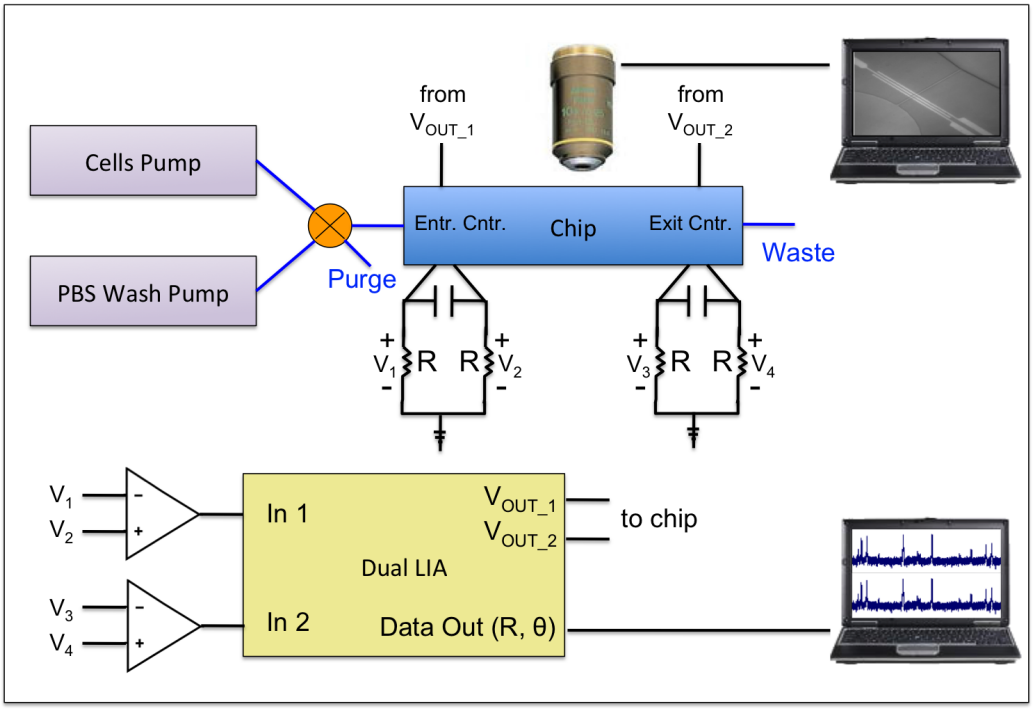

Figure 4.5: Direct-flow differential sensing method. White blood cell populations were flowed directly from chip entrance to exit. The differential count was obtained by subtracting the exit count from the entrance count. The difference in counter sensitivities prevented this as a feasible method to obtain CD4+ T lymphocyte counts.

both counters could detect cell passage, their sensitivities differed enough to make subsequent analysis subjective. For example, the average impedance pulse height at the entrance counter may be lower than that found at the exit counter for the same population of cells or beads with the capture chamber passivated from specific and non-specific adsorption. Ideally, both counters would have the same sensitivity and produce the same average impedance pulse heights for identical populations, resulting in a differential count of zero. However, using the same threshold trigger level (determines at what height an impedance pulse is a cell) would result in the non-real result of a larger exit count than entrance count—a negative differential count. Scaling the trigger level based on average pulse height, noise level, and other variables proved unsuccessful and subjective, precluding further application.

The reverse-flow differential counting method would remove the ambiguity in electrical analysis and lessen the counting error by using the entrance counter alone to enumerate cells entering and exiting the chip. Because only

one sensor is being used, the same threshold trigger level can be used for both the forward and reverse counts, resulting in a more straightforward and objective method to obtain differential counts. The exit counter would only be used as a qualitative means to determine when to reverse fluid flow direction to prevent cells from being lost through the chip's exit and to initiate reverse counting.

4.3.7 Reverse-Flow Differential Technique Validation

Experiments were designed to evaluate the plausibility of the reverse-flow differential counting technique and to quantify its inherent error. This can be found by passivating the capture chamber from any cellular interactions—specific and nonspecific—and performing differential counts of leukocyte populations. Ideally, a passivated capture chamber would result in equal forward and reverse counts (a differential count of zero), but error may come from imperfections in the passivation layer, cell disruption inside the capture chamber, and the electrical analysis itself.

The capture chamber was passivated by flowing in phosphate buffered saline (PBS, pH 7.4), with 1% BSA (A3059-50G; Sigma-Aldrich, St. Louis, MO) and incubating for at least one hour at room temperature to prevent the non-specific adsorption of cells. BSA is a well-known protein for surface passivation, and readily binds to the hydrophilic glass substrate at pH 7.4.36 The passivated chip was then evaluated using the reverse differential counting technique, described above, for various leukocyte dilutions.

4.3.8 Capture Chamber Modification for CD4+ T Lymphocytes

Other experiments were performed to enumerate CD4+ T lymphocytes in the heterogenous leukocyte populations by selectively immobilizing them in the capture chamber, which was functionalized with CD4 antibody.

Purified mouse antibody to human CD4 (MHCD0400) from Invitrogen, diluted (1:10) in PBS, was flown through a newly fabricated chip until the entire capture chamber was filled. Flow was stopped, and the solution was allowed to incubate at room temperature for 30 minutes, followed by two

more filling plus incubation cycles. A solution of PBS + 1% BSA was used to wash away unbound CD4 antibody and block any unconjugated sites from the nonspecific binding of cells. Chamber functionalization was performed either immediately before flowing leukocyte samples or the day before with the functionalized chip stored overnight at 4 °C.

4.3.9 CD4+ T Lymphocyte Count Comparison with Optical Control

An optical counting method using image processing was implemented to evaluate the electrical microcytometer chip's differential counting technique. Immediately after electrical differential counting was finished, the chip's entire capture region was sequentially imaged using an Olympus (Tokyo, Japan) IX81 inverted microscope with phase contrast under a total magnification of 64. Images were merged using standard imaging software, and cells were automatically enumerated in ImageJ to find the actual number of cells that were captured. This count was then compared with the electrical differential count.

4.3.10 Cell Capture Efficiency

A BD Biosciences LSRII flow cytometer was used to quantify the efficiency of the chip in capturing CD4+ T lymphocytes. Two leukocyte populations were analyzed: cells before flowing into the chip and cells that have exited the chip after a differential counting experiment. Alexa Fluor® 488-conjugated mouse antibody to human CD4 (MHCD0420) was purchased from Invitrogen. Phycoerythrin-Cy7 (PE-Cy7™)-conjugated mouse antibody to human CD14 (25-0149-42) and peridinin chlorophyll protein-cyanine 5.5 (PerCP-Cy5.5™)-conjugated mouse antibody to human CD3 (45-0037-42) were purchased from eBioscience (San Diego, CA). Both populations were stained with a cocktail of the above labels by following the manufacturer's suggested protocols, rinsed with centrifugation (200 x g, 5 minutes), and resuspended in PBS for flow analysis to compare the percentages of CD4+ T lymphocytes (CD3+CD4+CD14-) in both populations.

4.3.11 Cell Capture Purity

After optical control micrographs were obtained, the captured cells were fluorescently labeled to examine their phenotype and to understand the capture purity of the system (*i.e.*, the ratio between CD4+ T lymphocytes captured and total cells captured). Alexa Fluor® 488-conjugated mouse antibody to human CD4 (MHCD0420), allophycocyanin (APC)-conjugated mouse antibody to human CD14 (MHCD1405), and 4',6-diamidino-2-phenylindole (DAPI, D21490) were purchased from Invitrogen (Carlsbad, CA). The CD14 antibody was used to determine which CD4+ cells were monocytes, which express both the CD4 and CD14 surface proteins. DAPI was used to determine which cells were nucleated, in the case un-lysed erythrocytes were nonspecifically captured. A 1:20 cocktail of the above three fluorophores was created in PBS and flown into the chip at 2.5 μL·min^{-1} for a total volume of 50 μL. Flow was stopped and the mixture was allowed to incubate for 30 additional minutes. This was followed by a 5 μL·min^{-1} wash with PBS + 1% BSA to ensure unbound labels were purged from the chip. Fluorescent micrographs of selected areas of the chip were taken to create a representative of the entire population using the Olympus IX81 with appropriate fluorescent filter sets at a total magnification of 320.

4.4 Experimental Procedures

4.4.1 Maximum Pulse Density Limit

Varying dilutions (1:1000 to 1:100) of whole blood were injected into a chip at a constant flow rate of 5 μL·min^{-1} to test the pulse density limits (pulses·s^{-1}) of the differential counter. Flow direction was not reversed (kept in forward direction), and pulses were only analyzed for the entrance counter. Pulse density was calculated by normalizing the total number of pulses found by the number of fixed time windows that were applied at random points in the raw data.

Figure 4.6 compares the cell concentration found using the chip (calculated by the number of pulses for a known volume flown) versus the calculated concentration of each sample dilution, assuming the concentration of whole

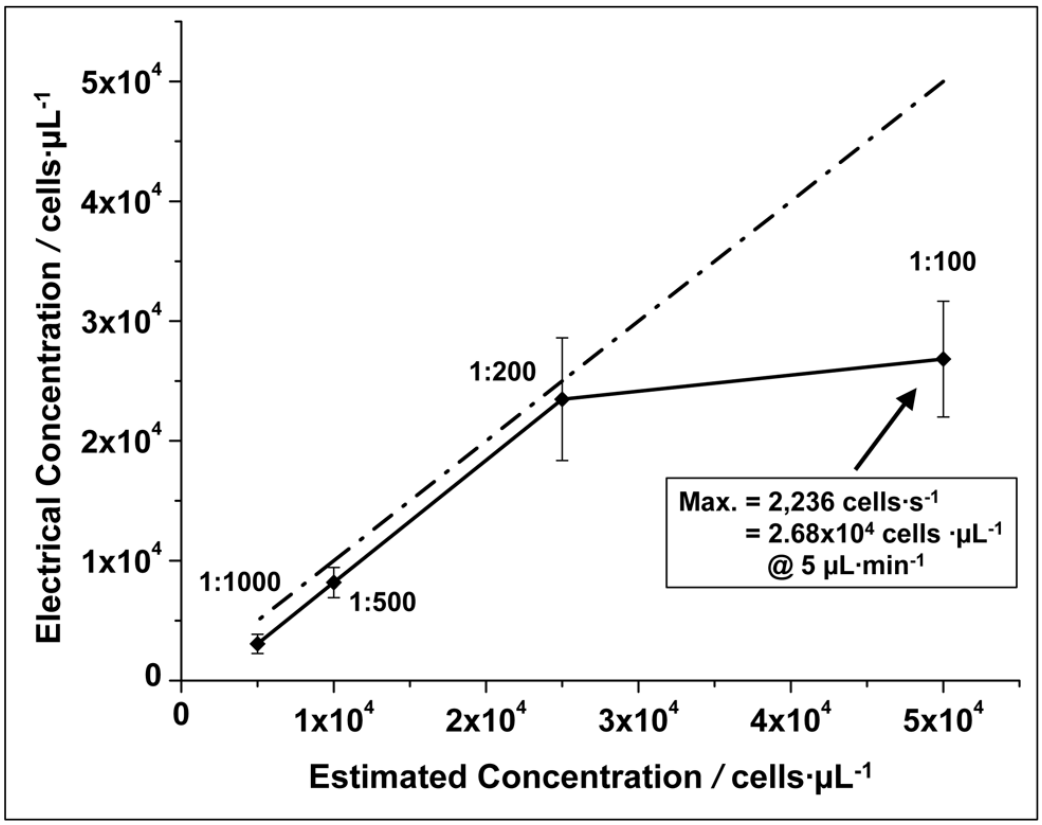

Figure 4.6: Maximum pulse density characterization. Concentration calculations were based on the number of pulses·s^{-1} for a known flow rate. Error bars represent the standard deviations obtained from measurements of 9 (1:1000), 14 (1:500), 25 (1:200), and 23 (1:100) duration windows. From [139] - Reproduced by permission of The Royal Society of Chemistry.

blood was 5 x 10^6 cells·μL^{-1}. At a 5 μL·min^{-1} flow rate, the chip could handle the 1:200 dilution of whole blood ($\sim$2.5 x 10^4 cells·μL^{-1}), but failed to count every pulse individually for the 1:100 dilution ($\sim$5 x 10^4 cells·μL^{-1}) because of pulse merging. The maximum pulse density the chip could handle was 2,236 cells·s^{-1}, equivalent to a concentration of 2.68 x 10^4 cells·μL^{-1} at a flow rate of 5 μL·min^{-1}. While in some pathologic conditions physiological leukocyte counts can exceed this threshold, the vast majority of leukocyte counts will be lower. This maximum pulse density also confirms that effective lysis of erythrocytes is necessary before sample entry to avoid cell counting error.

A possible explanation for the discrepancy between the theoretical (9 x 10^4 cells·μL^{-1}) and the observed concentration maxima (2.68 x 10^4 cells·μL^{-1}) is the theoretical calculations assumed an even distribution of cells in the sam-

ple volume. However, cells may not be evenly distributed at the microscale, as they could travel in packets that result in coincidence events (multiple cells in the sensing region). This is likely with the higher concentrations (*i.e.*, 1:100) and effectively reduced the maximum cell concentration that the electrical counters could handle.

The sampling frequency (115.2 kHz was used in this particular experiment) was not a limitation, as cell velocity through the sensing region (370 $\text{mm}\cdot\text{s}^{-1}$ for $Q = 5\ \mu\text{L}\cdot\text{min}^{-1}$) was not high enough to cause two pulse signatures to overlap from consecutive cell passages. Cell translocation time through the sensing region was 135 μs, or $\sim$15 data samples. This was well above our estimated minimum of 5 samples needed to resolve the passage of a cell and to distinguish between two different cells—as long as they were not simultaneously within the sensing region. (This estimated minimum sample number was determined by assuming distinct cell passage could be resolved if impedance signal values were recorded at the (1) baseline immediately before cell passage, (2) first peak (positive- or negative-going), (3) baseline between peaks, (4) second peak (opposite the polarity of the first peak), and (5) baseline after both peaks.)

4.4.2 Aggregate Shearing Mechanism

The reverse-flow differential counting technique should ensure much smaller error than its direct-flow counterpart by using a single counter to enumerate white blood cells entering and exiting the chip. However, preliminary passivated capture chamber experiments showed a large discrepancy existed between entrance and exit counts. Figure 4.7 illustrates a typical result for a negative control experiment. Ideally, the entrance and exit sums should be equivalent at the end of the experiment, but have a difference of over $\sim$3,500. It is interesting to notice that the exit count is higher than the entrance count, which is true for the 1:1 dilution of white blood cells, but not as dominant in lower leukocyte dilutions. Figure 4.8 shows the relationship between the white blood cell concentration and the difference between the exit and entrance counts for various trigger levels. A trigger level is the voltage threshold that determines whether an impedance pulse is a cell, and is set manually in Clampfit. It is a common convention to base the trig-

ger level off of the standard deviation of the baseline signal's noise (with no cells present). In the case of this experiment, a trigger level of ten times the standard deviation (SD) of the noise was the minimum threshold that could be used to ensure baseline noise pulses were not counted as cellular events. The threshold level for the entrance and exit counters is identical. A noticeable trend is the less diluted samples intersect the X-axis (Entrance - Exit = 0) at higher threshold values (67 x SD for 1:1; 40 x SD for 1:2; 20 x SD for 1:5) in the direction of increasing trigger level value (left to right). This, combined with the fact that the exit count is higher than the entrance count, can explain the large discrepancy in the entrance and exit counts. Cell aggregates form more frequently as the concentration of the purified leukocytes increases because there is more interaction between cell surfaces. These aggregates pass through the entrance counter port and its relatively high shear stresses (1,320 dyn·cm^{-1}) separate the aggregates back into individual cells, which are then counted by the exit counter. An aggregate is counted as a single entity by the entrance counter, but can become three or more entities by the time it reaches the exit counter. The entrance and exit counts only become equal when the threshold level is large enough to not count smaller entities such as single cells, and only counts larger objects that remain physically after passing through the entrance counter.

The aggregation of leukocytes prevents a true evaluation of the differential counter and can be remedied by larger dilutions. However, diluting has several drawbacks, most importantly, analyzing only a fraction of the cells needed to provide a more robust helper T cell test and requiring a much larger chip volume. Therefore, it is necessary to have the physiological concentration of white blood cells enter the chip, and can possibly still be allowed using a microfabricated 10 μm x 13 μm PDMS/glass pore, or "shearer", to separate cell aggregates before the chip entrance. Figure 4.9(a) shows the results after repeating the passivated experiment for 1:1 diluted leukocytes. The shearer proves to decrease the amount of aggregates before entering the differential counter chip (X-intercept at 9 x SD vs. 12.5 x SD for cell samples injected directly into the chip without the shearer). Figure 4.9(b) shows the difference in cell size (pulse amplitude) and cell passage duration when using the shearer. The population undergoing shear before making it to the entrance counter is a tighter distribution at lower pulse duration with similar pulse height amplitude as the un-sheared population because the larger ag-

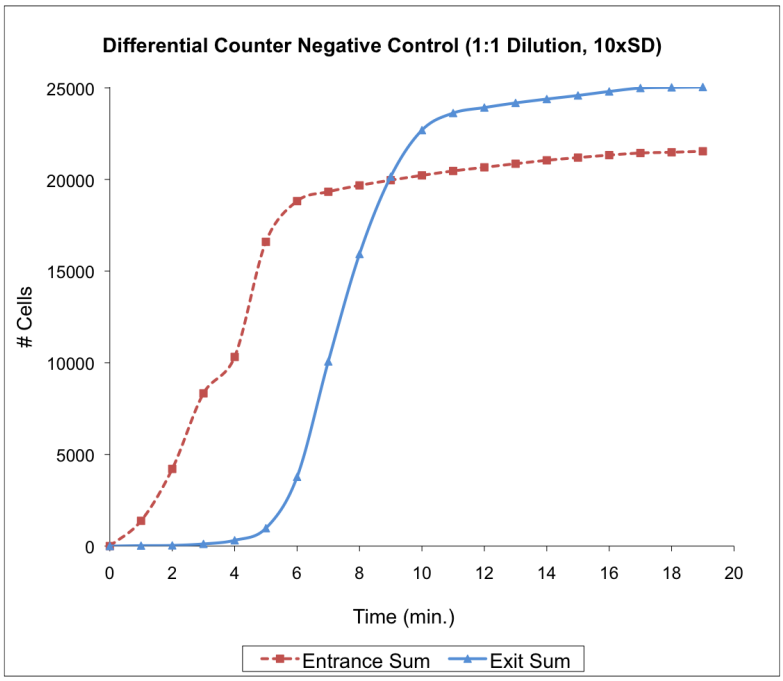

Figure 4.7: Representative entrance and exit count for the passivated capture chamber experiment. The larger difference count may be attributed to the aggregation of the more concentrated white blood cell solutions.

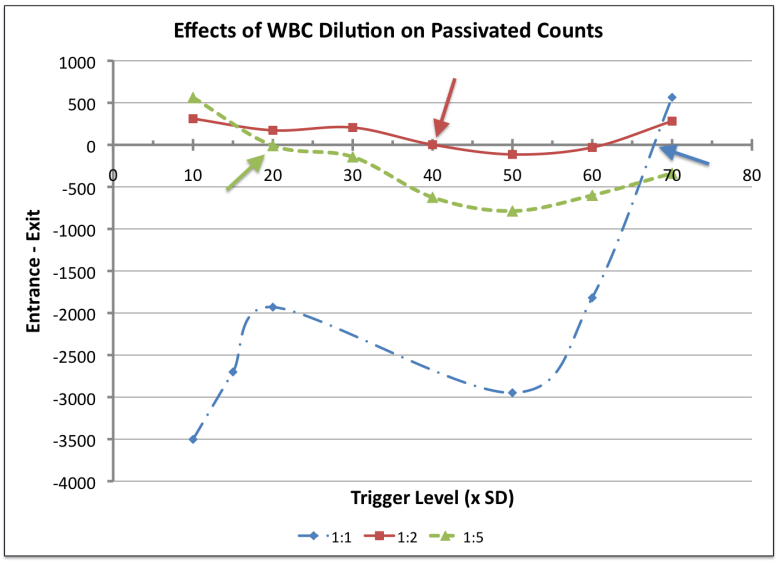

Figure 4.8: Relationship between white blood cell concentration and the discrepancy between the entrance and exit counts. Increasing trigger threshold levels eventually results in a matched entrance and exit count, as depicted by arrows.

gregates block the impedance sensing region longer. The amplitude does not change much because even the single cells are large enough to block most of the electrical current passing between the sensing electrodes. Figure 4.9(c) illustrates the size and passage duration similarities of cells that have been sheared prior to and counted at the entrance sensor and cells that did not undergo pre-chip shearing, but pass through the entrance counter pore and are counted at the exit counter. This shows that the entrance counter indeed is shearing aggregates into smaller entities, performing the same job as the pre-chip shearer. It is therefore necessary to have the shearing unit placed before the chip to ensure most aggregates are separated into single cells.

4.4.3 Reverse-Flow Differential Technique Validation

Figure 4.10(a) illustrates the results for 14 experiments on the analysis of leukocyte populations using the reverse differential counting method with a passivated capture chamber. Leukocyte sample dilutions ranged from 0.25 to 2 times the physiological concentration to understand the inherent error of the device and technique for a range of leukocyte counts. The percent error decreased for larger forward counts (*i.e.*, leukocytes entering the chip), which is desirable for clinical situations where samples will contain physiological concentrations of leukocytes. The main reason for this was that the absolute counting error remained roughly constant for the entire forward count range. (The percent error here is the absolute counting error normalized by the forward count, while the absolute counting error is the absolute difference from the ideal differential count of zero.)

Figure 4.10(b) illustrates the accumulated forward and reverse counts during the experiment highlighted in Fig. 4.10(a). This demonstrates how the reverse count eventually leveled off and became close to the forward count, resulting in an absolute counting error of 71 cells that equates to a 1.2% error.

Table 4.1 quantifies the data in Fig. 4.10(a), and affirms that larger leukocyte counts ($>$ 2,000 cells) resulted in a smaller percent error ($\sim$1.2%). The absolute counting error for this range of forward counts was $\sim$46 cells. The significance of this small error can best be expressed by normalizing it to the estimated 5 μL injected sample volume, resulting in a concentration accuracy

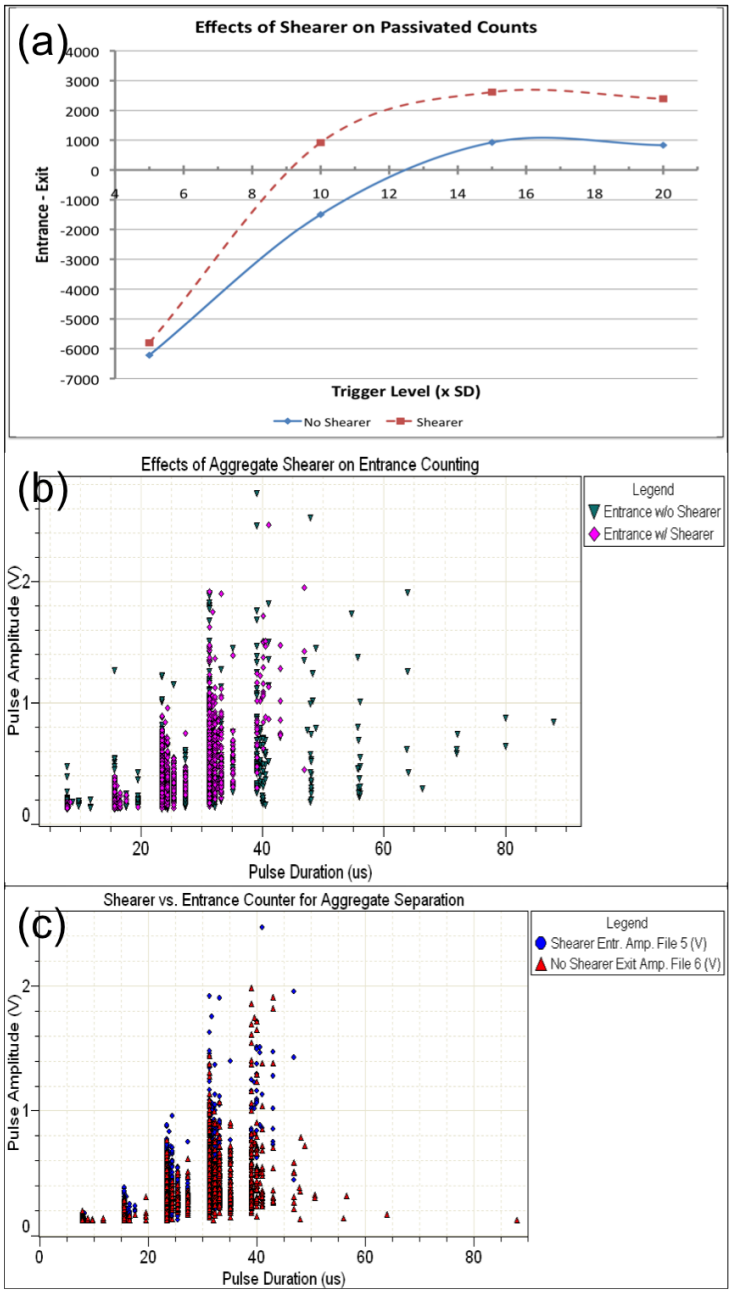

Figure 4.9: (a) Effects of shearer on differential cell counts at various trigger levels. (b) The reduction of aggregates by the shearer are demonstrated by the localization of cellular events at lower pulse durations at the entrance counter, compared to the wider range of durations found without using a shearer module. (c) The pulse amplitude/duration distributions are similar for cells counted by the entrance counter after the shear module and cells counted at the exit counter after passing through the entrance counter (with no shearer module).

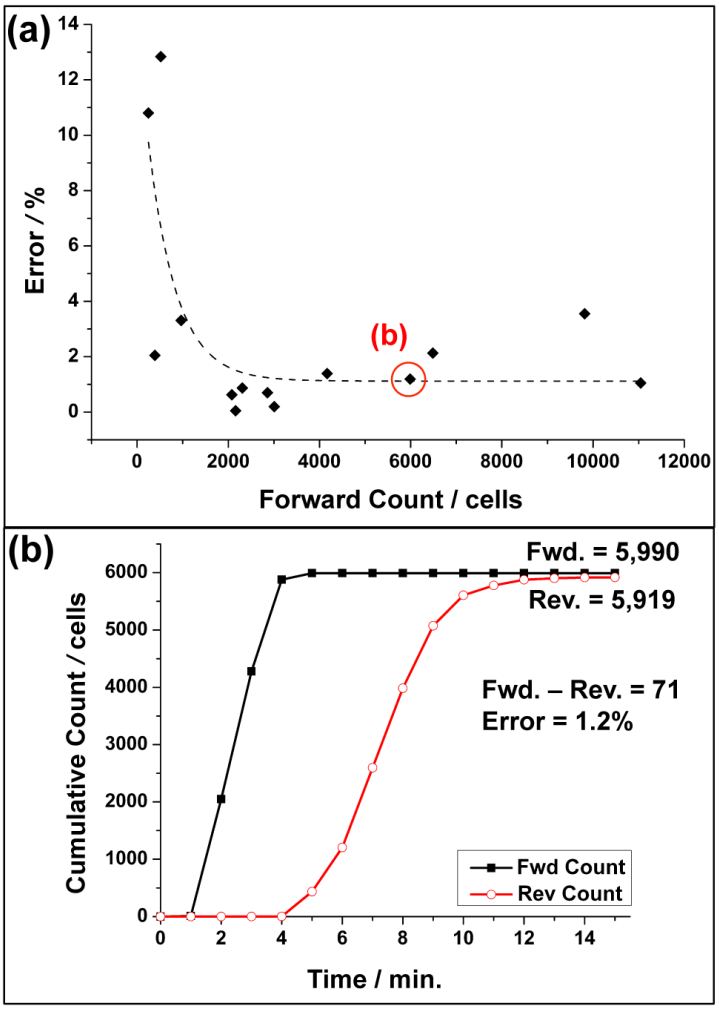

Figure 4.10: Analysis of reverse differential counting for a passivated capture chamber. (a) Percent error decreases exponentially (dashed line, R^2 = 0.57) as the number of leukocytes entering the chip (forward count) increases. (b) Cumulative counts of forward and reverse-flow regimes for the particular experiment highlighted in (a). Error is calculated by normalizing the differential count (absolute difference between the forward and reverse counts) to the forward count. From [139] - Reproduced by permission of The Royal Society of Chemistry.

of $\sim$9 cells$\cdot\mu$L^{-1}. This not only validates the differential counter as a plausible CD4+ T cell enumeration method, but opens the possibility of analyzing patients with advanced AIDS, who may have CD4+ T cell concentrations $<$ 50 cells$\cdot\mu$L^{-1}.

Table 4.1: Error analysis of electrical differential counting of leukocytes using a passivated capture chamber. $\overline{x}$ denotes sample mean. From [139] - Reproduced by permission of The Royal Society of Chemistry.

	Error (%)		Abs. counting error (cells)		Est. conc. accuracy (cells per μL)	
	$\overline{x}$	SD	$\overline{x}$	SD	$\overline{x}$	SD
All WBC	2.91	3.93	44.2	31.3	8.84	6.26
WBC $<$ 2,000	7.25	5.37	38.8	25.0	7.76	5.00
WBC $>$ 2,000	1.18	1.02	46.4	34.5	9.28	6.90

Although the capture chamber volume was $\sim$7 μL (Fig. 4.1(a)), we can only estimate that approximately 5 μL of sample entered the chamber before flow was reversed to prevent the loss of cells. This is because cell sample diffusion resulted in a lower concentration of cells reaching the exit counter before the more concentrated cell population completely filled the chamber. Estimation was made by observing the portion of the capture chamber filled with the concentrated cell population.

The counting error was caused mainly by non-specific adsorption of cells onto the chamber surface, despite passivating the capture chamber with BSA. Passivation using more incubation time and/or PBS with a pH closer to BSA's isoelectric point of 5 would substantially decrease this error and further emphasize the accuracy of this enumeration technique [142]. Another possible source of error may be dead/dying cells rupturing under the high shear rates found in the counter channel during forward counting, and not having the opportunity to be captured or counted again during the reverse counting phase.

4.4.4 CD4+ T Lymphocyte Count Comparison: Optical vs. Electrical

Fourteen purified leukocyte samples of varying dilution (0.5 to 2 times the physiological leukocyte concentration) were analyzed using a capture chamber conjugated with CD4 antibody. Figure 4.11(a) shows the results of the CD4+ T cell counting experiments and the close correlation ($y = 0.994x$, $R^2 = 0.997$) between the electrical differential method and the optical control experiments.

Figure 4.11(b) illustrates the cumulative forward and reverse counts during an experiment, showing how the absolute number of helper T cells was calculated. This particular experiment was finished within 7 minutes, as the reverse count levels off at this point. The average counting time for 12 experiments was 10±1.8 minutes, which can easily be shortened by using higher flow rates. The two other experiments were not included in the average because their average flow rates differed from the majority, affecting the analysis time.

Figure 4.11(c) shows Bland-Altman comparison analysis between the electrical differential and optical counting methods. A bias of only -9 cells confirms the accuracy of the electrical differential counting method for the entire range of enumerated CD4+ T cells. One reason for the negative bias (larger optical counts than electrical counts) could be that leukocytes traveling in aggregates were counted as one entity during the forward count, were then separated by the high shear forces of the entrance counter, and then were counted individually during reverse counting. This would result in a lower electrical CD4+ T cell count and a negative bias when compared to the optical count.

Figure 4.11(d) shows how the percent error relates to the total number of CD4+ T cells counted. (The percent error here is defined as the absolute difference in optical and electrical counts, normalized by the optical count.) Assuming that 5 μL of sample was flown into the chip, the data can be separated into three important CD4+ T cell concentration regimes for AIDS diagnostics. For less than 1,000 cells captured on the chip (5 μL sample at 200 cells$\cdot\mu L^{-1}$, the clinical definition of AIDS), the average error was 4.5% ($n = 3$). This shows to have high accuracy; for example, a patient with an actual CD4+ T cell concentration of 100 cells$\cdot\mu L^{-1}$ would have a counting

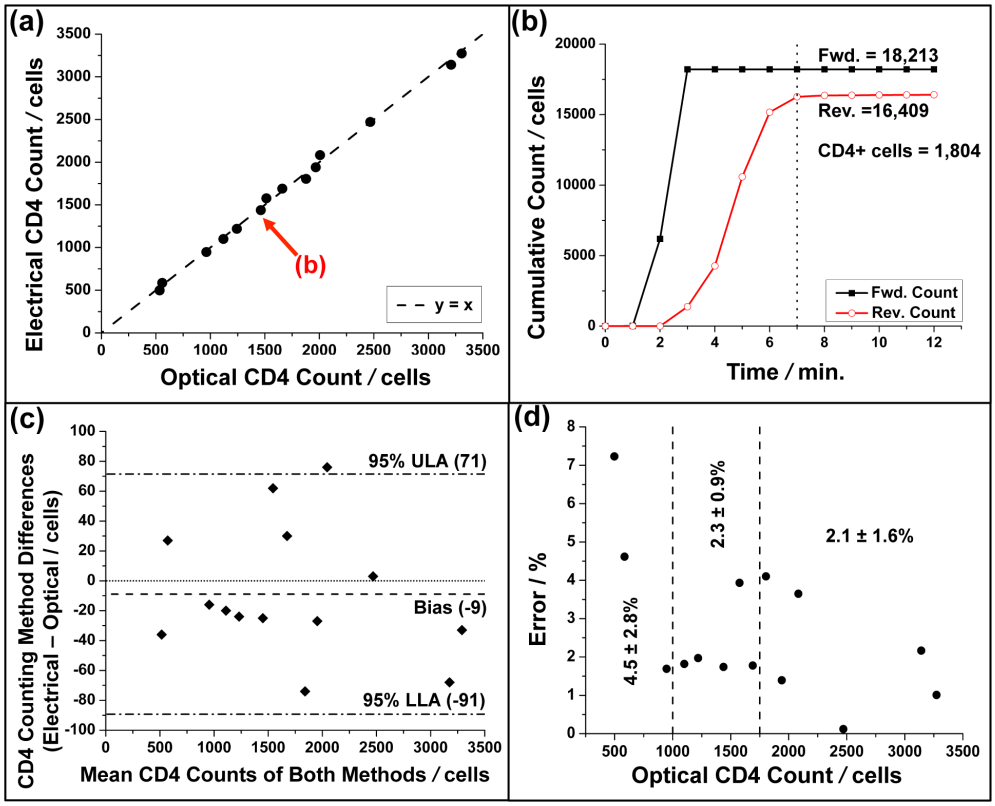

Figure 4.11: Reverse-flow differential counting of CD4+ T lymphocytes. (a) Comparison of electrical differential counting method and the optical controls. A linear fit ($R^2 = 0.997$) is not shown, as it is would be indistinguishable from the y = x correlation standard. (b) Cumulative counts of forward and reverse-flow regimes for the particular experiment highlighted in (a). The absolute number of captured CD4+ T cells was found simply by subtracting the reverse count from the forward count. The dotted line denotes a completed analysis (where reverse counting levels off) duration of approximately 7 minutes. (c) Bland-Altman analysis of the data in (a). The dash-dot lines denote upper and lower levels of agreement (ULA and LLA, respectively). The dashed line shows a bias of 9 cells toward the optical method. (d) Counting error decreases as the total number of captured CD4+ T cells increases. Listed statistics are for three regimes demarcated by dashed lines: 0 to 1,000 captured helper T cells (0 to 200 cells·μL^{-1}, assuming 5 μL of sample flown into chip), n = 3; 1,000 to 1,750 (200 to 350 cells·μL^{-1}), n = 5; and greater than 1,750 (> 350 cells·μL^{-1}), n = 6. From [139] - Reproduced by permission of The Royal Society of Chemistry.

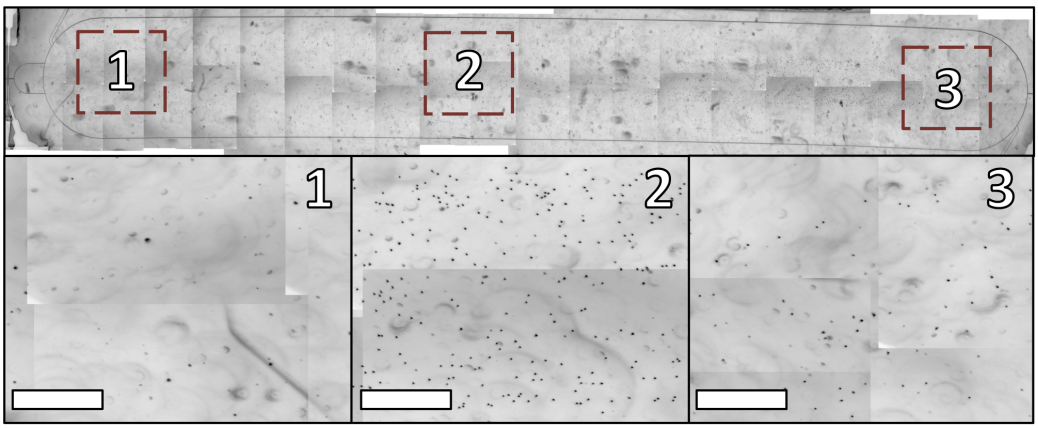

Figure 4.12: Composite phase contrast image of entire 34 mm-long capture chamber after a differential counting experiment. The bottom three panels are magnifications of the regions denoted in the main figure. Error bar lengths are 500 μm, and grayscale intensity was inverted to enhance visualization of captured cells (dark spots). From the supplementary of [139] - Reproduced by permission of The Royal Society of Chemistry.

error of only ± 4.5 cells$\cdot\mu$L^{-1}. The device has also shown to be even more accurate for the regimes surrounding the clinically critical threshold of 350 cells$\cdot\mu$L^{-1} (1,750 cells captured), which has been shown to be an optimal condition to start ART [5].

Figure 4.12 shows a composite phase contrast image of the entire capture region that was used to obtain the optical control count for a particular experiment. The largest density of cells was located near the midpoint of the chamber's length (inset 2), while a smaller density was found near the entrance (inset 1). The cells would have had little time to interact with the antibody layer just upon entering the chip compared to the interaction time from reaching the center of the chip. The low capture density near the exit (inset 3) can be explained by the fact that a smaller concentration of cells leading the entire population reached the exit counter first, causing reversal of the flow before higher concentrations could reach the end of the chip. One cause of these leading cells could be that they were traveling at or near the center of the microbore tubing (or the center of the capture chamber's height), where they would travel at approximately twice the velocity of the other cells, which were traveling at the average flow velocity under laminar flow conditions.

4.4.5 CD4+ Capture Efficiency

Flow cytometry analysis for 8 chips showed that 60.2±18% of CD4+ T cells were immobilized in the capture chamber. A major reason for this low capture efficiency may be that cells entering into the chip later do not have enough time to interact with the antibody before flow reversal. In addition, the low shear stress used during the experiments (0.5 dyn·cm^{-2}) may also cause a loss in capture efficiency. Cheng et al. have shown that shear stresses between 1 and 3 dyn·cm^{-2} will ensure adequate CD4+ T cell capture (∼95%), while efficiency sharply drops off outside of this zone [51]. However, they relied on erythrocytes flowing in the center of the capture chamber to effectively push the leukocytes toward the chamber walls, facilitating more leukocyte-antibody interactions. In our case, erythrocytes must be lysed to accurately enumerate leukocytes, but this removes the leukocyte margination mechanism. Although most leukocytes were able to come into contact with the chamber's floor by sedimentation, other leukocytes traveled near the center of the 50 μm-high channel at higher velocities and away from interactions with its walls. Simply reducing the capture chamber's height would not only increase the shear stress to within the desired range, but also ensures cells would interact with the chamber's walls. In addition, a covalent surface chemistry using linkers could be used to ensure proper CD4 antibody fragment antigen-binding (Fab) region orientation for optimal cell capture.

Additional error may have been introduced simply by the fact that a small sample volume (5 μL) was collected for flow analysis. Some practical issues are cells lost by non-specific adsorption to tubing during collection and cells lost during flow cytometry analysis preparation (fluorescent staining and washing).

4.4.6 CD4+ capture purity

Figure 4.13 depicts the analysis of three areas of a chip's capture region as an example of fluorescence analysis for quantification of captured cell purity. The percentage of captured cells being leukocytes was calculated by dividing the number of DAPI-positive cells by the number of cells found in the bright field image. The percentage of captured cells being CD4+ was calculated by dividing the number of Alexa Fluor® 488-positive (CD4+) cells

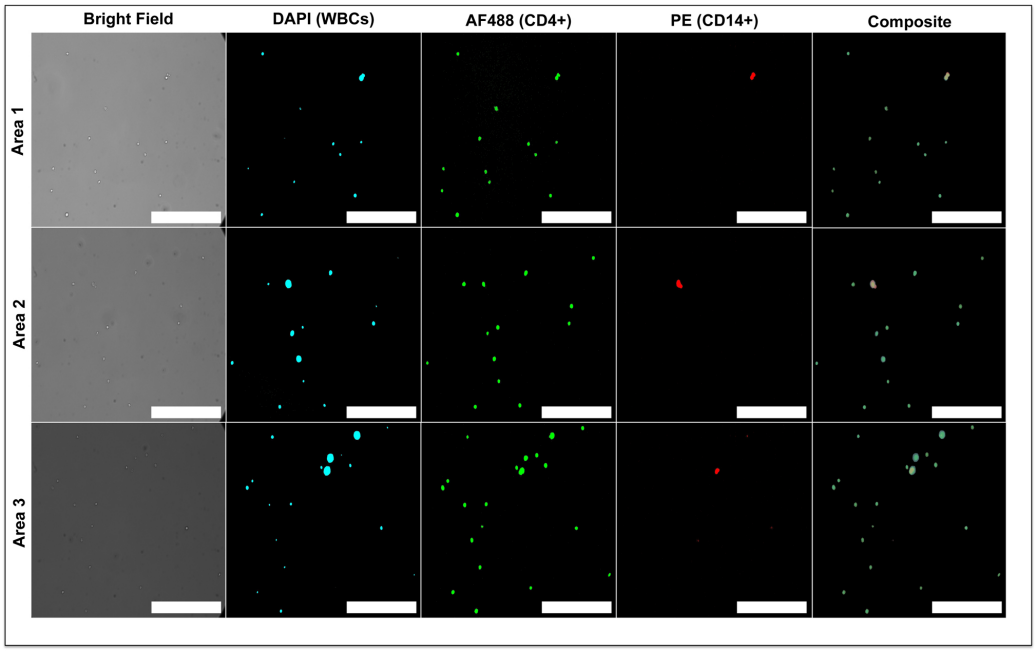

Figure 4.13: Example of selective fluorescence analysis of captured cells shown in bright field images for three different areas of the chip's capture region. ImageJ threshold analysis was used to define cells; false coloring was used to discriminate among the three fluorophores used: DAPI (blue; nucleated cells or white blood cells), Alexa Fluor® 488 (green; CD4+; present on helper T cells or monocytes), and PE (red; CD14+; present on monocytes). Scale bars represent 200 μm. From the supplementary of [139] - Reproduced by permission of The Royal Society of Chemistry.

by the number of DAPI-positive cells. The percentage of captured cells being monocytes was calculated by dividing the number of PE-positive (CD14+) cells by the number of Alexa Fluor® 488-positive cells. ImageJ software was used to determine the grayscale threshold level which defined the presence of a cell. False coloring was used to illustrate the different fluorescent labels used in the experiments.

Three chips were analyzed for CD4+ T cell capture purity after completing electrical differential counting experiments. In all chips, it was found that all captured cells were leukocytes (DAPI+) expressing the CD4 antigen (AF488+), confirming the high specificity of the surface chemistry for CD4+ cells. It was found that 81.7% of captured cells were CD4+ T lymphocytes, with monocytes comprising the remaining portion. According to Cheng et al., monocyte capture increased for shear stresses < 0.7 dyn·cm^{-2}, a regime in which our chip was operating (0.5 dyn·cm^{-2}) [51]. One of the chips had a

CD4+ T cell capture purity of 56.5% because flow was temporarily stopped before reversing flow direction. This effectively decreased shear stress even further, allowing more monocytes to be captured. The other two chips had no such stoppage, and showed an average capture purity of 94.3%, which agrees with our previous work [51]. Although relatively small, the percentage of captured monocytes can still cause a positive bias for patients CD4+ T cell counts below 200 cells$\cdot\mu L^{-1}$. One solution for this problem is to create a monocyte depletion chamber conjugated with CD14 Ab immediately before the entrance to the entrance counter and main capture chamber [53].

4.5 Conclusions

We have demonstrated as a proof of concept that a differential cell counter device using the reverse-flow technique and cell immunoaffinity depletion is a viable method to electrically enumerate CD4+ T lymphocytes from purified leukocyte populations from donor blood samples. Our microfabricated device and detection approach resulted in a short testing time of 10 minutes, had an accuracy (9 cells$\cdot\mu L^{-1}$) that allows for lower detection limits, and correlated closely with an optical standard ($R^2 = 0.997$), demonstrating its capability to analyze patients in all stages of HIV infection. Its microfabricated nature suggests it may be an inexpensive, simple, and portable alternative to current flow cytometric practices that would enhance the penetration of CD4+ T cell tests into resource-poor regions.

Several advancements to the current design are necessary to create a complete PoC AIDS diagnostics device for whole blood samples. An on-chip erythrocyte removal/lysis module is needed to eliminate off-chip sample preparation steps. Also, an on-chip sample metering system is necessary to accurately ensure a known amount of blood is injected into the chip and for comparison to other CD4+ T cell counting methods. Furthermore, an optimized capture chamber design and surface chemistry would provide greater CD4+ T cell capture efficiency.

CHAPTER 5

ELECTRICAL DIFFERENTIAL COUNTER FOR CD4+ T LYMPHOCYTES WITH SAMPLE PREPARATION MODULE

5.1 Introduction

In the previous chapter, it was demonstrated that CD4+ T lymphocytes could be accurately enumerated using a microfabricated sensor that used only electrical interrogation coupled with an antibody-coated capture region. This is significant, as it does not require the bulky, expensive, and fragile optics and fluorescent labeling implemented by other reduced-scale CD4+ T cell analyzers. However, this previous design requires off-chip sample preparation to create a purified population of leukocytes via erythrocyte lysis and centrifugation. These off-chip steps are impractical for resource-poor regions, which may not have laboratory equipment, personnel, or laboratories to perform such steps. This chapter details the methods to develop the necessary on-chip sample preparation module to realize an integrated, stand-alone CD4+ T cell counter that can handle whole blood as an input.

5.2 Principle

Figure 5.1 shows the newest version of the electrical differential counting chip which can handle whole blood samples. This chip builds upon the reverse-flow differential counting principle where white blood cells are counted before (*forward count*) and after the depletion of CD4+ T cells (*reverse count*), with the absolute CD4+ T cell count being the difference between the forward and reverse counts [139]. A multilayer fluidics network is necessary to ensure accurate spatio-temporal control of the injected blood cells and a small chip footprint.

The addition of an erythrocyte lysis module is critical to ensure accurate

counts, as the sheer number of erythrocytes (∼1,000 times average leukocyte concentrations) would require large sample dilutions—increasing analysis time drastically—and would inherently increase the probability of counting error. As an example of the latter point, 1 μL of blood from a patient may have 500 CD4+ T cells, 5,000 leukocytes, and 5 x 10^6 erythrocytes. With no erythrocyte lysis, only ∼0.01% of the counted cells would be captured. This small change could be easily lost in the noise of sources of error, such as the nonspecific adsorption of erythrocytes to the capture chamber. On the other hand, erythrocyte lysis would result in a 10% difference between forward and reverse counts in this example, which we have shown to be detectable [139].

The lysis module selectively ruptures the membranes of the erythrocytes through diffusive mixing of the lysis solution (saponin + formic acid) with the centered blood stream [118, 143]. Figure 5.2(a) shows how the blood sample stream is focused between two lysis streams to enhance the diffusion effects, while the 65 μm-tall serpentine mixing region, Fig. 5.2(b), ensures complete diffusion and enough lysis time to rupture all erythrocytes but keeps leukocytes intact (∼6 s). The 110 μm-tall quenching module supplies a concentrated solution of salts and sodium carbonate to both sides of the mixture to quickly halt lysis and give the saponin from the lysing solution enough time to fully disassociate erythrocyte membranes—creating a debris-free, purified population of leukocytes before electrical analysis at the counting region (Fig. 5.2(c)). The quenching process has been shown to take ∼10 s [143].

The counting region is similar to our previous work and is comprised of a 15 x 15 μm^2 channel with 15 μm-wide platinum electrodes with similar gaps, resulting in a sensing volume (∼17 pL) small enough to ensure cells are counted individually and with little cell passage height variance over the coplanar sensing electrodes [139]. Figure 5.2(d) shows two leukocytes passing through the counter region. The main purpose of the three-electrode system is to determine whether cells are entering or exiting the chip after flow reversal [139]. The new chip lacks the second (exit) counter of the previous design because an external metering system has been added that can accurately deliver a known volume of sample to the chip. Equally important, a large (∼500 μL) holding coil has been added to the chip's exit to ensure no cells are lost before all the sample is metered and flow reversal starts.

The capture region selectively captures CD4+ T cells via CD4 antibodies immobilized on the chamber walls. Each of the 20 mm long, 2 mm wide

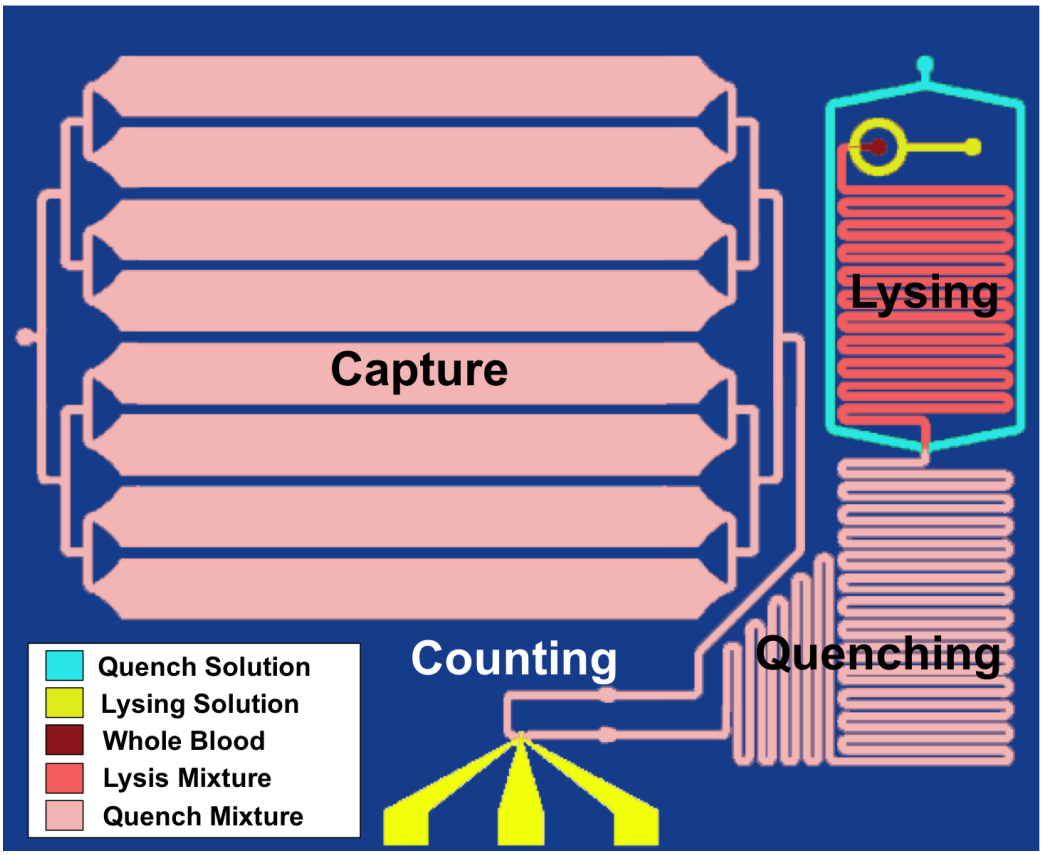

Figure 5.1: Electrical differential counter chip for whole blood samples (3 cm x 4 cm footprint). The lysing region contains all three fluid inlets, denoted by color described in the inset legend. The capture region includes the sole chip outlet, which is connected to a 500 μL exit holding coil to prevent the loss of leukocytes before flow direction reversal. The lysis mixture contains whole blood and the lysis buffer, while the quench mixture contains whole blood, lysis buffer, and quenching buffer. The lighter shades of red illustrate the progressive dilution of the blood sample after being processed through each module.

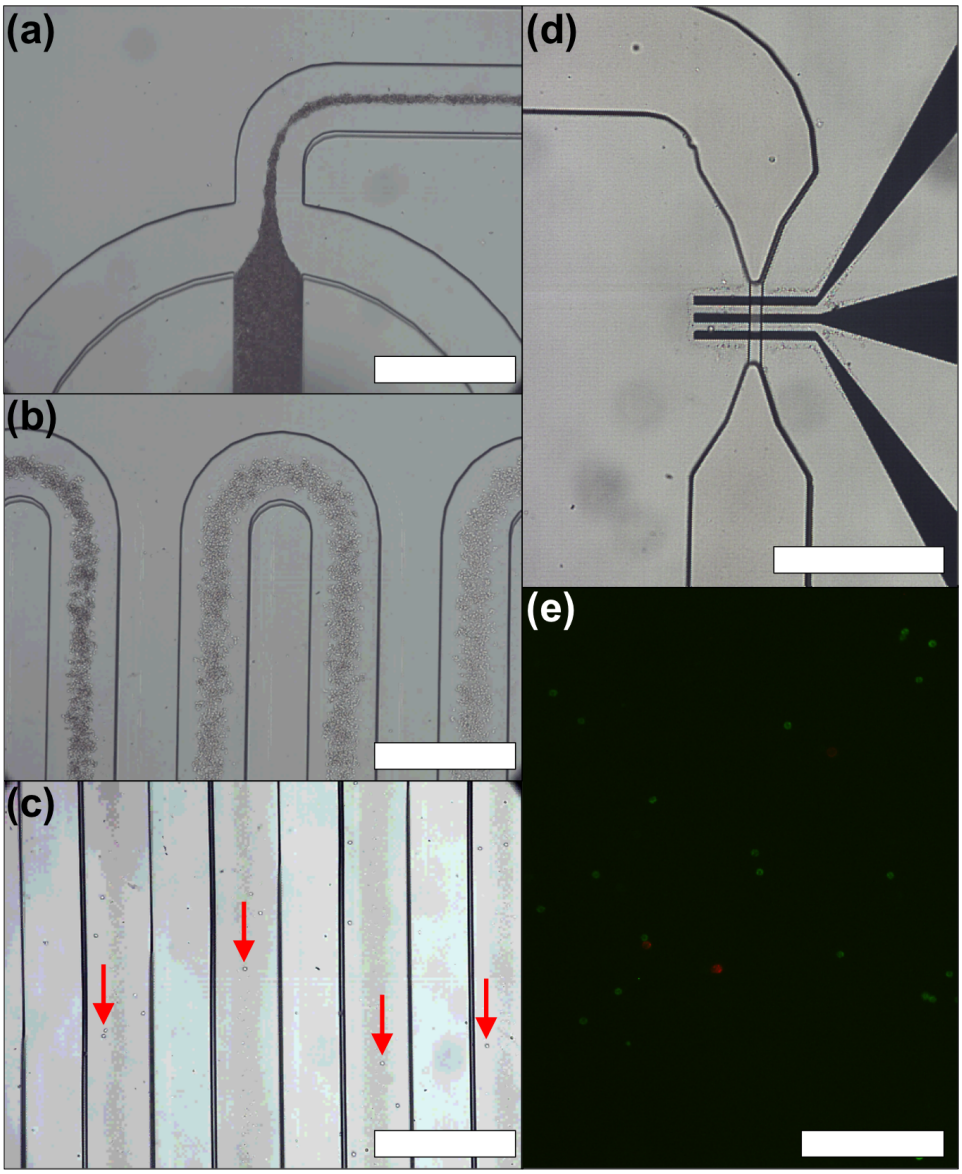

Figure 5.2: Micrographs of the various regions shown in Fig. 5.1. (a) Focusing of blood sample by lysis buffer sheaths to decrease diffusion time necessary to lyse the erythrocytes. (b) Serpentine mixing channels in the lysing region. As the blood sample flows from left to right, the erythrocytes' membranes progressively rupture until they release their hemaglobin, resulting in transparent "ghosts". (c) Mixing channels in the quenching region, showing only leukocytes (some highlighted with arrows). (d) Two leukocytes passing through the counting region. (e) Fluorescent micrograph of CD4+ T lymphocytes (green) and monocytes (red) that were captured in one of the chambers in the capture region. False coloring was used to simulate actual fluorescence color. Scale bars: (a) – (c), 400 μm; (d), 300 μm; (e), 150 μm.

capture chambers are of equal height, which depends on the desired capture chamber shear stress and the total flow rate of the three chip inlets (70 – 208 μm). Because of the increase of total flow rate from the on-chip lysis and quenching modules ($\sim$20x sample flow rate), a binary network of channels is used to equally divide the sample flow into eight identical capture chambers to ensure channel shear stress is low enough to allow enough interactions between the cells and the immobilized antibodies on the chamber walls. A single 16 mm-wide capture would not have given desired results, as the very low height-to-width ratio would cause the chamber to collapse during fabrication. It would also balloon up when pressurized during experiments, creating a capture channel height much more than the desired height (this was even noticed sometimes with the 4 mm-wide capture chamber in the previous chapter). Finally, it was observed that even with a 4 mm capture chamber from last chapter's experiments, cells would generally flow in the center of the channel, missing a majority of possible interactions with immobilized antibodies not in the center of the channel's width. This would only be perpetuated with a wider capture chamber. The 2 mm width has proven to solve or lessen the aforementioned problems. Figure 5.2(e) shows fluorescently labeled CD4+ T lymphocytes (green) and monocytes (red) immobilized in one of the capture chambers.

5.3 Materials and Methods

5.3.1 On-Chip Sample Preparation

Erythrocytes were first lysed for durations between 2 and 10 s upon entering the chip by using a 0.12% (v/v) formic acid and 0.05% (w/v) saponin in DI solution. Lysis was quickly quenched using a 0.6% (w/v) sodium carbonate and 3% (w/v) sodium chloride in DI solution or a solution of concentrated PBS with 0.6% (w/v) sodium carbonate. The blood sample, lysing, and quenching solutions are each flown at particular rates to ensure similar mixture ratios as noted in the literature [143]. The ratio between the blood sample and lysis solution flow rates was always locked to 1:12, respectively. The ratio between the blood sample and 3% (w/v) sodium chloride quenching solution was set to 1:5.3, while it was 1:6.3 for the concentrated PBS

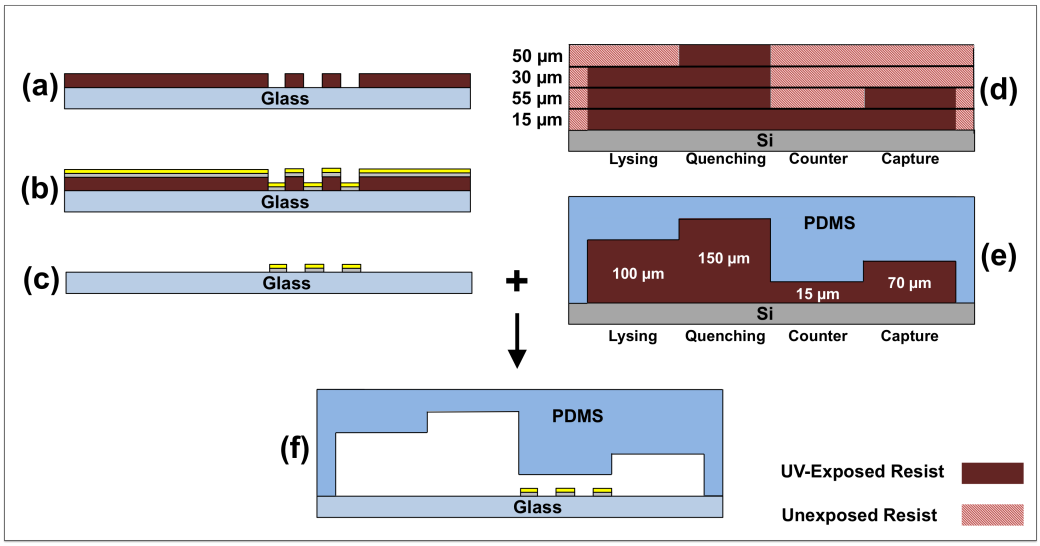

Figure 5.3: Microfabrication processes for creating the electrodes (a–c) and fluidics (d–e) layers. Both layers were exposed to O_2 plasma before aligning and permanently bonding them (f). Different channel heights were used to ensure proper cell residence time (lysing and quenching), counting accuracy (counter), and capture chamber shear stress (capture).

quenching solution.

5.3.2 Counter Fabrication

Figure 5.3 illustrates the fabrication methods used to create the aforementioned differential counter chip, which is comprised of an electrodes layer and a multi-level fluidics layer.

Platinum electrodes were created by standard lift-off processes, as previously described [139]. Briefly, a negative of the electrodes pattern (15 μm widths and gaps) was patterned on a 4" glass (Pyrex 7740) wafer using a double layer liftoff recipe using LOR2A lift off (Microchem Corp. Newton, MA) and Microposit S-1805 (Rohm and Haas Electronic Materials, Marlborough, MA) resists. An EV420 mask aligner (Electronic Visions, Inc., Rockledge, FL) was used to align and expose the wafer, and the resist was developed with Microposit CD-26 developer (Fig. 5.3(a)). An SEC-6000 evaporator (CHA Industries, Fremont, CA) was used to first deposit a 25 nm Ti adhesion layer, followed by a 75 nm Pt conduction layer (Fig. 5.3(b)). Undesired metal was subsequently lifted off using Microchem Remover PG to create the

electrode geometry (Fig. 5.3(c)). Individual chips were diced using a Disco DAD-6TM dicing saw (Tokyo, Japan).

The multi-level fluidics layer was created using standard rapid microfluidic prototyping using Microchem SU-8 negative photoresists and Poly(dimethylsiloxzane) (PDMS). A negative master was constructed on a 4" Si wafer using four successive iterations of the standard SU-8 recipe, with all soft bake and post-exposure bake durations and temperatures being similar to those suggested in the SU-8 product sheets. SU-8 was spun to a height of 15 μm and exposed using the EV420 mask aligner to define the counting and filter regions and provide a base for the other regions. A 55 μm layer was then spun on and exposed to define the 70 μm-tall capture region. 30 μm of SU-8 50 was deposited to define the 100 μm lysis region, followed by a 50 μm layer to create the 150 μm quenching region (Fig. 5.3(d)). Development in SU-8 developer was deferred until all four layers were created. After development and rinsing the mold with IPA, a 1:10 curing agent to base mixture of PDMS was poured over it and cured for at least 15 minutues at 150° C to create the fluidic channels (Fig. 5.3(e)). The fluidic inlets and outlet were cored out of the PDMS mold using a custom hole punch.

Devices were assembled by aligning and permanently bonding the electrodes-glass and PDMS layers after exposing both to O_2 plasma (Fig. 5.3(f)). Microbore tubing was inserted into the inlets and outlet to connect to the fluidic control system, described below. Figure 5.4 shows a finished chip, which has a 3 cm x 4 cm footprint.

5.3.3 Experimental Setup

Figure 5.5 illustrates the setup used to evaluate the differential counter device. An Eksigent Nanoflow LC pump (Dublin, CA) is used to infuse the lysing, quenching, and PBS carrier and washing solutions into the chip with accurate and consistent flow rates. A Rheodyne MHP7980-500-1 valve (Rohnert Park, CA) is used to load a blood sample into a 10 μL holding coil (via syringe) and then direct PBS through the coil to inject the blood sample into the chip. Air bubbles are injected into the holding coil immediately before and after the blood sample to ensure no diffusion into and dilution from the adjoining buffer solutions. Inside the chip, the erythrocytes are

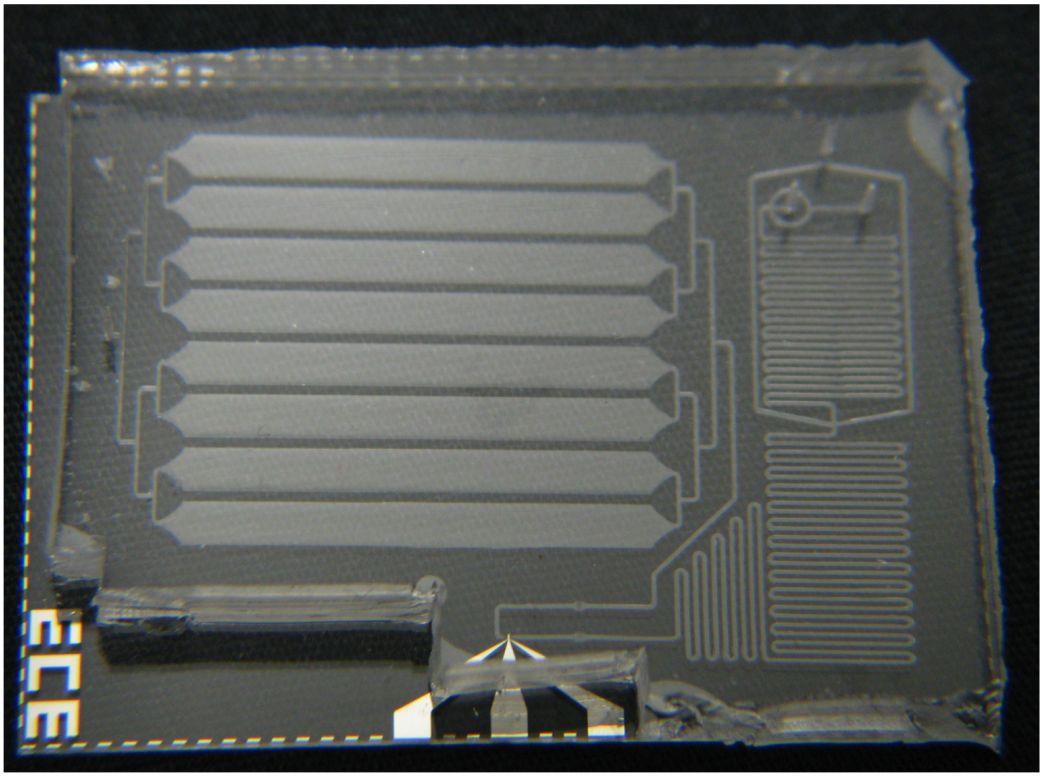

Figure 5.4: Completed microfluidic chip after PDMS/glass bonding.

lysed, leukocytes are electrically counted, and CD4+ T cells are captured in the capture region. These processes continue until 10 μL of sample has been injected into the chip, providing the *forward count*. A valve with a 500 μL holding coil contains any uncaptured leukocytes that have exited the chip to ensure no loss of cells during forward flow. Once the 10 μL sample is injected into the chip, both valves are switched to reverse the flow direction and wash all cells out of the 500 μL holding coil and the chip's capture and counting regions to obtain the *reverse count*. Figure 5.6 graphically summarizes the processes performed in the microfluidic chip to obtain an electrical differential count. Experiment durations range from 12 to 35 minutes, depending on the total flow rate in the chip, which in turn depends on the capture chamber height and the desired capture chamber shear stress.

A Zurich Instruments (Zurich, Switzerland) HF2LI lock-in amplifier was used to simultaneously inject 303 kHz and 1.7 MHz AC signals (both at 5 V (rms) amplitude) into the chip's center counting electrode. Relative impedance was obtained by creating a Wheatstone bridge circuit with 10 kΩ resistors [139]. The voltage difference between the two Wheatstone branches

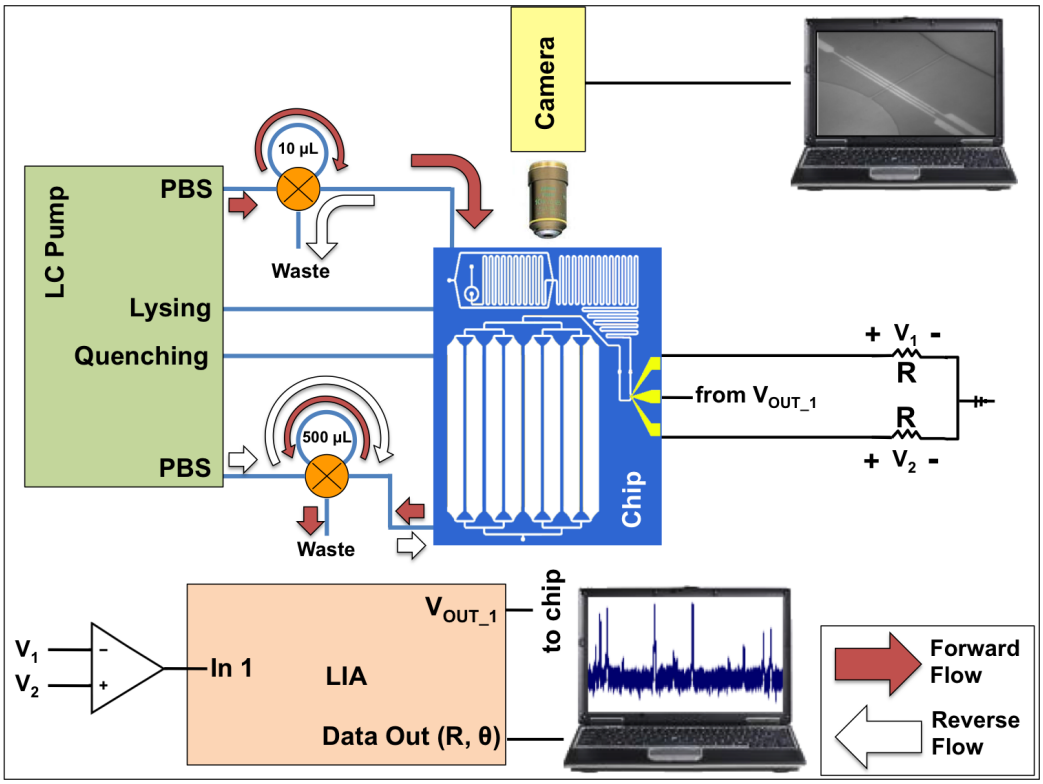

Figure 5.5: Experimental setup

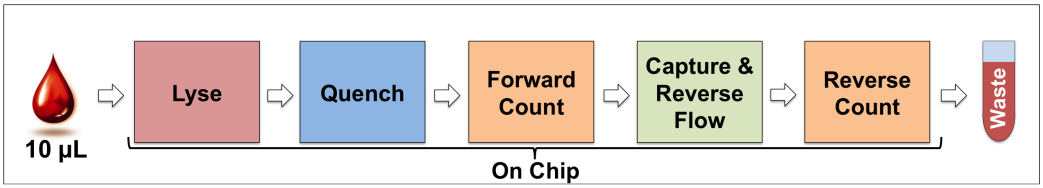

Figure 5.6: Flow graph of processes performed in the differential counter chip. The chip waste is used for subsequent characterization of the chip's capture performance. Experiment durations may range from 12 to 35 minutes, depending on the total flow rate of the chip, which depends on the capture chamber height and the desired shear stress.

was found using a differential preamplifier (Zurich Instruments) and input into the HF2LI, which provided the impedance magnitude (R) and phase (θ) that was recorded at a 500 kHz sampling rate in LabVIEW on a computer with a PCI-6351 DAQ card (National Instruments, Austin, TX). A customized Matlab program was used to analyze pulses at a high throughput, providing differential counting data in the form of various scatterplot relationships. For example, the low frequency impedance (at 303 kHz) can be plotted against the electrical opacity, which is the ratio of high frequency (at 1.7 MHz) to low frequency impedances [102].

The following is the reasoning behind the chosen interrogation frequencies. The 303 kHz (low frequency) signal was used to differentiate among leukocytes based on cell size. At this frequency, cells act as non-conducting spheres that completely block the electrical current in the volume of conductive fluid they displace. This creates impedance pulses that are proportional to a cell's volume [95,132]. As a result, the lymphocytes (7 – 8 μm diameter) can be distinguished from the larger granulocytes and monocytes ($\geq$ 10 μm diameter). The 1.7 MHz interrogation frequency (high frequency) has been shown to further differentiate among the leukocytes and between cells and debris [117, 118, 122]. At this frequency, the change in impedance from cell passage is less about cell size and more about the cell membrane capacitance, which is shown in Fig. 2.9(b). Cells with different membrane surface morphologies (*e.g.*, roughness, folds, wrinkles, blebs, etc.) will have different membrane surface areas, resulting in different membrane capacitances. For example, monocytes have extensive ruffling and pronounced folds in their membranes, which would increase their surface area, leading at an increase in membrane capacitance [144]. This could distinguish them from neutrophils, which may have less prominent ruffles and folds. Equation 5.1 shows how the impedance from a capacitor Z_{cap} is inversely proportional to capacitance (C) at a particular frequency (ω), and how a larger capacitance would result in a smaller total impedance.

$$Z_{cap} = \frac{1}{j\omega C} \tag{5.1}$$

Gawad *et al.* extend this concept to calculating cell impedance using the equivalent circuit model for a cell in Fig. 2.9(a) to simulate changes in a

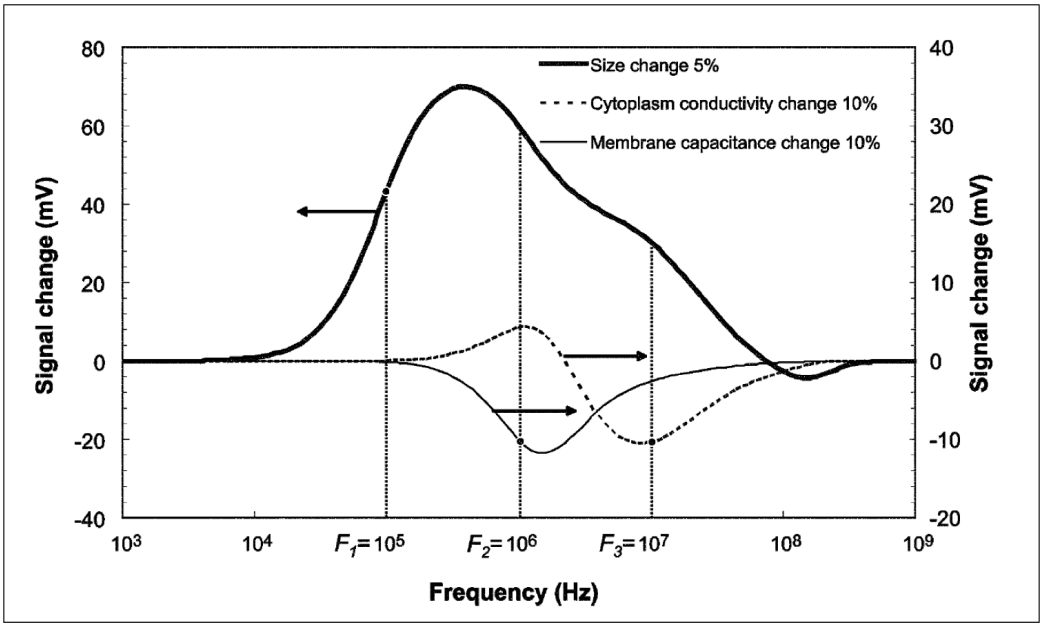

Figure 5.7: SPICE simulation of the impedance of a cell, showing how modifying cell characteristics changes the total impedance of the cell. Of particular interest is the 10% increase in cell membrane capacitance, which causes a decrease of impedance, which is maximum around 1.7 MHz. From [145] - Reproduced by permission of The Royal Society of Chemistry.

cell's impedance after increasing its membrane capacitance [145]. According to their results in Fig. 5.7, this change creates a decrease in cell impedance which is maximum around 1.7 MHz. This may be why Holmes *et al.* were able to differentiate between neutrophils and monocytes at a frequency of 1.7 MHz, as they show that the opacity of the monocytes is less than the neutrophils (Fig. 2.12(a)) [117].

A Nikon Eclipse E600 FN microscope (Nikon Instruments, Incl. Melville, NY) coupled with a Phantom v310 high speed camera (Vision Research, Wayne, NJ) was used to verify the chip's proper operation, including erythrocyte lysis, debris filtering, leukocyte counting, and CD4+ T cell capture.

5.3.4 Blood Sample Acquisition

Blood samples were obtained from volunteers using an informed consent process approved by the UIUC Institutional Review Board. Blood was collected via venipuncture in EDTA-coated BD Vacutainers® (BD Biosciences, Franklin Lakes, NJ), and kept on sample rotisserie at room temperature until

needed for experiments. The blood samples were used within 24 hours for all chip experiments and external controls.

5.3.5 Passivated Capture Chamber Analysis

With the addition of the lysing, quenching, and filtering modules and a modified capture chamber geometry, it was important to re-evaluate the reverse-flow differential counting method. Possible error could come from the delayed loss of cells from the shock of the rapid lysis process or from the relatively long cell residence time in the blood/lysis/quenching mixture. This mixture contains a much lower blood protein concentration (∼1:20 dilution) than found in vivo, which may adversely affect the leukocytes' vitality.

Differential counting experiments were performed with capture chambers passivated from all cellular interactions to find the inherent counting error of the system via comparison to the ideal differential count of zero (equal forward and reverse counts) [139]. Capture chambers were passivated for at least 2 hours using a 1% BSA in PBS (pH 4.3) blocking solution. A pH of 4.3 was chosen to facilitate optimal BSA adsorption to the glass surface via electrostatic interactions between the positively-charged glass (isoelectric point of 1.5 to 3.5) and negatively-charged BSA (isoelectric point of 4.7). BSA more readily (30 - 60 times more than glass) adsorbs to the PDMS surfaces for a wide pH range with its smaller surface charge capacity and high hydrophobicity [146].

A 1% BSA in PBS (pH 7.4) solution was used to wash away the blocking solution immediately before performing the reverse electrical differential counting protocol with whole blood samples, which was described earlier in this section. Percent error was determined by finding the difference between the forward and reverse counts, and normalizing the result by the forward count [139].

5.3.6 Erythrocyte Lysis and Quenching Time Optimization

Ledis *et al.* developed the initial protocol for rapid, debris-free erythrocyte lysis using a 0.12% (v/v) formic acid and 0.05% (w/v) saponin in DI solution, and noted that lysis times should not be longer than 10 s, but preferably

6 s or less [143]. Lysis times longer than 10 s would adversely affect the vitality of the leukocytes. They also noted that the lysis process needed to be quenched for at least 10 s to ensure all erythrocytes and their membranes were completely disassociated by the saponin detergent. Van Berkel *et al.* were the first to implement this lysing and quenching technique in a microfluidic environment, which gave them more precise control of the lysis time, which was set to 6 s [118]. They did not mention the quenching time that they used.

Experiments were performed to observe the efficacy of erythrocyte lysis and leukocyte viability for a range of exposure times in the aforementioned lysis solution in a microfluidic environment. 10 μL whole blood samples were injected into the chip, with the blood sample and lysis solution flow rates adjusted to ensure proper flow ratio (1:12) and exposure time in lysis regions of known volume. The lysis process was rapidly neutralized by the quenching solution for durations that would ensure the erythrocyte ghosts were completely disassociated by the saponin detergent before reaching the counting region, which electrically analyzed the purified leukocytes using the aforementioned dual frequency interrogation method. Total leukocyte, lymphocyte, granulocyte, and monocyte concentrations and their respective ratios to each other were compared with controls found using a Sysmex XE-5000 hematology analyzer at the Carle Foundation Hospital Laboratory in Urbana, IL.

Experiments were also performed to find the minimum quench duration to create a debris-free leukocyte solution. Quenching time was varied by adjusting the volume of microfluidic tubing between the output of the quenching region and the input of the counter region. The blood, lysing solution, and quenching solution flow rates and ratios were kept constant. The quenched solution was interrogated with the dual frequency method at the counter region, and the resultant impedance data were analyzed to see whether erythrocytes were successfully lysed (*i.e.*, no interference from unlysed erythrocytes in determining accurate leukocyte counts) for a specific quenching duration.

5.3.7 Capture Chamber Modification for CD4+ T Lymphocyte Capture

Selective capture of CD4+ T lymphocytes from leukocytes was attained by coating the capture chamber region via simple adsorption with CD4 antibody before electrical differential experiments. Specifically, purified mouse antibody to human CD4 (clone 13B8.2; IM0398, Beckman Coulter, Inc., Brea, CA) was diluted 1:20 in pH 7.4 PBS and then injected into the capture region chambers. The solution was then incubated for 30 minutes before a second infusion and subsequent incubation period of at least 30 minutes. The chips were either used immediately after the final incubation period, or stored in a 4 °C refrigerator for experiments that would be performed on the same day as antibody coating. The antibody solution was washed out with pH 7.4 PBS immediately before counting experiments.

5.3.8 CD4+ T Lymphocyte Count Comparison

It is imperative to compare the differential counter chip's CD4+ T cell counts to the "gold" standard of flow cytometry to see whether the chip would be a viable alternative in resource-poor regions. 10 μL whole blood samples were evaluated using the electrical differential counting technique with on-chip erythrocyte lysis and quenching. Control counts were found using a Beckman Coulter FC-500 flow cytometer at the Carle Foundation Hospital Laboratory in Urbana, IL.

5.3.9 CD4+ T lymphocyte Capture Efficiency Analysis

Capture efficiency analysis was used to evaluate the chip's ability to capture CD4+ T lymphocytes at various capture chamber shear stresses. This is necessary to understand possible errors between the electrical differential counts and the various control counts, as poor capture efficiencies would result in chip counts that are much lower than those from control counts. For example, a capture efficiency of 25% would result in electrical counts that are four times less than the control counts, assuming capture purity is 100%.

Figure 5.8 illustrates the capture efficiency analysis protocol. Two populations were analyzed for the percent of CD4+ T cells (out of total lymphocytes) from the same blood source: (1) 10 μL whole blood samples that went through on-chip lysis and quenching, but were collected in a tube immediately after the quenching process and (2) 10 μL whole blood samples that went through the entire reverse differential counting process with capture chambers coated with anti-CD4 antibody (also including) on-chip lysis and quenching. Both populations were collected in tubes already containing a 1% BSA in PBS (pH 7.4) solution and immediately centrifuged (200 x g, 5 minutes) and resuspended in 200 μL of the BSA solution. This dilution of chip waste in the BSA solution was necessary, as it was found to increase leukocyte vitality. Omitting this dilution step resulted in total loss of all leukocytes. Both samples were labeled with a cocktail of Alexa Fluor® 488-conjugated mouse antibody to human CD4 (MHCD0420, Invitrogen, Carlsbad, CA), phycoerythrin-Cy7 (PE-Cy7™)-conjugated mouse antibody to human CD45 (25-0459-42, eBioscience, San Diego, CA) and peridinin chlorophyll protein-cyanine 5.5 (PerCP-Cy5.5™)-conjugated mouse antibody to human CD3 (45-0037-42, eBioscience) using the manufacturer's suggested protocols to fluorescently isolate the CD4+ T lymphocytes (CD45+CD3+CD4+). The CD45 label was used to enhance the isolation of the lymphocytes from the other leukocytes, based on the lymphocytes' unique side scatter and CD45 receptor density characteristics. After labeling for 30 minutes, 1% BSA in PBS (pH 7.4) was added to each sample before washing (200 x g, 5 minutes) and resuspending the cells in the BSA solution before flow analysis using a Guava EasyCyte Plus flow cytometer (Guava Technologies, Inc., Hayward, CA). The times listed in Fig. 5.8 are to give an idea of the time the leukocytes have been outside their optimal environment in whole blood.

Capture efficiency was calculated using the equation

$$\eta = \frac{\xi_{pop1} - \xi_{pop2}}{\xi_{pop1}} \tag{5.2}$$

where ξ_{pop1} and ξ_{pop2} are the fractions of total lymphocytes that are CD4+ T lymphocytes measured from the aforementioned populations (1) and (2), respectively. These populations can be explicitly described by the equation

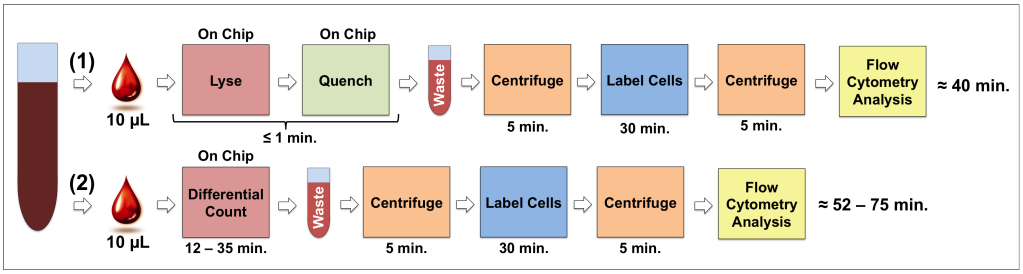

Figure 5.8: Process flow graph for the capture efficiency analysis protocol. Times listed are to give an idea on the time the leukocytes have been outside their optimal environment in whole blood.

$$\xi_{pop} = \frac{X_{CD4Tcell}}{X_{CD4Tcell} + X_{other}} \tag{5.3}$$

where $X_{CD4Tcell}$ is the sum of all CD4+ T lymphocyte events and X_{other} is the sum of all other lymphocyte events.

Population (1) in Fig. 5.8 could have been obtained from flow cytometry at Carle Foundation Hospital Laboratory; however, we wanted both populations (1) and (2) to share as many steps as possible for the most accurate comparison. For example, the Carle reference laboratory would have first labeled the CD4+ T cells with fluorescent antibodies and then lysed the erythrocytes off-chip (using different lysing chemicals than described in this chapter) before flow cytometry analysis.

5.3.10 CD4+ T lymphocyte Capture Purity Analysis

Capture purity analysis was used to evaluate the chip's sensitivity in capturing CD4+ T cells—where a true positive event would be a captured CD4+ T cell and a false negative event would be the capture of any other cell. This capture purity is another important factor in the chip's counting accuracy when compared to control counts. For example, a capture purity of 50% would result in electrical cell counts that are twice those found using the control method, assuming capture efficiency is 100%.

Figure 5.9 illustrates the capture purity analysis protocol. After CD4+ T cell capture experiments were completed, captured cells were labeled in a 1% BSA in PBS (pH 7.4) solution containing Alexa Fluor® 488-conjugated

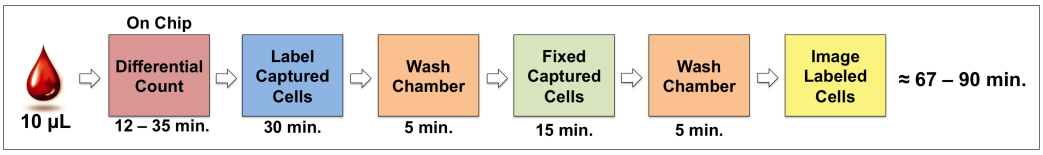

Figure 5.9: Process flow graph for the capture purity analysis protocol. Durations are given to give an idea on how long the leukocytes have been outside their ideal environment in whole blood before analysis. Since the fixing step preserves cell morphology, the actual crucial duration should be between 47 and 70 minutes.

mouse antibody to human CD4 (MHCD0420, Invitrogen), allophycocyanin (APC)-conjugated mouse antibody to human CD14 (MHCD1405, Invitrogen), and 4',6-diamidino-2-phenylindole (DAPI, D21490, Invitrogen). The labeling solution consisted of antibody concentrations that were 1:30 of their respective stock solutions and a 1 μM DAPI concentration. The labeling solution was incubated in the capture chambers for at least 30 minutes before being washed out with fresh 1% BSA in PBS (pH 7.4) solution. Cells were then fixed with a 1% paraformaldehyde (PFA) in PBS (pH 7.4) solution for 15 minutes before being washed with fresh 1% BSA in PBS (pH 7.4). Cells were fluorescently imaged using an Olympus IX81 inverted microscope (Tokyo, Japan) with total magnification of 200x with the appropriate filter sets. Micrographs along the entire length of several of the eight capture chambers were taken to represent the entire captured population. ImageJ software was used to obtain the percentage of CD4+ T cells (DAPI+CD4+CD14-), monocytes (DAPI+CD4+CD14+), and other leukocytes (DAPI+CD4-CD14-) out of total captured cells. Figure 5.9 lists the estimated duration of the capture purity analysis protocol to give an idea of how long the leukocytes have been out of their optimal environment in whole blood before imaging. However, the duration up to fixation is the most crucial, as the fixing step preserves cell morphology. A more accurate assumption would therefore be 47 – 70 minutes.

5.4 Experimental Results and Discussion

5.4.1 Passivated Capture Chamber Analysis

Whole blood samples were analyzed using the reverse differential counting method with a passivated capture chamber. Sample volumes from 0.5 μL to 10 μL were used to vary the total number of leukocytes that passed through the chip. Lysing and quenching were performed on-chip using lysing (0.12% (v/v) formic acid and 0.05% saponin in DI) and quenching (0.6% (w/v) sodium carbonate and 3% (w/v) sodium chloride in DI) buffers that have been previously shown to work in the microfludic environment [118]. Input flow rates were adjusted to ensure ∼6 s lysis times.

Figure 5.10 illustrates the high error found between the forward and reverse counts (average absolute error: $\bar{x} = 36.8\%$, n = 8)[1]. The majority of the points lie well above the x axis, showing many cells were lost between forward and reverse counting. Capture chambers were inspected to ensure minimal non-specific binding of leukocytes occurred. One possible reason for this large error is the lysing/quenching mixture does not create an amenable environment for leukocyte vitality for the minimum of 10 minute residence time, resulting in cell death/lysis before being counted again during reverse flow direction. This was supported by the fact that the lysis/quenching solution mixture had a pH of 6.7 and an osmolarity of ∼400 mOsm, which are far from the ideal in keeping the leukocytes alive for extended periods (in vivo conditions are a pH of 7.4 and osmolarity of 300 to 330 mOsm).

Experiments were designed to confirm whether the counting error was from a quenching solution, which did not fully neutralize the lysis process and provide the cells with an amiable osmotic environment. Erythrocytes were lysed off-chip using the same lysis and quenching solutions as before; however, the leukocyte pellet was washed with and resuspended in a 1% BSA solution in PBS (pH 7.4) before being injected into the chip (bypassing the lysis and quenching modules). Fig. 5.11 shows how the error drastically drops ($\bar{x} = 4.2\%$, n = 9), showing the important role the quenching solution has in ensuring leukocyte vitality for the entire cell residence time in the counter chip.

A new quenching solution was formulated to provide an optimal environ-

[1] $\bar{x}$ and s represent the sample mean and sample standard deviation, respectively.

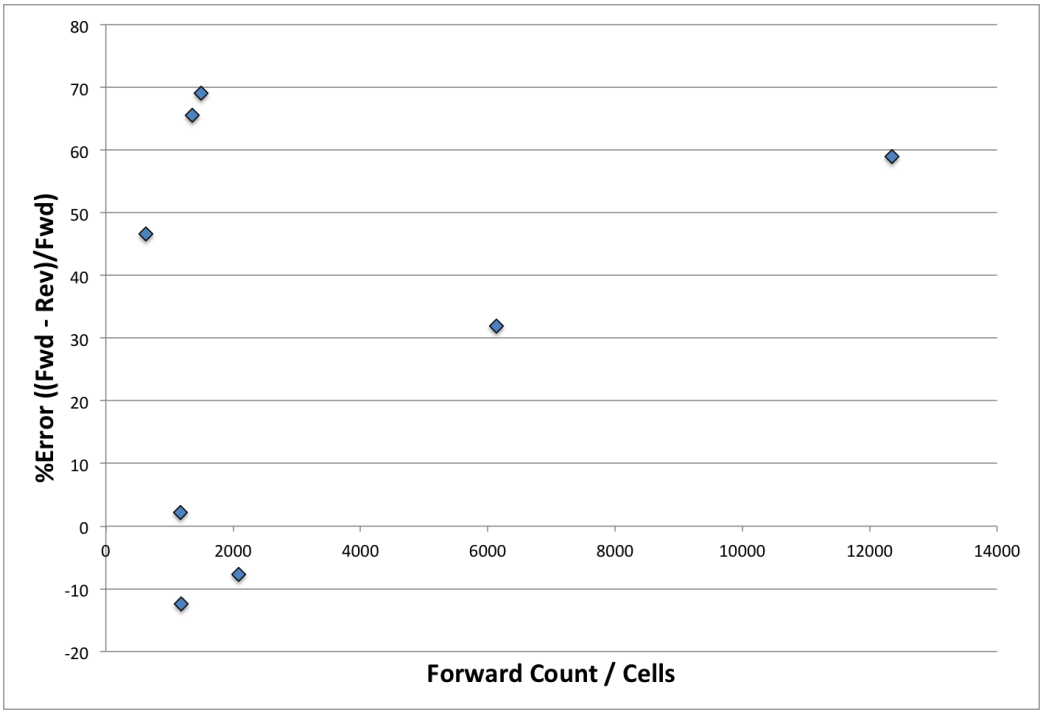

Figure 5.10: Percent error for electrical differential counts with passivated capture chambers using 0.12% (v/v) formic acid and 0.05% saponin in DI lysis and 0.6% (w/v) sodium carbonate and 3% (w/v) sodium chloride in DI quenching solutions. The sample mean and standard deviation were $\bar{x} = 36.8\%$ and $s = 27.0\%$, respectively, and were calculated by taking the absolute of each percent error beforehand (n = 8).

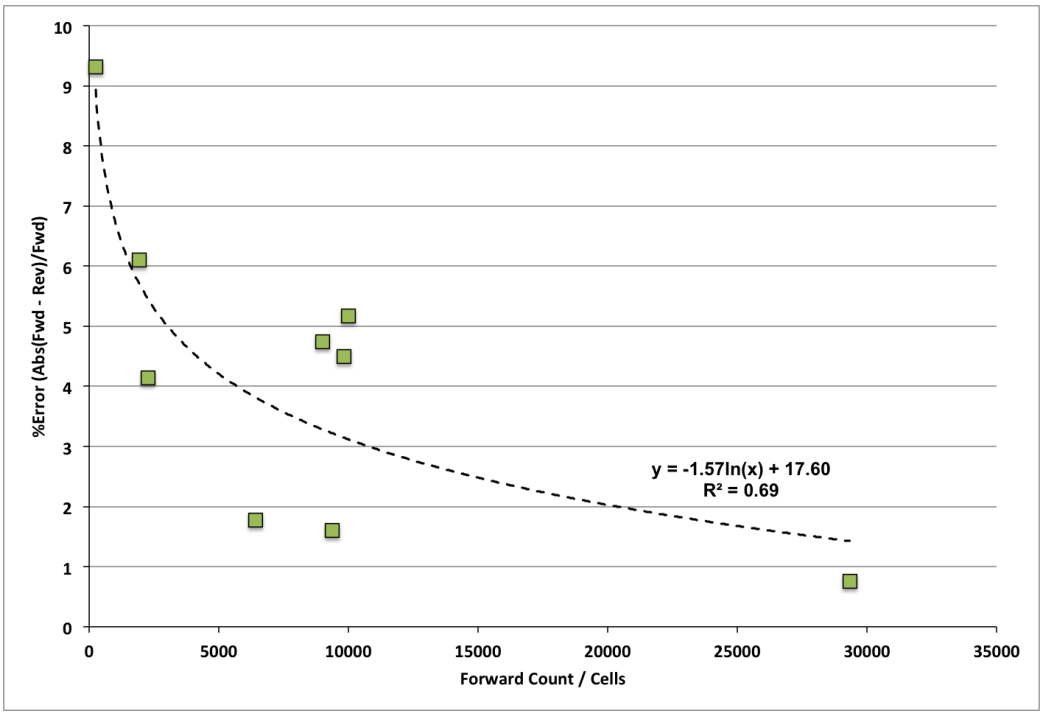

Figure 5.11: Percent error for electrical differential counts with passivated capture chambers using off-chip lysis and resuspension in 1% BSA PBS (pH 7.4) solution. The sample mean and standard deviation were $\bar{x} = 4.2\%$ and $s = 2.6\%$, respectively (n = 9). Outliers were removed with a 99.99% confidence, assuming a T distribution. Logarithmic data fitting (dashed line) was used as the most accurate depiction of %error over a range of forward counts. ($R^2 = 0.69$).

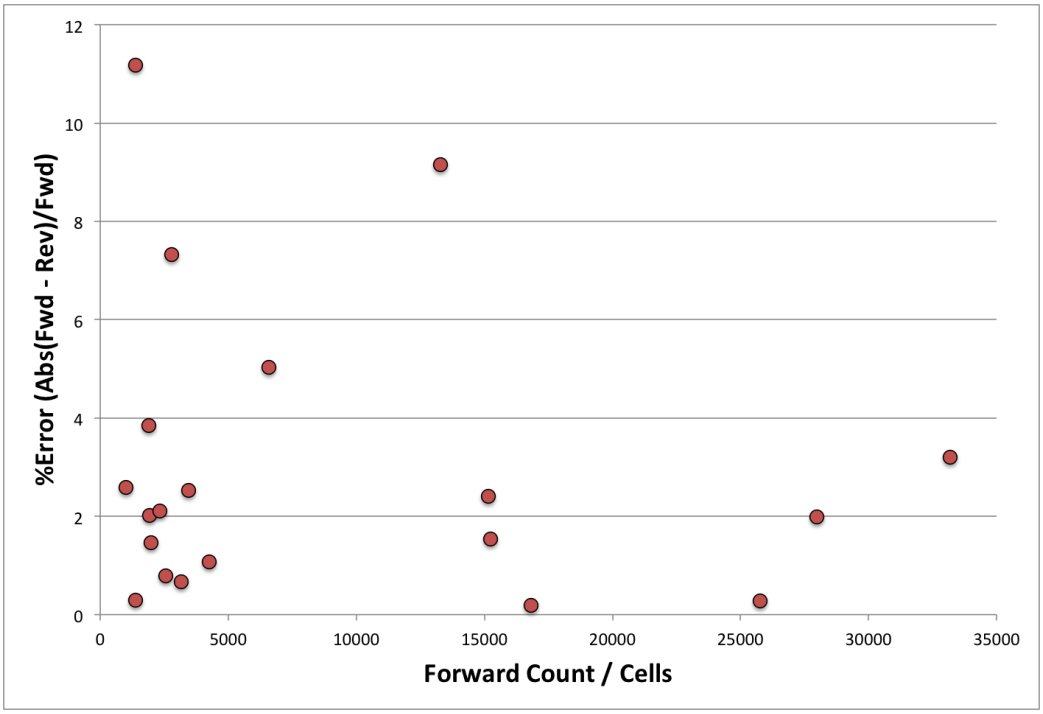

Figure 5.12: Percent error for electrical differential counts with passivated capture chambers using 0.12% (v/v) formic acid and 0.05% saponin in DI lysis and 0.6% (w/v) sodium carbonate in 2.1x PBS quenching solutions. The sample mean and standard deviation were $\bar{x} = 3.0\%$ and $s = 3.0\%$, respectively (n = 20).

ment for the leukocytes after on-chip lysis and quenching. The solution was comprised of concentrated PBS (∼2.1x) and sodium carbonate (∼0.6% (w/v)), which resulted in a pH of 7.4 and an osmolarity of 324 mOsm after mixing with lysing solution and blood—with the ratios of 1 part blood, 12 parts lysing solution, and 6.3 parts quenching solution. The phosphate buffer in the PBS would ensure that the pH would be stable for storage and during experiments, which may not be true for the previous quenching solution that lacked buffer capacity.

Reverse differential counting experiments with passivated capture chambers were performed with the new quenching solution, resulting in a much lower counting error ($\bar{x} = 3.0\%$, n = 20) (Fig. 5.12). Figure 5.13 shows how this error is comparable to using the off-chip lysis methods used in the previous chapter and this chapter, which suggests that the electrical differential counting chip with integrated on-chip lysis and quenching modules is a plausible device to obtain CD4+ T cell counts.

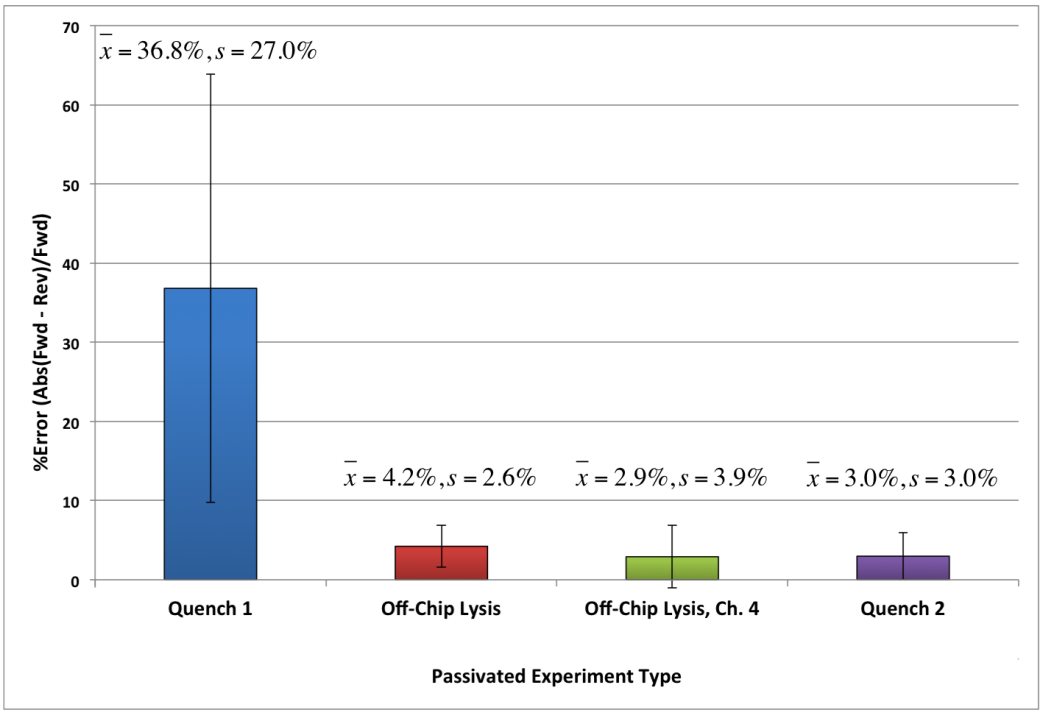

Figure 5.13: Comparison of absolute %errors using different quenching techniques. The "Quench 1" label denotes on chip lysis and quenching with 0.6% (w/v) sodium carbonate and 3% (w/v) sodium chloride in DI quenching solution (n = 8); "Off-Chip Lysis" denotes standard off-chip lysis/quench followed by wash/resuspension in 1% BSA PBS (pH 7.4) solution (n = 9); "Off-Chip Lysis, Ch. 4" denotes error from reverse differential counting with passivated capture chambers from the previous chapter (n = 14); "Quench 2" represents on-chip lysis and quenching with 0.6% (w/v) sodium carbonate in 2.1x PBS quenching solution (n = 20).

5.4.2 Erythrocyte Lysis and Quenching Time Optimization

Figure 5.14 illustrates how on-chip lysis duration affects the population distribution of the leukocytes. Each scatterplot compares the low frequency impedance (303 kHz) to the opacity—the ratio of the high frequency impedance at 1.7 MHz to the low frequency impedance—for a particular lysis time. The low frequency impedance level is proportional to the size of a cell, while the electrical opacity gives information about a cell's membrane that is independent of cell size [103, 107, 117]. It can be seen that as lysis time increases, a portion of the granulocytes/monocytes population transitions from its original population (2 s), to between the lymphocytes and granulocytes/monocytes population (4 – 6 s), to its final position which partially overlaps the smaller-sized portion of the lymphocyte population (8 – 10 s). Holmes *et al.* noted that short-term exposure of leukocytes to saponin during lysis can damage the membranes of some leukocytes subsets [117]. Also, it is well known that saponin is used to permeabilize cells' cytoplasmic and nuclear membranes by solubilizing membrane cholesterol, but does not affect cell morphology or membrane antigen expression [147]. This may explain the aforementioned transition: some granulocytes' and/or monocytes' membranes become progressively more permeabilized as the lysis time increases. Eventually, the membranes become fully permeabilized, forming the third population of cells, shown in Fig. 5.14(e). At 303 kHz, the permeabilized cells cannot be represented as non-conducting particles anymore, as electrical conduction takes place through the cell, resulting in smaller 303 kHz impedance (a 64% decrease between the granulocyte/monocyte population and the permeabilized population in Fig. 5.14(e)). The 1.7 MHz impedance also decreased (42%) for similar reasons, but not to the same extent as at 303 kHz—which explains the 63% increase in the permeabilized population's opacity. One possible explanation is the fact that the high frequency impedance would already be electrically interrogating *unpermeabilized* cells' interiors. This is unlike low frequency interrogation, where cells block all electrical conduction and the impedance is directly proportional to the volume of fluid that is displaced by each cell.

We group the granulocyte and monocyte populations together because we cannot electrically distinguish the two. Holmes *et al.* have shown that the two populations have similar low frequency impedance characteristics (cell

size), but the monocytes' opacity was slightly less than the granulocytes, allowing them to differentiate the two populations (Fig. 2.12). We do not observe this difference, but assume the monocytes are included with the granulocyte population. Our coplanar electrode configuration may prevent us from seeing this slight difference in opacity, as their vertical (top-bottom) electrodes configuration may remove possible error caused by cells passing the electrodes at varying heights—creating a more sensitive system [107,117].

Figure 5.15 shows the recovery of leukocytes and leukocyte subpopulations for a range of on-chip lysis durations. Recovery percentage is based on the ratio of the chip concentration to the control concentration. The granulocytes/monocytes were gated similarly to the dashed areas in the inset of Fig. 5.15, which includes the permeabilized population. Lymphocyte gating is shown by the solid ellipse of the same inset. The total leukocyte recovery of 55 – 65% for all durations shows considerable leukocyte loss, which can be attributed to the loss of granulocytes/monocytes—a population which has already been shown to be affected by the lysis process (Fig. 5.14) and comprises the majority of total leukocytes ($\sim$67%, n = 15). For example, at a lysis time of 2s, the 36% loss of granulocytes/monocytes contributes to 24% total leukocyte loss, while the 51% lymphocyte loss contributes 17% to the total loss. The decrease in granulocytes/monocytes and increase in lymphocytes starting at 4 s is most likely from the permeabilized granulocytes/monocytes population overlapping and being gated with the lymphocytes population. This results in false positives for lymphocyte counts and an apparent loss of of cells in the granulocytes/monocytes population.

This aggressive lysing method lyses all erythrocytes within seconds, which is optimal for a microfluidic point-of-care platform. Gentler lysing methods may give a higher leukocyte recovery, but can take up to 15 minutes and, from our experience, are not as successful in removing enough erythrocytes to provide accurate leukocyte analysis using the electrical differential counting technique. However, is the rapid lysing technique deleterious for the CD4+ T cells? We have used flow cytometry to compare CD4+ T cell recoveries for the aforementioned rapid lysis technique (performed off-chip) and a commercial method (Becton Dickinson Pharmlyse$^{\text{TM}}$). We found that although there was a loss of 20% of total leukocytes compared to the Pharmlyse$^{\text{TM}}$, the rapid lysis technique showed only a loss of 1% CD4+ T cells (n = 4). Although the lysing dynamics may be different in the microfluidic environment, it is

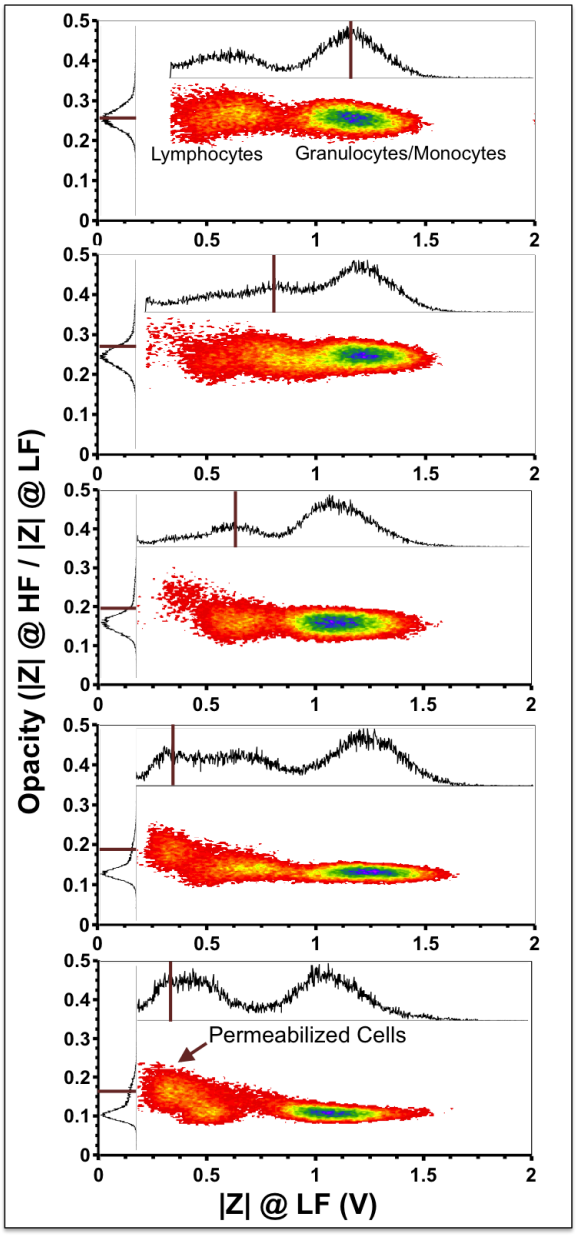

Figure 5.14: Low frequency impedance (303 kHz) vs. opacity (|Z| @ 1.7 MHz / |Z| @ 303 kHz) scatterplots showing the effects of microfluidic lysing duration on the granulocyte/monocyte population. (a) – (e) represent 2, 4, 6, 8, and 10 s lysing times, respectively. A distinct third population of permeabilized granulocytes/monocytes can be seen for 10 s lysis duration. The vertical lines in the inset low frequency impedance histograms show the estimated mean of the permeabilized population's movement toward the lower impedance regime from 2 s to 10 s. The horizontal lines in the inset opacity histograms show the estimated mean of the same population during its rise in opacity from 2 s to 10 s.

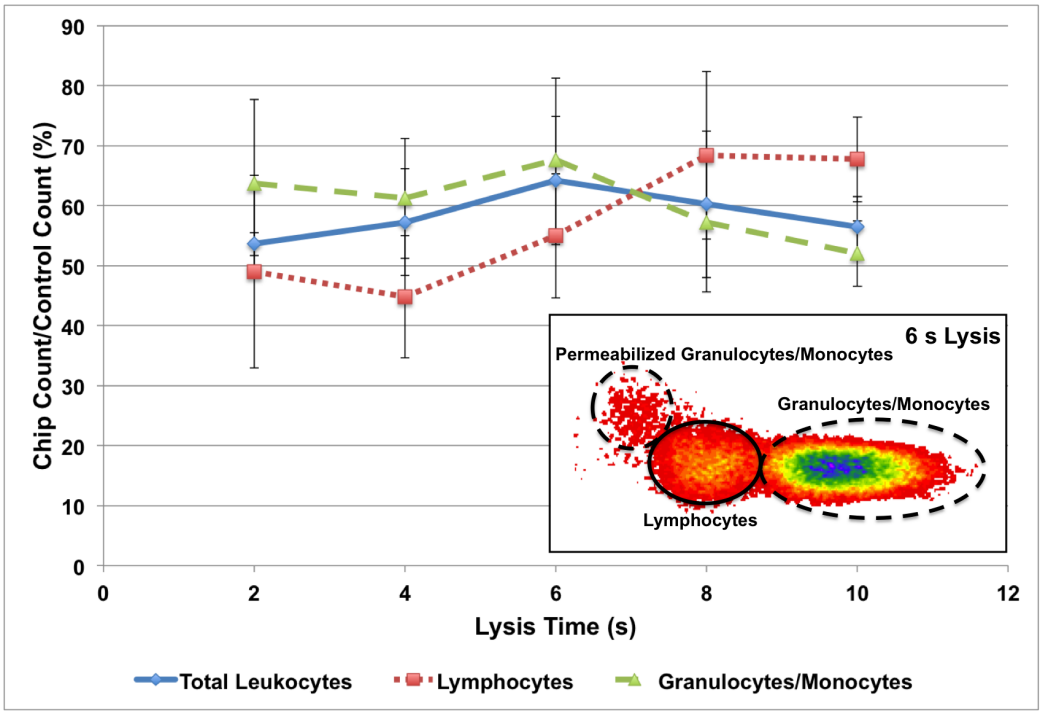

Figure 5.15: Recovery percentages for varying lysis durations for leukocytes and leukocyte subpopulations. The solid, dotted, and dashed lines denote total leukocyte, lymphocyte, and granulocyte/monocyte recovery, respectively. n = 6 for the 2 s data, while n = 3 for all the other lysing durations. The inset shows an example of how lymphocytes and granulocytes/monocytes were counted in a low frequency impedance (x axis) vs. opacity (y axis) scatterplot for a 6 s lysis duration. The solid ellipse denotes lymphocyte gating, while the two dashed areas denote the total granulocyte/monocyte populations. It is assumed that the third population is permeabilized granulocytes and monocytes.

possible that even if 50% of leukocytes are lost after lysis, all of CD4+ T cells may have been successfully recovered, given that in our experiments the average percent of total leukocytes that were CD4+ T cells was 13% (from 15 different donor samples).

Figure 5.16 shows how quenching duration affects the quality of the electrical signal and the ability to accurately count leukocytes. Quenching times of 7.5 s and 11.3 s do not allow the saponin to completely disassociate the erythrocyte fragments or ghosts that were created from the exposure to formic acid [117]. These ghosts still create an appreciable change in impedance when they pass through the counter, resulting in a baseline noise level which masks many leukocytes. The low frequency impedance pulse histograms shown in Fig. 5.16(b) and (d) show that the erythrocyte debris dominates all counts. Complete erythrocyte lysis and debris removal seem to occur between 11.3 s and 15.4 s, as the pulse signal-to-noise ratio in Fig. 5.16(e) is similar to that found by analyzing leukocyte populations that were prepared using off-chip techniques, which includes lysing, quenching, and washing twice via centrifuge. In addition, the baseline noise at 15.4 s is similar to that found for the longer quench durations in Fig. 5.16(g) and (i). The histograms shown in Fig. 5.16(f), (h), and (j) show how the erythrocyte debris peak at the far left of the distribution at 15.4 s decreases as quenching time is increased until it is completely removed at 48.3 s, showing only the lymphocyte and granulocyte/monocyte populations. Therefore, the minimum quenching time should be approximately 48 s to ensure that all erythrocyte debris is removed, ensuring adequate separation from the electrical noise and that no debris is falsely counted as leukocytes. Figure 5.17 shows micrographs of the counter region for the same quenching experiments, confirming that a considerable amount of debris exists for 7.5 s, is lessened at 11.3 s, and is completely removed at 48.3 s.

5.4.3 CD4+ T Lymphocyte Capture Efficiency

Figure 5.18 shows flow cytometry data using the aforementioned labeling protocol to isolate the lymphocytes and CD4+ T lymphocytes. Figure 5.18(a) shows how total lymphocytes are gated based on their unique side scattering vs. CD45 fluorescence intensities. Figure 5.18(b) breaks down the lympho-

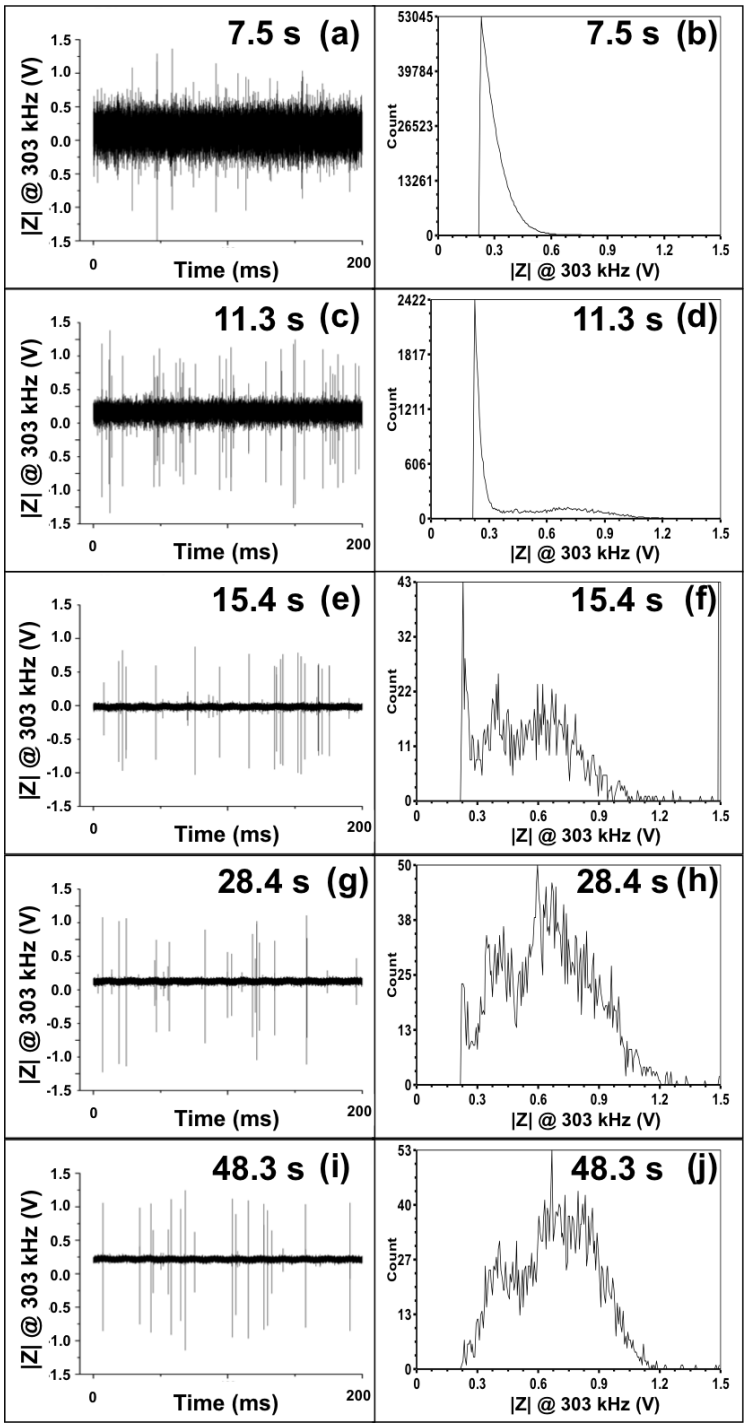

Figure 5.16: Impedance signals (a, c, e, g, i) and resultant pulse height histograms (b, d, f, h, j) for various quenching times of whole blood samples. Histograms were created by analyzing impedance data using a threshold level of 0.22 V. The plots in (a), (c), (e), (g), and (i) are 200 ms snapshots of the electrical data that was analyzed to create their respective histograms. Impedance pulse plots were plotted at the same scale for pulse height and baseline noise comparison.

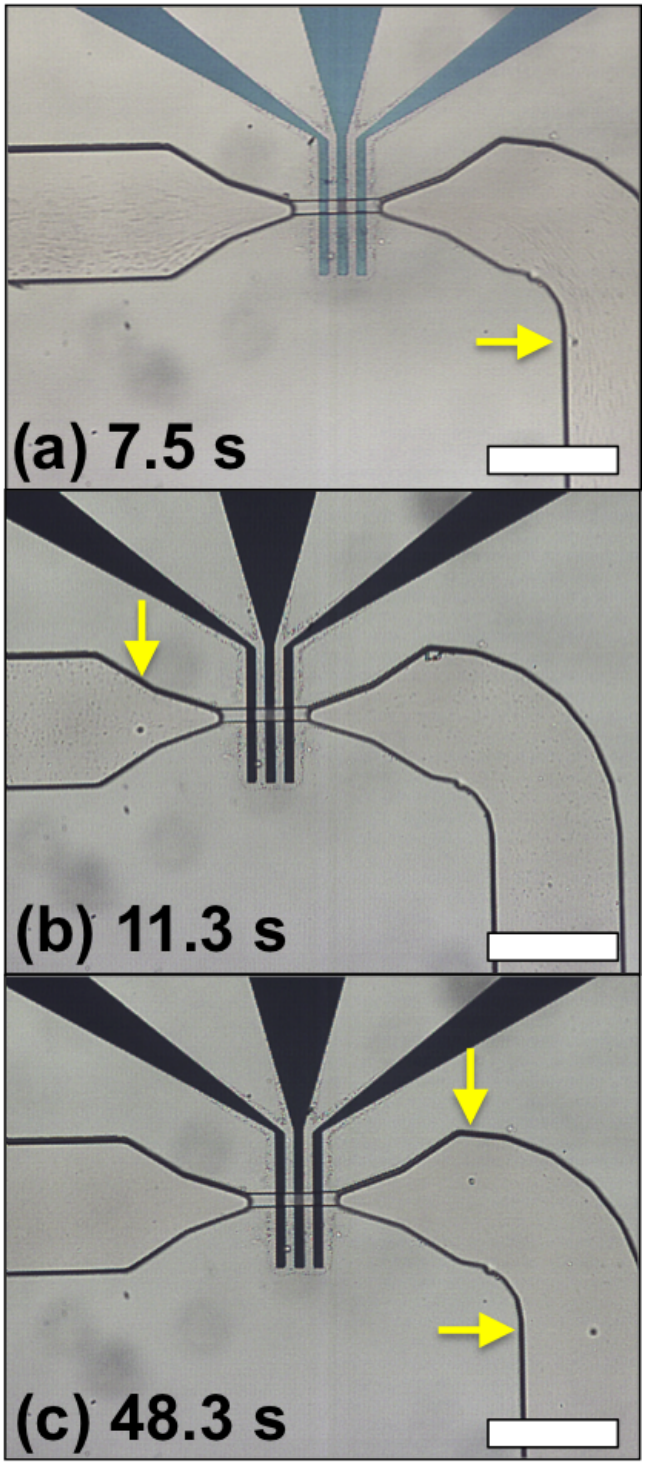

Figure 5.17: Micrographs of the counting channel at different quenching times of whole blood samples. Erythrocyte debris is noticeable for 7.5 s (a), lessens at 11.3 s (b), and is absent at 48.3 s (c). Flow direction is from left to right in all micrographs. Arrows signify the position of leukocytes along the channel. Scale bars are 200 μm.

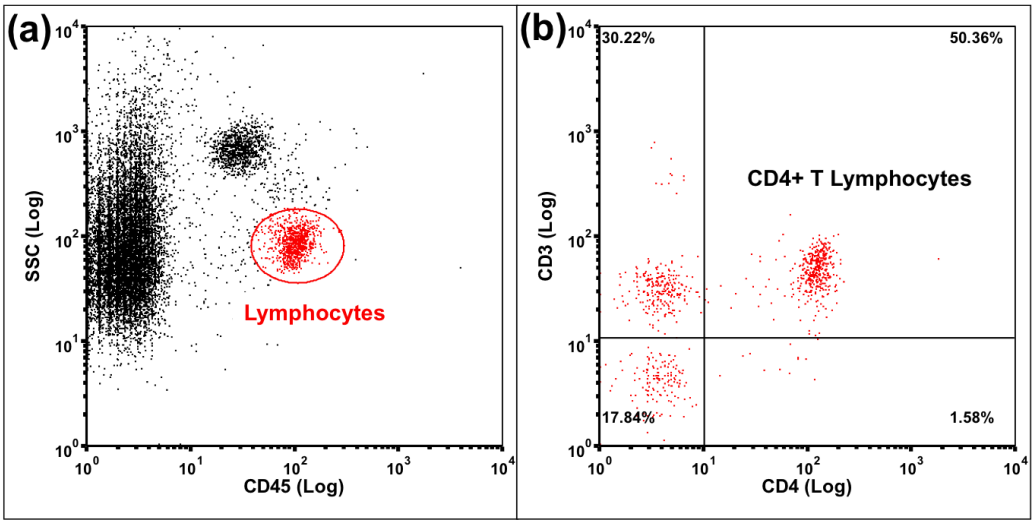

Figure 5.18: Flow cytometry analysis of lymphocytes from on-chip processed whole blood. (a) The lymphocyte population was isolated via its unique side scattering vs. CD45 intensities. (b) CD4+ T lymphocytes were isolated through the presence of CD3 and CD4 antigens within the lymphocyte population gated in (a).

cytes gated in (a) into different lymphocyte subpopulations. Populations of interest include CD4+ T lymphocytes (CD3+CD4+, upper right quadrant), T lymphocytes (CD3+, upper two quadrants), and all lymphocytes (all quadrants). The fraction of lymphocytes that are CD4+ T lymphocytes is calculated based on the number of upper right quadrant events divided by the events in all quadrants (*i.e.*, Eq. 5.3).

Figure 5.19 shows how the capture efficiency increases with decreasing shear stresses and plateaus at 0.333 dyn·cm^{-2} with a maximum of 44.5% efficiency at 0.088 dyn·cm^{-2}. The average efficiency for the plateau is 41.9%, which is somewhat lower to what we found in the off-chip lysis methods from the previous chapter (60.2%). The following are possible explanations for this discrepancy.

1. The capture efficiencies in this chapter may actually be similar to those in the previous chapter, but non-idealities from the differential counting experiments and subsequent capture efficiency analysis itself may be generating artifacts that result in seemingly lower capture efficiencies.

   (a) The nonspecific capture of lymphocytes other than CD4+ T lymphocytes would generate error in calculating capture efficiency.

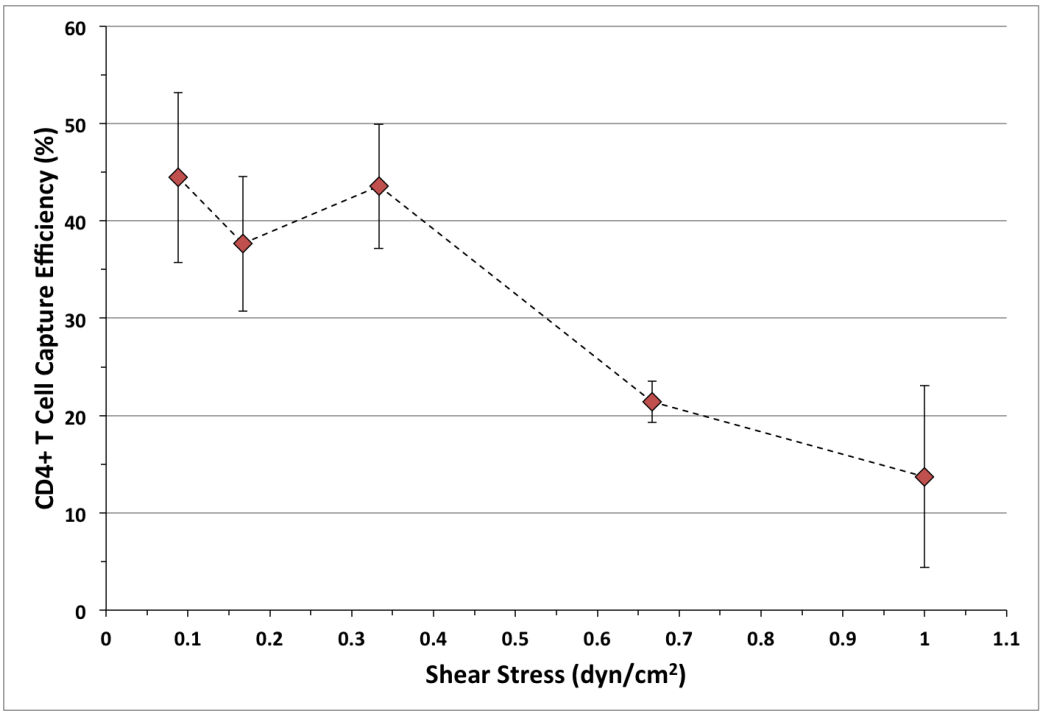

Figure 5.19: CD4+ T cell capture efficiency for various capture chamber shear stresses. Corrections for the capture of lymphocytes that are not CD4+ T lymphocytes, described in the text, resulted in an increase of 2.5, 1.8, 2.6, 1.1, and 0.9 percentage points for 0.088, 0.167, 0.333, 0.667, and 1 dyn·cm^{-2}, respectively. These corrections are reflected in this figure. Iterations: 0.088 dyn·cm^{-2}, n = 6; 0.167 dyn·cm^{-2}, n = 5; 0.333 – 1 dyn·cm^{-2}, n = 3.

This nonspecific capture would lower the number of X_{other} events in Eq. 5.3, increasing the fraction of CD4+ T cells that were not captured by the chip (ξ_{pop2}, Eq. 5.2), resulting in a lower calculated capture efficiency (η, Eq. 5.2) than reality. Adjustments to Fig. 5.19 were made to compensate for this error, assuming all CD4- leukocytes had equal opportunity to be nonspecifically captured. The capture of these *other lymphocytes* was estimated by knowing the percent of these cells compared to all leukocytes (via flow cytometry control) and the percent of nonspecific capture of CD4- leukocytes for a particular capture chamber shear stress (see 5.4.4). Multiplying these two terms gives the fraction of *other lymphocytes* that were captured, and that should be added to X_{other} in Eq. 5.3 to ensure the most accurate capture efficiency analysis. This resulted in an average increase of 1.8% in capture efficiency for all shear stresses, which far from covers the discrepancy between the capture efficiencies found in this chapter and the previous chapter.

(b) Another possible source of error is that the on-chip lysis process and larger cell residence times using the methods in this chapter may cause damage to the lymphocytes that are not CD4+ T lymphocytes, causing delayed death before being analyzed by flow cytometry. With respect to the capture efficiency calculations, this would create the same effects as if these lymphocytes were nonspecifically captured in the capture chambers, resulting in a lower capture efficiency than it truly is. No corrections can be made for this error using the aforementioned capture efficiency analysis protocol, as this protocol relies solely on the ratios of cells. It is possible to compensate for this in future experiments by adding a known number of fluorescent counting particles to the samples before flow cytometry analysis to find the absolute concentrations of the lymphocytes and lymphocyte subsets. Comparing the concentrations between the population of cells that were simply lysed and quenched and the population of cells that went through the entire differential capture process would show how many lymphocytes were actually lost from the differential counting process. Other

possible solutions to this source of error are listed in 5.4.5.

2. Several suggestions for why the on-chip sample processing results in a lower capture efficiency than the off-chip method stem from the fact that the methods described in the previous chapter in preparing the purified leukocyte population vary significantly compared to the on-chip lysis sample preparation that is described in this chapter. Both methods lysed erythrocytes and quenched the lysis process using similar chemicals and lysis times, but the similarities end there. For the off-chip lysis method, the remaining leukocytes were washed twice in a 1%BSA in PBS (pH 7.4) solution, resuspended in the same solution, and stored on ice for at least 30 minutes before capture experiments. On-chip lysis and quenching resulted in a purified leukocyte population suspended in PBS (pH 7.4) containing saponin, the products of neutralizing formic acid with sodium bicarbonate, and erythrocyte debris. These purified leukocytes could make it into the capture region in as little as 30 s after lysis. Some suggestions:

   (a) The erythrocyte debris may be interfering with antigen-antibody binding dynamics. Although the erythrocyte debris is undetectable optically via microscope and electrically via impedance analysis, its presence at the molecular level cannot be neglected, and may partially block the interactions between the helper T cells' CD4 receptors and the immobilized CD4 antibodies on the chamber floors.

   (b) The lysis solution may cause hypotonic swelling of the leukocytes, partially damaging or removing microvilli which contain the CD4 antigens on their tips [148]. This would hinder antigen-antibody interactions, as the microvilli are known to aid in cell adhesion to surfaces in vitro and in vivo circumstances [148,149]. This may not happen to all CD4+ T cells since a portion of them are captured. A possible explanation for this is that some of the cells are exposed to the lysis solution longer during the initial diffusive mixing of blood and lysis solution, which is relatively slow in the laminar flow regime. If this damage is temporary, the cells processed off-chip may have enough time to recover before passing through the

capture chambers—a luxury the on-chip processed cells do not have.

(c) The presence of saponin, commonly used to permeabilize living and fixed cells for internal labeling studies, may cause problems with cell antigen expression, effectively reducing the number of captured cells. However, multiple sources have shown that lymphocyte surface antigen functionality was not impeded by the presence of saponin and that this permeabilization is reversible if the saponin is washed away [147, 150].

3. Another reason for the differences between the capture efficiencies found in this chapter and the previous chapter could be that we used different antibody clones at different concentrations. The concentration of antibody used to coat the capture chambers was 20 μg·mL^{-1} in the previous chapter, while half the amount was used in this chapter's experiments (10 μg·mL^{-1}). This could understandably lessen the antigen-antibody interaction time and probability, resulting in fewer cells captured.

4. Another possible source of error is the capture chamber length in the design in this chapter is shorter than in the previous chapter (20 mm vs. 34 mm), possibly not allowing as much time for capture. Capture chamber length had to be reduced to fit the additional modules and create a chip with a reasonable footprint for fabrication throughput purposes. However, the reverse flow technique effectively increases the capture chamber length by 100% to 40 mm, which is similar to capture chamber lengths used elsewhere for single flow direction capture of CD4+ T lymphocytes [51, 52, 64].

With respect to the last point, it is possible that some cells are not making contact with the capture chamber floor to facilitate capture. Therefore, it is imperative to ensure the sedimentation process has enough time to cause the lymphocytes to reach the floor of the capture chambers to interact with the immobilized CD4 antibody. We can obtain an estimate of the sedimentation velocity of lymphocytes with the equation [151]

$$w = \frac{(\rho_p - \rho_f)r^2}{4.5\mu}g \tag{5.4}$$

where ρ_p and ρ_f are the densities of lymphocytes (1.075 g·mL^{-1}, [152]) and suspending medium (1.01 g·mL^{-1}), respectively. The suspending medium was assumed to have a density similar to that found in a 1x concentration of PBS (pH 7.4). The radius of the lymphocytes, r, is estimated to be 3.9 μm, which was determined from the average lymphocyte volume found by Zipursky *et al.* [152]. The dynamic viscosity of the suspending medium, μ, was empirically found to be 1.33 cP by measuring lysed and quenched whole blood using a viscometer in our laboratory. The acceleration due to gravity is denoted as g. Using the aforementioned equation and values, the sedimentation velocity of lymphocytes was found to be 1.62 μm·s^{-1}.

Cell residence time in the chamber, t_{RES}, is based on the average fluid velocity through the capture chamber, and is defined

$$T_{RES} = \frac{L_C W_C H_C}{Q_T} \tag{5.5}$$

where L_C is the chamber length (20 mm), W_C is the effective capture region width (2 mm x 8 chambers = 16 mm), H_C is the capture region height (varies), and Q_T is the sum of the sample, lysis, and quenching solution volumetric flow rates (varies). At a shear stress of 0.167 dyn·cm^{-2}, cell residence time in the capture chamber is approximately 86 s in either the forward or reverse flow direction. Multiplying this time by the previously calculated sedimentation velocity would result in a downward vertical displacement of ∼140 um for lymphocytes. Given that 115 μm tall capture chambers were used for the 0.167 dyn·cm^{-2} shear stress experiments, all lymphocytes should settle to the floor of the capture region well before exiting it because their settling distance would be over 1.21 times the height of the chamber.

Figure 5.20 summarizes the fraction of a chamber's height settled by lymphocytes for all shear stresses. The fraction was found by dividing the sedimentation displacement distance by the height of the chamber. These calculations allow for proper comparison between different shear stresses, as several capture chamber heights and different flow rates were used to obtain the specific shear stresses and to reduce leukocyte residence time in the chip to avoid cell loss. It is interesting to note that the fractions found for both 0.088 and 0.333 dyn·cm^{-2}, which had relatively high capture efficiencies, are

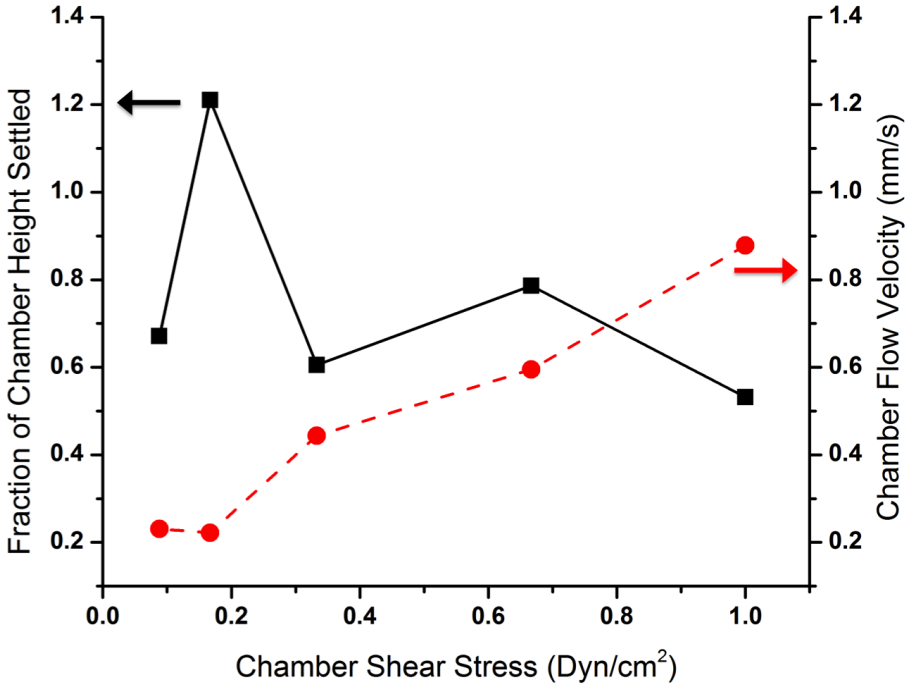

Figure 5.20: Relationship between ratio of capture chamber height settled by lymphocyte sedimentation and shear stress (solid line, left y-axis), and the relationship between the average capture chamber fluid flow velocity and the shear stress (dashed line, right y-axis). Capture chamber heights used for particular shear stresses were 208 μm for 0.088 dyn·cm^{-2}, 115 μm for 0.167 and 0.333 dyn·cm^{-2}, and 70 μm for .667 and 1 dyn·cm^{-2}.

below unity and are similar to those found at the higher shear stresses, which had much lower capture efficiencies. This may mean that the lymphocytes are already near the floor of the chambers when they enter, reducing the distance necessary to settle to the floor. This is possible, given the leukocytes were funneled down toward the floor of the 15 μm counting channel, and may have remained near the floor of subsequent taller channels.

Since the cells most likely are making it to the surface of the capture chamber for all tested shear stresses, another main factor determining CD4+ T cell capture is the velocity of the cells along the chamber floor. At smaller shear stresses, the slower rolling velocity of the cells on the capture chamber floor allows more interaction time with the immobilized antibodies, increasing the probability of capture. The average chamber flow velocities used in the capture experiments are depicted in Fig. 5.20, showing that the lower average

flow velocities correlate with the shear stresses which gave the highest capture efficiencies, and that at velocities above 0.45 mm·s^{-1} the cells do not have enough interaction time with the CD4 antibodies. It is not to be implied that the calculated average chamber flow velocity is the actual rolling velocity of the cells on the surface of the chip, but that the latter is directly proportional to the former.

Even if the capture efficiency was similar to the previous chapter (60.2%), it would still be considerably lower than what Cheng *et al.* reported (above 90%) because it lacks the leukocyte margination effect that is caused by the presence of the erythrocytes [51, 139]. Whereas their method depends on the erythrocytes to push the leukocytes against all chamber walls, our method depends on sedimentation to cause the leukocytes to land and then roll along the floor of the capture chambers. The capture efficiency could be enhanced by using covalent chemistry to ensure the proper orientation of the antibodies' antigen binding regions, ultimately increasing interaction time and probability between the CD4+ T cells and the immobilized antibodies. Moon *et al.* have used such a chemistry for capturing CD4+ T lymphocytes that were rolling along the floor of the capture chamber, but were still only able to obtain a 70.2% capture efficiency [60].

Capture efficiency could further be improved by decreasing the chamber height to be similar to the size of the cells to force more cell-surface interaction, but the effective width of the capture region would have to be prohibitively large to ensure low shear stresses at sample flow rates to keep the diagnostic duration below 15 minutes. For example, to have 10 μm-high capture chambers and to operate at 0.167 dyn·cm^{-2} to have 10 μL of blood analyzed within 10 minutes, the effective width of the capture channel region would have to be over 4.75 m wide, which is obviously impractical for any situation, much less for point-of-care applications. Microposts coated with antibodies have been shown to increase the efficiency of capturing rare circulating tumor cells [153]. The increase in surface area using a similar micropost design in the capture chamber may help increase the capture efficiency of CD4+ T cells. For example, microposts can be spaced closely together (*e.g.*, $\sim$10 μm) to force the lymphocytes to interact with the pillar surfaces, while the chamber height can be large enough to ensure that the combination of low enough shear stress and a small chip footprint are possible. This could also increase the capture purity, as higher shear stresses can

be used because of the guaranteed surface interactions with the posts. These higher shear stresses, especially starting at 1 dyn·cm^{-2}, could decrease the nonspecific capture of CD4- leukocytes and the capture of monocytes [51].

5.4.4 CD4+ T Lymphocyte Capture Purity

Figure 5.21 gives the percent of total captured cells for each cell type of interest for a range of shear stresses. The increase in capture purity of CD4+ T cells with shear stress is mostly attributed to the decrease in nonspecific capture of CD4 negative leukocytes (monocytes are weakly CD4+). This is supported by the fact that at a shear stress of 0.088 dyn·cm^{-2}, nonspecific capture of other leukocytes dramatically increases to 54%, resulting in a CD4+ capture purity of only 32%. At such a low shear stress, the leukocytes are rolling so slowly on the channel floor that they have enough time to attach to the glass surface via their integrin receptors. Although monocytes have an order of magnitude less CD4 surface antigen than CD4+ T cells, Eq. 5.4 shows that their larger size ($r = 5.03\ \mu$, [152]) ensures they will settle to the chamber floor 1.6 times faster than lymphocytes, having ample time to interact with the CD4 antibodies at all shear stresses [51, 136, 137]. This is supported by the fact that the percent of captured cells being monocytes is similar for all shear stresses ($\bar{x} = 18.4\%$, s = 3.7%.).

The capture purity for the previous chapter was ∼82% at 0.5 dyn·cm^{-2}, which is considerably larger than what was found in this chapter (∼60%, estimated for the same shear stress). The main reason for this discrepancy is the fact that the leukocytes were in a 1% BSA solution in the previous chapter, acting as a blocking agent to prevent nonspecific capture of leukocytes. No blocking agent was present in this chapter's capture experiments. The percent of other leukocytes captured at this shear stress in this chapter's data is ∼20%. Assuming blocking would prevent all nonspecific capture, the estimated capture purity would be around 80%, which would match the previous chapter's data.

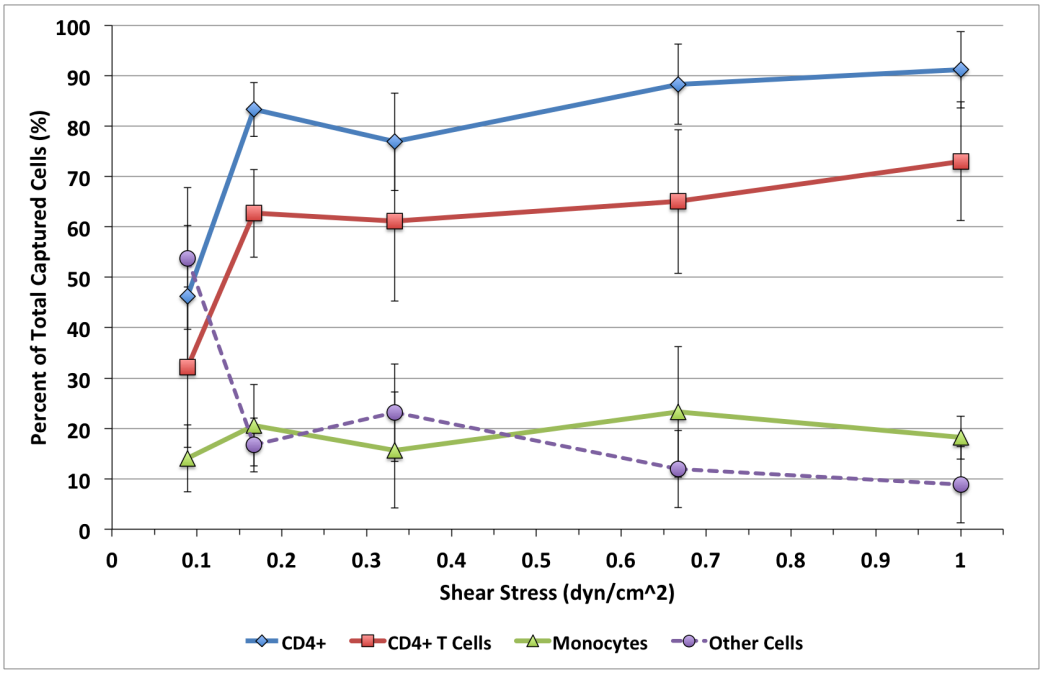

Figure 5.21: Percent of total captured cells vs. capture chamber shear stress for all CD4+ cells, CD4+ T cells, monocytes, and other leukocytes. The "All CD4+ cells data" is obtained by adding the monocytes and CD4+ T cell percentages. CD4+ T cell capture purity peaks at 73% at 1 dyn·cm^{-2}, slightly decreases to an average of 63% (s = 1.9%) for 0.167 – 0.667 dyn·cm^{-2} before further decreasing to 32% for 0.088 dyn·cm^{-2}. Iterations: 0.088 dyn·cm^{-2}, n = 6; 0.167 dyn·cm^{-2}, n = 7; 0.333 dyn·cm^{-2}, n = 11; 0.667 dyn·cm^{-2}, n = 10; 1 dyn·cm^{-2}, n = 4.

5.4.5 CD4+ T Lymphocytes Comparison: Electrical Differential Counting vs. Flow Cytometry Control

Sixteen blood samples were analyzed using the electrical differential counting technique to find the concentration of CD4+ T lymphocytes. Nine of the blood samples were diluted using their own plasma to provide a range of CD4+ T cell counts (1:2 to 1:20 dilutions). These results were compared to the flow cytometry control, obtained from the Carle Foundation Hospital Laboratory. A chamber shear stress of 0.167 dyn·cm^{-2} was used for these capture experiments because its relatively high capture efficiency (Fig. 5.19) and purity (Fig. 5.21) should provide the most accurate representation of the actual CD4+ T cell concentration. A shear stress of 0.333 dyn·cm^{-2} could have also been used, but it was assumed that the capture efficiency at 0.167 dyn·cm^{-2} would be the same or greater because the cells would have more opportunity to interact with the immobilized antibodies on the capture chamber floors at the slower flow speeds—despite the minor dip in its capture efficiency.

Figure 5.22 shows the low frequency impedance vs. opacity scatterplots for forward (a) and reverse (b) counts for a particular capture experiment. It also shows how the total number of leukocytes were gated for both counts. The reverse counting gate was slightly modified to follow the contour of the permeabilized cells to avoid counting the noise that is not present in the forward counts. The source of the noise could be debris from leukocytes that died and ruptured in the capture chambers or exit holding coil.

Figure 5.23 compares the electrical differential counting method to the flow cytometry control for all 16 iterations, showing good correlation between the two methods ($y = 1.068x$, $R^2 = 0.946$). Multiple repetitions were analyzed using the chip for the same donor sample, and showed high repeatability, especially for the lower CD4+ T cell concentrations. The high correlation with the "golden standard" of flow cytometry and high repeatability suggests that this electrical differential counting method with on-chip sample preparation is a viable technology to provide portable and rapid CD4+ T cell counts for patients in resource-poor regions.

This high correlation was not expected, given that the capture efficiency and purity were approximately 42% and 63% for this shear stress regime. Equation 5.6 relates the flow cytometry CD4+ T cell concentration control

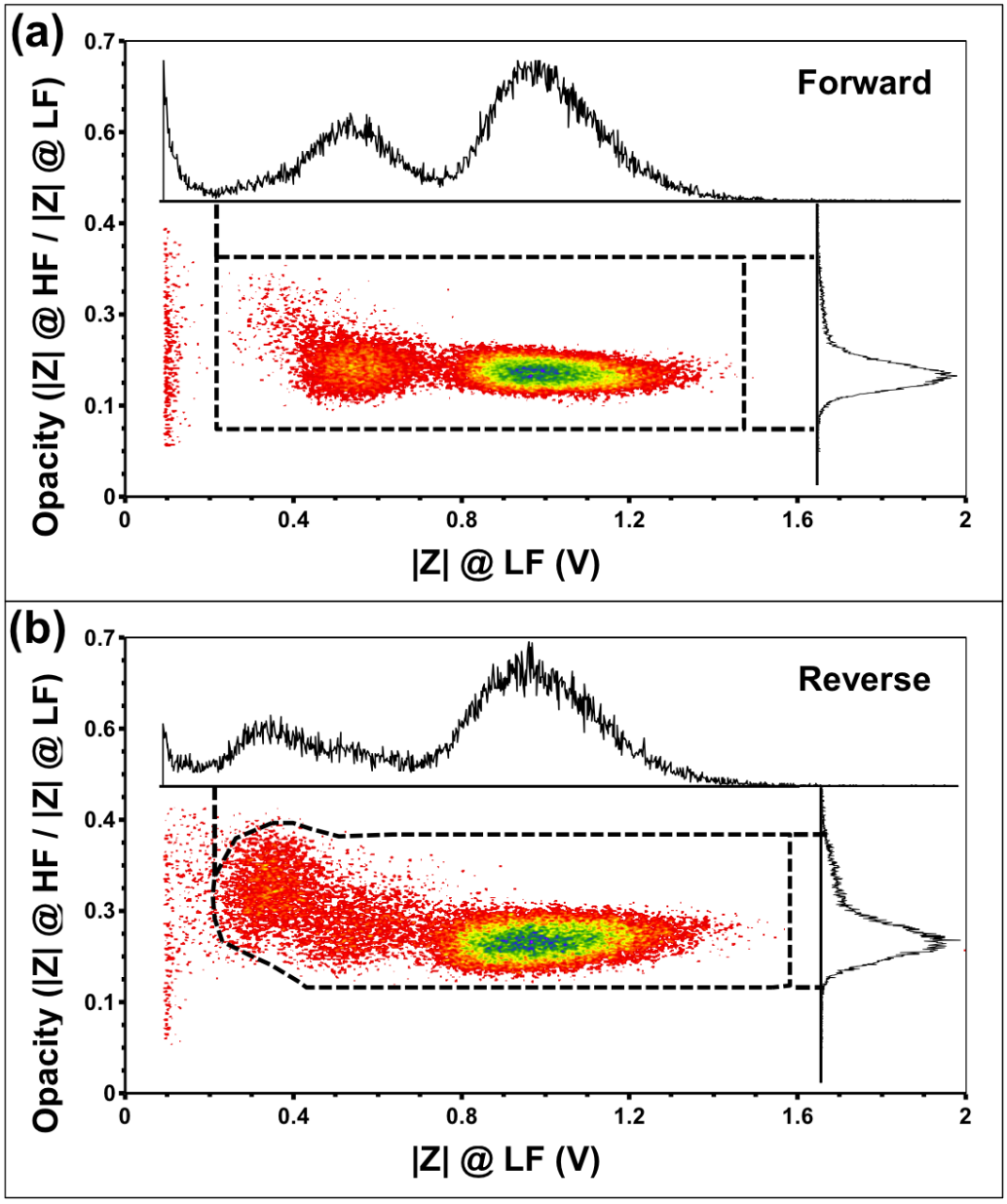

Figure 5.22: Low frequency impedance vs. opacity scatter plots of a CD4+ T lymphocyte capture experiment. Capture chamber shear stress was 0.167 dyn·cm^{-2}. The dashed boxes indicate the gates used to determine the total leukocyte counts for the forward (a) and reverse (b) flow directions.

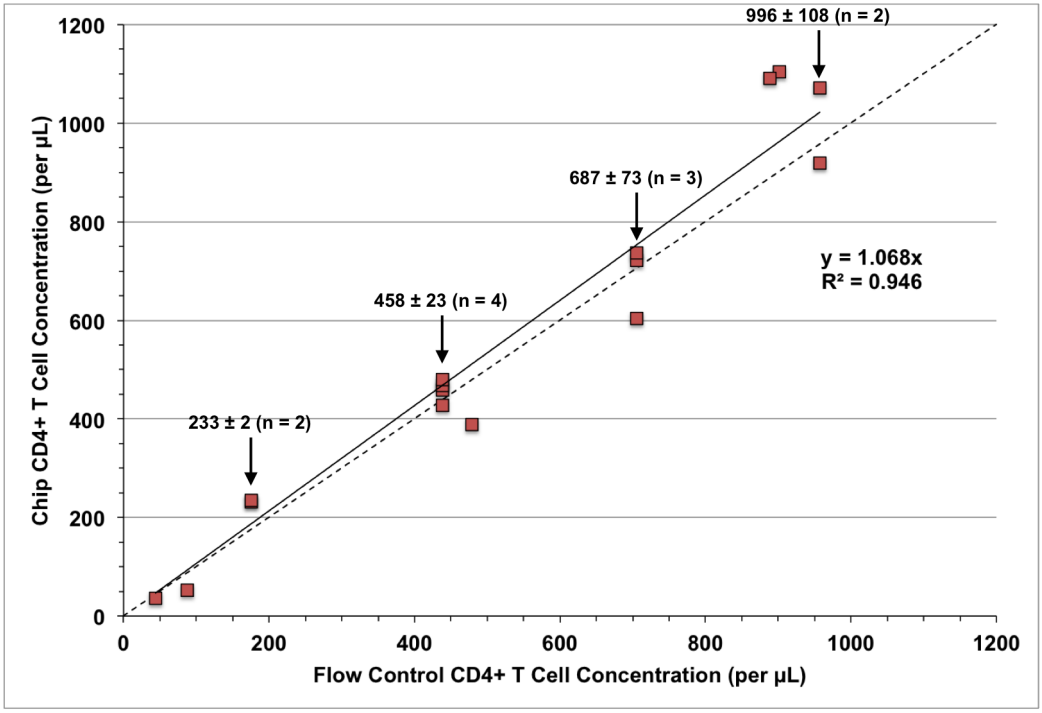

Figure 5.23: Comparison between CD4+ T cell concentrations from the flow cytometry control and the electrical differential counting method (n = 16). The dashed line represents perfect correlation between the two analysis methods. The solid line represents a linear fit of all 16 points (y = 1.068x, $R^2 = 0.946$). Outliers were removed with a 99.99% confidence, assuming a T distribution. Average cell concentration and standard deviation are given for repetitions in chip analysis for the same sample. The number in parentheses denotes how many iterations were performed, which can be difficult to differentiate because of datapoint density.

(T_{ctl}) to the electrical differential count (T_{chip}) through the capture purity (α), capture efficiency (η, Eq. 5.2), and CD4+ T cell recovery after erythrocyte lysis and quenching (β).

$$T_{chip} = \frac{\eta\,\beta\,T_{ctl}}{\alpha} \tag{5.6}$$

It is assumed that β is unity because of our previous investigations (5.4.2). Given the aforementioned capture efficiency (42%) and purity (63%), T_{chip}/T_{ctl} would be 0.67, which means that, on average, chip counts should be 33% less than the control counts. However, Fig. 5.23 shows that, on average, chip counts are ∼7% larger than the control counts (based on the slope of the linear fit).

The author believes that this discrepancy is primarily caused by the errors in *obtaining* the capture efficiency, which are detailed in 5.4.3, reasoning 1, with emphasis on (b). As shown in Fig. 5.8, the capture efficiency protocol requires many steps where cells can be lost or damaged. The duration the leukocytes are exposed to the lysis/quenching mixture before being diluted in the waste vial for population (1) is less than a minute. The leukocytes in population (2), however, may be in the mixture for over 35 minutes. This time difference between the two populations supports the idea that the vitality of population (2) is substantially less than (1). In addition, the total time between leukocytes leaving their optimal environment in whole blood and actual efficiency analysis in the flow cytometer is also a concern, as the cells in population (2) are out of their optimal environment for over 75 minutes, most likely affecting their vitality. Fixing the cells could sustain their morphology, but this step would have been performed after fluorescent labeling of the cells—which is already at the end of the efficiency analysis protocol and would have added several more processing steps.

In contrast, capture purity analysis has proven to be a more reliable process. It directly obtains the capture purity of cells by imaging a single population of leukocytes that were captured on chip. In contrast, the capture efficiency experiments compares two different populations of leukocytes that went through a different number of steps of different total durations, most likely with different vitalities. This leads us to believe that α in Eq. 5.6 is an accurate representation of capture purity.

With α being a good representative of capture purity, the feasibility that CD4+ T cell recovery after lysis is unity ($\beta = 1$), and given the high correlation between the chip and control counts ($y = 1.07x$, or $T_{chip} \approx T_{ctl}$), the only variable unaccounted for is capture efficiency (η). In fact, if the capture efficiency was indeed 60% as found in the previous chapter, Eq. 5.6 would result in a T_{chip}/T_{ctl} of 0.95. This would complement the 1.07 ratio that is observed from the chip vs. control counting data in Fig. 5.23.

Capture efficiency experiments can be improved to better ensure the aforementioned errors are minimized and/or compensated for. Some suggested modifications are listed below.

1. Fluorescent counting beads can be used to obtain the absolute concentrations of the lymphocytes and lymphocyte subsets during flow cytometry analysis, giving vital information regarding how many lymphocytes were lost (5.4.3).

2. Experiments need to be modified to ensure that the vitality of the lymphocyte (and leukocyte) population is maintained throughout the entire differential counting and capture efficiency analysis processes. This may be done by optimizing the capture chamber height to ensure a shear stress of 0.167 dyn·cm^{-2} at the fastest total flow rate possible (60 μL·min^{-1}, based on the pumping system's maximum infusion rates) to ensure cell duration in the chip's non-ideal environment is minimal.

3. BSA could be added to the quenching solution to simulate the same on-chip conditions found in the previous chapter, possibly increasing the vitality of the cells.

4. Capture efficiency experiments could also be run that negate the reverse flow step to also shorten cell residence time in the chip and also quantify the capture efficiency of performing a single pass through the capture chambers (it could be possible that only one pass would be needed).

5. Decreasing on-chip lysis time below 2 s may improve lymphocyte (and total leukocyte) recovery, allowing lymphocytes to remain alive longer in the non-ideal, on-chip environment.

6. Obtaining capture efficiency more directly by analyzing the captured cells in the same manner as used in capture purity analysis may re-

duce error. Captured cells can be fluorescently tagged with CD3+ and CD4+ antibodies, and the ratio of the CD3+CD4+ helper T cells to total T cells (CD3+) can be compared to the same ratio found using the flow cytometry control of the same blood sample source.

5.5 Conclusions

In this chapter, we have evaluated an electrical differential counter with an on-chip sample preparation module to evaluate whole blood samples for CD4+ T lymphocyte concentration. We found that erythrocyte lysis is quick and rigorous, leading to leukocyte casualties. However, preliminary experiments have shown that the CD4+ T cells were not affected by off-chip lysis and quenching, as they showed high recovery (99%). Lysis times less than 2 s may result in higher leukocyte recovery, allowing the differential counter chip to accurately provide the total lymphocyte and granulocyte/monocyte concentrations in addition to the CD4+ T lymphocyte concentration. We found that the quenching solution described in the literature [118, 143] did not maintain leukocyte vitality for the required residence times in the chip ($\geq$ 12 minutes), but modified the solution using concentrated PBS to ensure correct and stable pH and osmolarity. The optimal quenching time was found to be $\sim$48 s to disassociate all erythrocytes, ensuring a debris-free leukocyte solution. The chip's capture purity and efficiency were characterized for different capture chamber shear stresses, and the optimal shear stress of 0.167 dyn$\cdot$cm^{-2} was used to obtain CD4+ T cell concentrations that correlated well with the "gold standard" of flow cytometry. The on-chip lysis of erythrocytes and subsequent immunocapture of the remaining leukocytes is not found in the literature, and requires more detailed characterization between capture efficiency and the resultant chip counts. Efforts should be made to increase the capture efficiency and capture purity, and are discussed in the next chapter.

CHAPTER 6

FUTURE WORK

This chapter briefly discusses future steps that should be taken to better characterize, improve on, and expand the current differential counter design.

6.1 Further Evaluation of Current Differential Counter

6.1.1 Erythrocyte Lysis Duration

In 5.4.2, it was found that approximately 40% of total leukocytes were lost after on-chip erythrocyte lysis, preventing an accurate depiction of total leukocytes, lymphocytes, and granulocytes/monocytes, which is helpful supplementary information to the CD4+ T cell count. Even though initial experiments have shown that CD4+ T cell vitality is not affected by the lysis protocol, it is still possible that other lymphocytes are being affected (*i.e.*, partial damage and delayed death), resulting in a capture efficiency that is lower than it actually is (5.4.3).

Several modifications can be made to investigate this topic. The minimum lysis time can found by reducing lysis duration until just before unlysed erythrocytes are observed at the counter channel. This can be evaluated by looking at the counter region under microscope with the aid of a high speed camera, or by observing the low frequency impedance vs. opacity scatter plots for a noticeable erythrocyte population. The lysis and/or quenching solution concentrations or compositions could also be modified to create a gentler lysing/quenching process.

6.1.2 Capture Efficiency

More iterations of capture efficiency experiments are necessary to fully understand the correlation between the chip's differential count, capture efficiency, lysis recovery, and capture purity. Equation 5.6 has related these terms and shows a discrepancy between the expected and actual relationship between the chip and control counts. It is the author's belief that the actual capture efficiencies are higher than depicted in Fig. 5.19 for the reasons stated in 5.4.3. Mainly, the nonspecific capture or delayed death/lysis of lymphocytes other than the CD4+ T lymphocytes is causing the capture efficiency calculations to result in lower capture efficiencies.

Counting efficiency experiments can be modified to quantify the aforementioned losses of lymphocytes, ensuring an accurate depiction of the capture dynamics of the chip. Specifically, adding a known number of fluorescent counting beads to the labeled solutions would provide the concentrations of total lymphocytes and CD4+ T lymphocytes, rather than simply the ratio between the two populations. The concentrations can be compared between samples that were not injected into the capture chamber and the those that went through the entire differential counting process to see if any lymphocytes, other than CD4+ T cells, were lost. Another solution to reduce error is to perform capture efficiency analysis more directly by using the same methods from the capture purity protocol. This entails fluorescently tagging all captured T cells with CD3 antibodies in addition to labeling all captured CD4+ T lymphocytes with CD4+ antibodies. The ratio of CD3+CD4+ helper T cells to the total number of CD3+ T cells can be compared to the same ratio obtained from flow cytometry. Other proposed solutions are listed in 5.4.5.

Improving lymphocyte vitality would also help ensure more accurate results. Further optimization of lysis time and/or lysis/quenching solution formulations may help preserve lymphocytes (and other leukocytes) during the entire differential counting experiment and subsequent capture efficiency analysis (6.1.1). Reducing cell residence time in the non-ideal saponin, protein-diminished environment found on-chip should also increase cell vitality. This can be done by increasing the total flow rate (blood sample + lysis solution + quenching solution) for faster processing times, given the capture chamber's height is increased to maintain the optimal shear stress of 0.167

$dyn \cdot cm^{-2}$.

6.1.3 HIV Patient Testing

It is necessary to test whether the differential counter can accurately provide CD4+ T cell counts for HIV/AIDS patients in addition to HIV- patients. In Chapter 5, low CD4+ T cell concentrations were created by diluting whole blood before injecting it into the chip. In this case, the ratio between helper T cells and total leukocytes remained the same (8 – 22% range, $\bar{x} = 12\%$, $s = 4\%$; n = 15). In HIV+ patients, this ratio may be much lower, given the selective depletion of the CD4+ T cells. We may need to confirm the counting accuracy because the ratio of leukocytes that were nonspecifically captured to the CD4+ T lymphocytes would increase.

HIV+ patient samples will be obtained from willing participants of the Champaign-Urbana Public Health District (Champaign, IL) using an informed consent process approved by the University of Illinois Institutional Review Board. These samples will be analyzed by the differential counter chip and control counts will be obtained from Carle Foundation Hospital Laboratory (Urbana, IL).

6.2 Improvements on Current Differential Counter

6.2.1 Surface Chemistry

In this dissertation, CD4 antibodies have been immobilized to the capture chamber walls by simple adsorption. A more robust protocol, such as the silane surface chemistry already described, would ensure that a higher number of Fab regions are available to interact with helper T cell surface antigens, increasing the chip's capture efficiency [51,60,141,154]. It could also increase the chip's capture purity, as the presence of silane and linkers should provide a more even and robust coverage over chamber surfaces, more effectively preventing nonspecific binding of other leukocytes.

6.2.2 Enhancing Cell and Chamber Surface Interactions

Moon *et al.* have used the aforementioned silane surface chemistry to capture CD4+ T cells by allowing them to roll along the chamber floor (similar to the capturing methods in Chapters 4 and 5), but only achieved a 70.2% capture efficiency, which is far less than what Cheng *et al.* obtained from flowing whole blood through their capture chambers ($> 90\%$) [51, 60]. This is because the latter capture method relies on erythrocytes to push the leukocytes toward the walls of the capture chamber, ensuring high quality interactions with the immobilized CD4 antibodies. In our case, the necessary step of lysing the erythrocytes before counting prevents us from taking advantage of this phenomenon.

Moon *et al.* said that increasing the capture chamber's length may increase the interaction time between the cells and capture chamber floor, resulting in a higher capture efficiency [60]. However, our reverse flow method allows the cells to interact with the 20 mm capture chamber twice, effectively creating a 40 mm capture chamber length—which is much longer than their 24 mm capture chamber in which they flow their cells through only once. With this fact, it may possible that cells need this mechanical pressure to fully engage the cells' surface antigens with the antibodies on the chamber walls.

A capture chamber of small height ($\sim$10 μm) could be used to do this, as it is similar in height to the average size of the lymphocytes. However, as already mentioned in 5.4.3, the resulting chip's footprint would be prohibitively large to ensure proper capture chamber stress and analysis times.

Nagrath *et al.* used microposts coated with antibodies to increase the efficiency of capturing rare circulating tumor cells (CTCs) [153]. Adams *et al.* used a series of sinusoidal capture channels to also isolate CTCs from blood samples [124]. Stott *et al.* used a herringbone design to create microvortices that enhanced the cell-to-surface interactions [155].

We plan to use an approach similar to Nagrath *et al.* by placing microposts into the capture chamber to not only create more surface area for cell-to-surface interactions, but to mechanically press the cells against the antibody-coated posts. Figure 6.1 illustrates this idea, where leukocytes are forced against and squeezed between pillars, capturing the CD4+ T cells. Figure 6.2 shows preliminary COMSOL simulations of shear stresses in a capture region with pillars. Optimal shear stresses may be more similar to those used

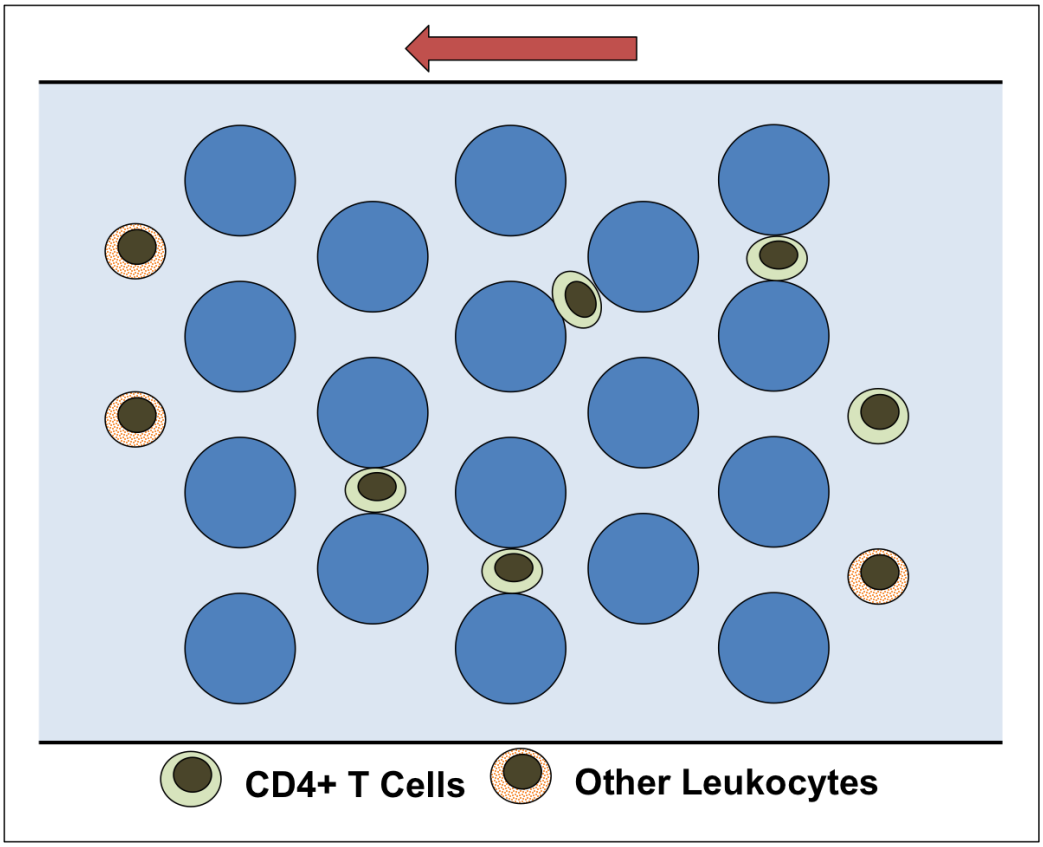

Figure 6.1: Illustration showing leukocytes passing through a capture region comprised of vertical pillars (top-down view). The arrow denotes flow direction. All leukocytes are temporarily squeezed between pillars coated with CD4 antibodies. CD4+ T lymphocytes are captured while the other leukocytes were allowed to pass through the array. Shear stress would be controlled to prevent the capture of monocytes (weakly CD4+) and the nonspecific capture of other leukocytes.

by Cheng *et al.* (1 – 3 dyn·cm^{-2}), as all leukocytes will be pushed between the pillars similarly to the way the erythrocytes forced the leukocytes to the capture chamber walls [51]. Pillar diameter, height, and spacing will need to be optimized to (1) create optimal shear stress at a particular total flow rate, (2) ensure the back pressure generated from the capture chamber is below the maximum to ensure no leaking, and (3) ensure successful and consistent pillar formation (*i.e.*, the height-to-diameter ratio is crucial).

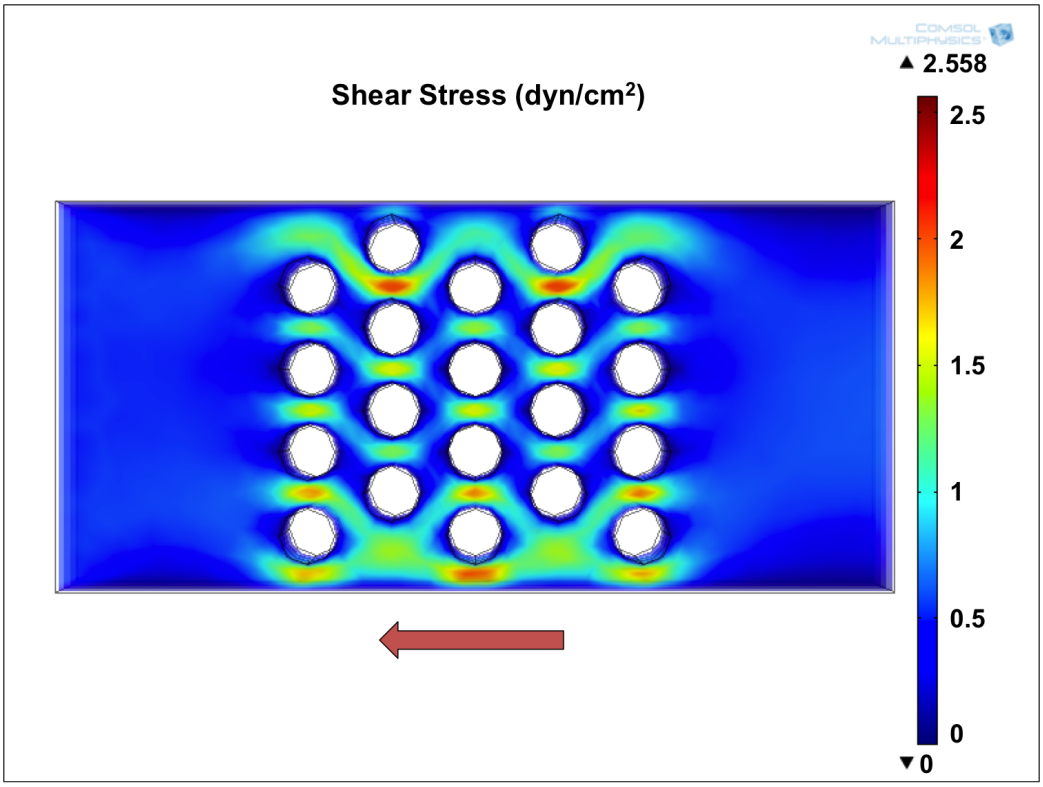

Figure 6.2: COMSOL simulation of shear stresses in a capture chamber arrayed with pillars. The arrow denotes flow direction. Pillar diameter, spacing, and height are 20 μm, 10 μm, and 50 μm, respectively. Capture chamber length, width, and height are 300 μm, 150 μm, and 50 μm, respectively. Flow velocity was chosen to match the flow velocity in the chip design from Chapter 5 at the maximum total flow rates allowed by the pumping system (60 μL$\cdot$min^{-1}), provided the velocity was scaled down because the differences in capture chamber width and height between this simulation and the capture chamber design from Chapter 5.

6.2.3 Revisiting the Single Flow Direction Method

CD4+ T cell counting duration could be halved if a single flow direction was used with electrical counters at both the entrance and exit of the capture chamber. Initial investigations in Chapter 4 showed that this method would not work, as the two counters would have different sensitivities—making it impossible to choose an objective impedance threshold level that determined which pulses were leukocytes. However, the dual frequency interrogation method described in Chapter 5 and elsewhere has shown it is possible to isolate populations based on their shape in the low frequency impedance vs. opacity scatterplots [117, 118]. As a result, entrance and exit counts can be gated separately with the confidence that all leukocytes were accounted for in each case.

A major benefit for the single flow direction method besides shorter analysis time is the fact that the leukocytes' on-chip residence times will be less, resulting in a healthier cell population for exit counts and for subsequent characterization (*e.g.*, capture purity and capture efficiency).

6.3 Expansion of Differential Counter Concept

The advantage of the differential counting approach is that it can be easily adapted to count other cell types simply by changing the immobilized antibodies in the capture chambers. Capture chambers and counters can be multiplexed to provide multiple cell counts in a single chip. This would truly harness the power of working in the microfluidic domain: different screenings could be performed simultaneously, reducing total testing time and cost. Figure 6.3 shows how this idea can be implemented to obtain a complete cell count (CBC) on a chip by using different antibodies specific to particular white blood cell subsets. A CBC is a common and important screening tool which provides physicians with a general assessment of a patient's health to help direct them to further testing and/or treatment. The chip depicted in Fig. 6.3 also includes an erythrocyte and platelet counting region that first dilutes the blood sample to electrically count these cells, which are at much higher densities than leukocytes [118]. Fewer chambers would be needed if dual frequency impedance interrogation was used, as lymphocytes could be easily distinguished from granulocytes (neutrophils, eosinophils, and ba-

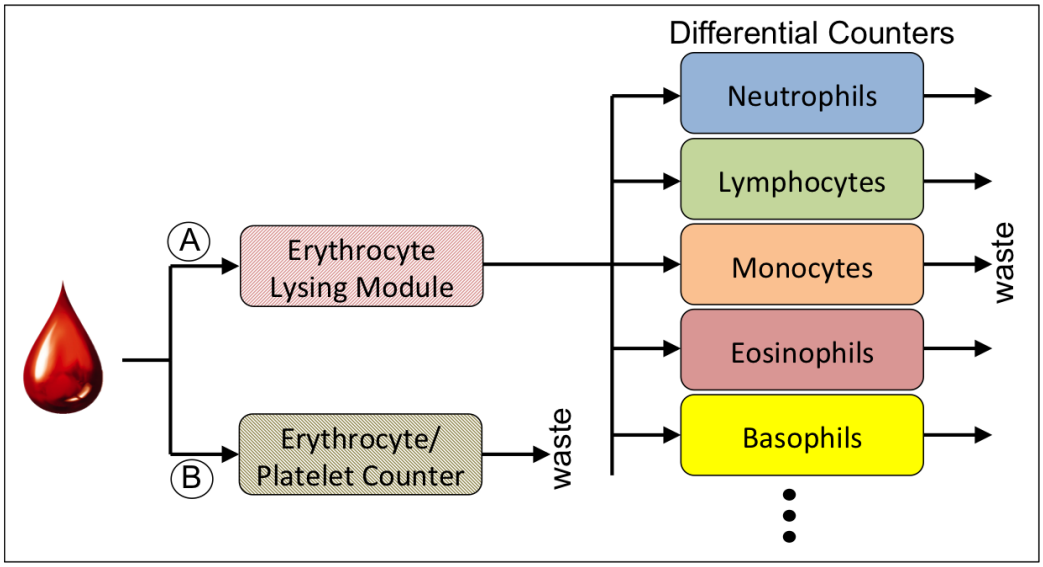

Figure 6.3: Concept of CBC on a chip using the electrical differential counting technique. Whole blood samples are split between two branches. Branch A performs erythrocyte lysis and subsequent differential counts of leukocyte subsets. Branch B dilutes the blood sample to count the erythrocytes and platelets. Modified from [156]. © 2011 IEEE.

sophils) simply from the forward (entrance) counts.

The first major step to realize and test the feasibility of this concept is to start with analyzing two cell types simultaneously. CD4+ T lymphocytes and CD8+ T lymphocytes (suppressor T cells) were chosen, as their counts and ratio are also an important HIV/AIDS diagnostic. Figure 6.4 shows an actual mask design that will be used to create the fluidics and electrical sensing components of the CD4/CD8 chip. The same lysis and quenching methods would be used as described in Chapter 5. After quenching, the purified leukocyte population would be split between two separate counter and capture chamber networks. One set of capture chambers would be coated with CD4 antibodies, while the other would be coated with CD8 antibodies.

The branching mechanism may create extra counting error if downstream fluidic resistances are not identical between the two counter/capture networks. This non-ideal situation would cause the flow to split unevenly between the two branches, resulting in counting error because the assumption that identical sample volumes were analyzed by each counter would not be true.

On-chip flow rate metering can be used to compensate for this error by

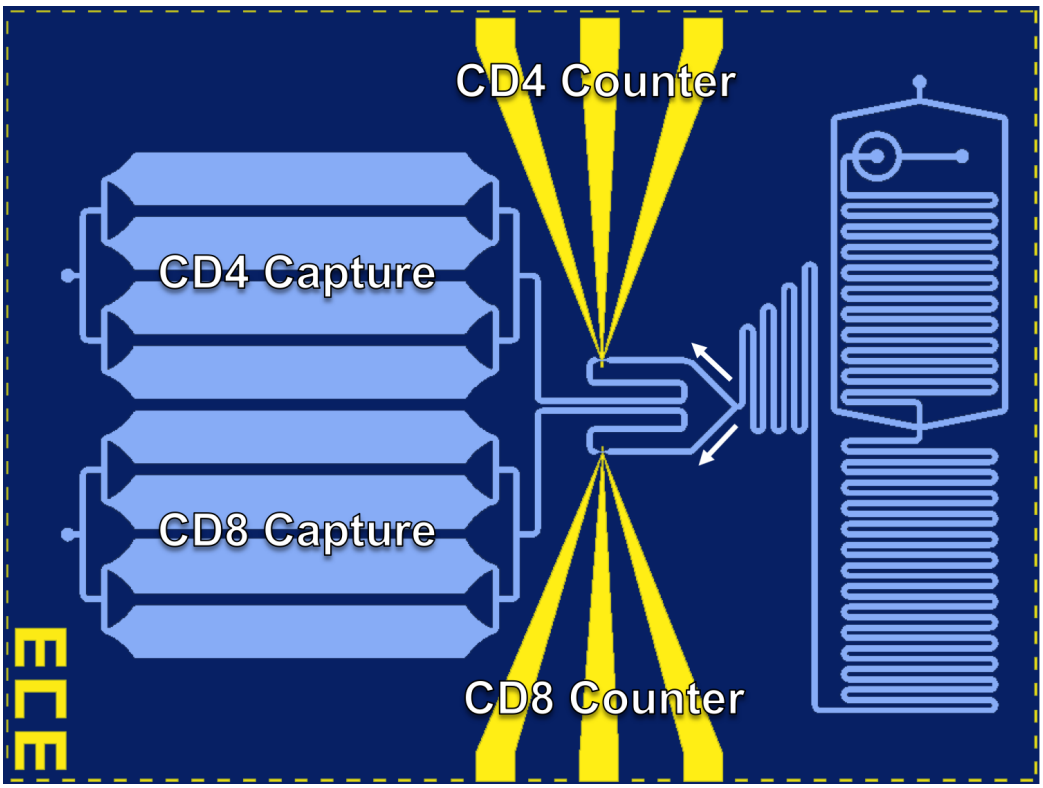

Figure 6.4: CD4/CD8 differential counter design. Whole blood samples undergo the same on-chip erythrocyte lysis and quenching steps before equally splitting the flow between two separate counters and capture chamber networks. The chip's dimensions are 3 cm x 4 cm.

determining the ratio of flow rates between the two networks in addition to how much sample volume was flown through each counter. Collins and Lee have shown that the admittance across microfabricated electrodes in microfluidic channels for ionic solutions varies linearly with flow rate [157]. We used the configuration shown in Fig. 6.5(a) to simultaneously count leukocytes and measure flow rate after on-chip lysing and quenching. Figure 6.5(b) verifies this linear relationship, suggesting that this method can be used to compensate for the aforementioned flow error and provide accurate CD4/CD8 counts.

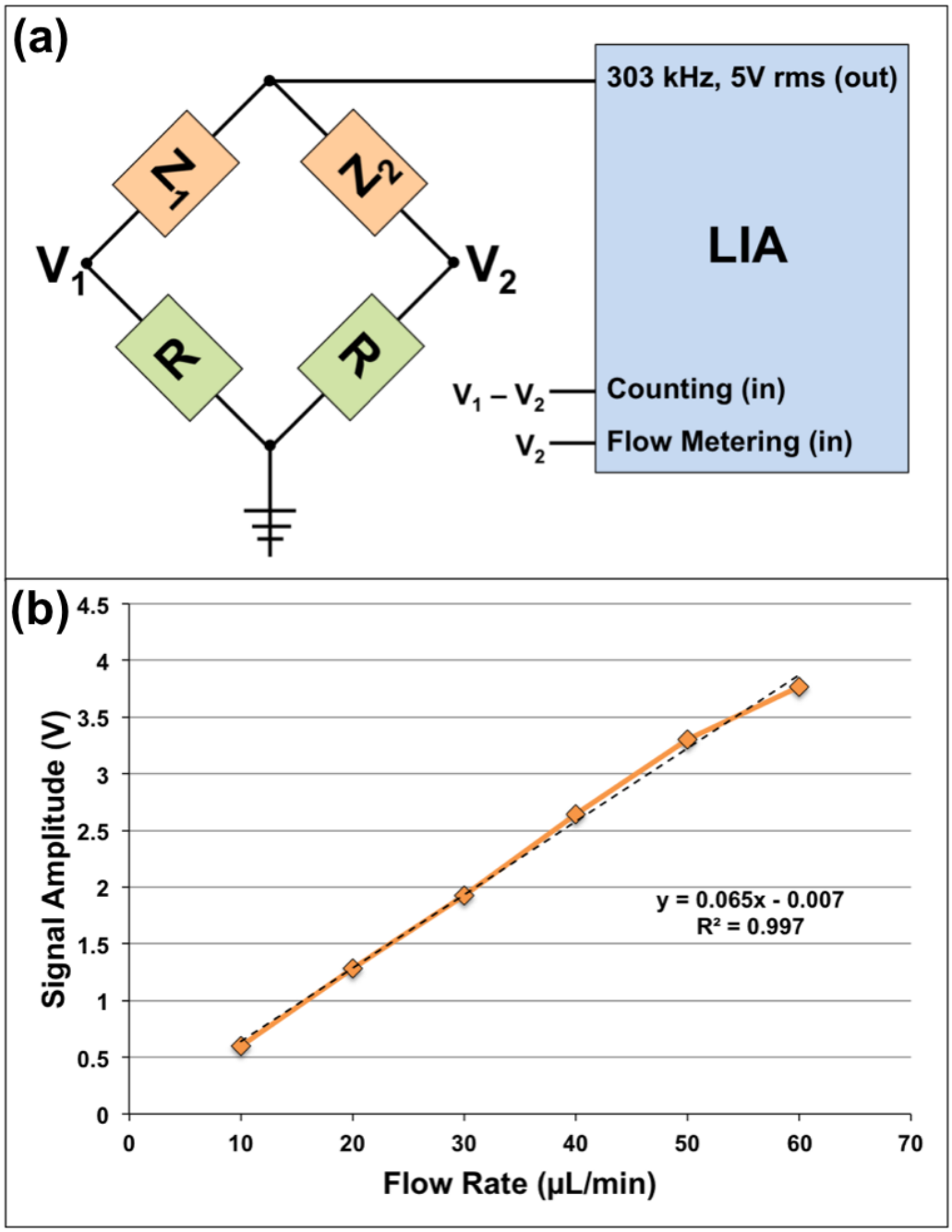

Figure 6.5: (a) Electrical configuration to simultaneously count cells and measure volumetric flow rate. (b) Comparison between the voltage of V_2 and known flow rates. The relationship is linear, as shown by the linear regression statistics (dashed line, $R^2 = 0.997$).

APPENDIX A

ELECTRICAL PARAMETER EXTRACTION OF BIOLOGICAL CELLS

Pauly and Schwan's investigations into the dielectric properties of cellular suspensions have led to the following equations which can be used to estimate the cellular dispersion phenomena [96,103,158]. This was accomplished using Maxwell-Wagner mixture equations assuming a single shell, non-conducting membrane model [159, 160]:

$$\epsilon_0 = \frac{1 - p/2}{1 + p} + \left(\frac{9}{8\epsilon_r}\right)\left(\frac{p}{p+1}\right) DC_M \tag{A.1}$$

$$\epsilon_\infty = \epsilon_1 \frac{(1+2p)\epsilon_2 + 2(1-p)\epsilon_1}{(1-p)\epsilon_2 + (2+p)\epsilon_1} \tag{A.2}$$

$$\sigma_0 = \sigma_1 \left(\frac{1-p}{1+p/2}\right) \tag{A.3}$$

$$\sigma_\infty = \sigma_1 \frac{1 + 2p(\sigma_2 - \sigma_1)/(\sigma_2 + 2\sigma_1)}{1 - p(\sigma_2 - \sigma_1)/(\sigma_2 + 2\sigma_1)} \tag{A.4}$$

ϵ_0 and σ_0 are the permittivities and conductivities measured at the low frequency limit and ϵ_∞ and σ_∞ are the permittivities and conductivities measured at the high frequency limit, respectively. ϵ_r is vacuum permittivity (8.85 x 10^{-14} F/cm), p is the volume fraction of the cells, D is the cell diameter, and C_M is the cell membrane capacitance. ϵ_1 and σ_1 are the permittivities and conductivities of the suspension media, respectively.

These foundational relationships can be used to obtain the cytoplasm permittivity (ϵ_2) and conductivity (σ_2) [103, 145, 161]:

$$\epsilon_2 = \epsilon_1 \frac{(-2+p)\epsilon_1 + (2+p)\epsilon_\infty}{(1+2p)\epsilon_1 - (1-p)\epsilon_\infty} \tag{A.5}$$

$$\sigma_2 = \frac{(2+p)^2(\sigma_\infty - \sigma_1)}{(1+2p)(2+p) - 2(1-p)^2(\sigma_\infty/\sigma_1)} \tag{A.6}$$

The membrance capacitance can also be extracted; using the Hanai-Asami-Koizumi mixture equation [145, 162]:

$$C_M \cong \frac{2}{3}\frac{\epsilon_r}{R}\frac{\epsilon_0}{1-(1-p)^{3/2}} \tag{A.7}$$

f_c is the characteristic (or mid-point) frequency of the β-dispersion phenomenon, which is caused by the charging of the capacitive cell membrance through the cell's interior and external fluids and can be estimated as [96, 100, 163]

$$f_c = \frac{1}{\pi D C_M}\left(\frac{\sigma_1\sigma_2(2+p)}{\sigma_1(2+p) + \sigma_2(1-p)}\right) \tag{A.8}$$

Qualitatively, at low frequencies, the cell's membrane can polarize in enough time to create a counter field to the externally applied field, effectively shielding the cell's inner contents. As the applied frequency is increased, the membrane's charge/discharge response begins to lag, and eventually fails to keep up with the external field. As in the case of a capacitor at high frequencies, the membrane's reactance becomes negligible and is effectively shunted. This allows the total potential to be across the cell's cytoplasm, effectively polarizing its nuclear envelope and organelles. At even higher frequencies, the nuclear envelope itself is shunted, resulting in another dispersion, and the nucleus is electrically interrogated [164]. Therefore, it is possible to electrically interrogate different components of a cell simply by varying the applied frequency.

In addition, f_c can be used to find the effective permittivity (ϵ) and conductivity (σ) of the entire cell (combined membrane and cytoplasm) for an arbitrary frequency:

$$\epsilon = \epsilon_\infty + \frac{\epsilon_0 - \epsilon_\infty}{1 + (f/f_c)^2} \tag{A.9}$$

$$\sigma = \sigma_\infty + \frac{\sigma_0 - \sigma_\infty}{1 + (f/f_c)^2} \tag{A.10}$$

REFERENCES

[1] UNAIDS, "AIDS Epidemic Update," November 2009. [Online]. Available: http://data.unaids.org/pub/Report/2009/2009_epidemic_update_en.pdf

[2] W. H. Organization, "The global shortage of health workers and its impact," April 2006. [Online]. Available: http://www.who.int/mediacentre/factsheets/fs302/en/index.html

[3] G. Flechet, "Sub-Saharan Africa: the population emergency," January 2008. [Online]. Available: http://www.eurekalert.org/pub_releases/2008-01/idrp-sat010808.php#

[4] M. Kitahata, S. Gange, A. Abraham, B. Merriman, M. Saag, A. Justice, R. Hogg, S. Deeks, J. Eron, J. Brooks, S. Rourke, M. Gill, R. Bosch, J. Martin, M. Klein, L. Jacobson, B. Rodriguez, T. Sterling, G. Kirk, S. Napravnik, A. Rachlis, L. Calzavara, M. Horgerg, M. Silverberg, K. Gebo, J. Goedert, C. Benson, A. Collier, S. V. Rompaey, H. Crane, R. McKaig, B. Lau, A. Freeman, and R. Moore, "Effect of early versus deferred antiretroviral therapy for hiv on survival," *The New England Journal of Medicine*, vol. 360, pp. 1815–1826, 2009.

[5] P. Severe, M. Juste, A. Ambroise, L. Eliacin, C. Marchand, S. Apollon, A. Edwards, H. Bang, J. Nicotera, C. Godfrey, M. Gulick, J. W. Johnson, J. Pape, and D. Fitzgerald, "Early versus standard antiretroviral therapy for hiv-infected adults in haiti," *The New England Journal of Medicine*, vol. 363, pp. 257–265, 2010.

[6] World Health Organization and United Nations Children's Fund and UNAIDS, "Towards universal access: scaling up priority HIV/AIDS interventions in the health sector. Progress report 2009," Geneva, World Health Organization, 2009.

[7] A. Phillips, C. Lee, J. Elford, G. Janossy, A. Timms, M. Bofill, and P. Kernoff, "Serial CD4 lymphocyte counts and development of AIDS," *Lancet*, vol. 337, pp. 389–392, 1991.

[8] V. Miller, S. Staszewski, C. Sabin, A. Carlebach, C. Rottmann, E. Weidmann, H. Rabenau, A. Hill, A. Lepri, and A. Phillips, "Cd4 lymphocyte count as a predictor of the duration of highly active antiretroviral therapy–induced suppression of human immunodeficiency virus load," *The Journal of Infectious Diseases*, vol. 180, pp. 530–533, 1999.

[9] A. Lepri, A. Phillips, A. Monforte, F. Castelli, A. Antinori, A. de Luca, P. Pezzotti, F. Alberici, A. Cargnel, P. Grima, R. Piscopo, T. Prestileo, G. Scalise, M. Vigevani, and M. Moroni, "When to start highly active antiretroviral therapy in chronically hiv-infected patients: evidence from the icona study," *AIDS*, vol. 15, pp. 983–990, 2001.

[10] R. Tirumalai, K. Chan, D. Prieto, H. Issaq, T. Conrads, and T. Veenstra, "Characterization of the low molecular weight human serum proteome," *Molecular and Cellular Proteomics*, vol. 2, pp. 1096–1103, 2003.

[11] B. Alberts, A. Johnson, J. Lewis, M. Raff, K. Roberts, and P. Walter, *Molecular Biology of the Cell*, 4th ed. New York: Garland Science, 2002.

[12] V. Daniels, P. Wheater, and H. Burkitt, *Functional Histology: A Text and Colour Atlas*. Churchill Livingstone, 1979.

[13] N. Campbell and J. Reece, *Biology*, 8th ed. London: Benjamin Cummings, 2008.

[14] B. Liang, "White blood cells," 2010. [Online]. Available: http://www.wisc-online.com/objects/ViewObject.aspx?ID=AP14704

[15] K. Saizawa, J. Rojo, and C. Janeway, Jr., "Evidence for a physical association of CD4 and the CD3:alpha:beta T-cell receptor," *Nature*, vol. 328, pp. 260–263, 1987.

[16] J. Reeves and R. Doms, "Human immunodeficiency virus type 2," *Journal of General Virology*, vol. 83, pp. 1253–1265, 2002.

[17] D. Chan and P. Kim, "Hiv entry and its inhibition," *Cell*, vol. 93, pp. 681–684, May 1998.

[18] R. Wyatt and J. Sodroski, "The HIV-1 Envelope Glycoproteins: Fusogens, Antigens, and Immunogens," *Science*, vol. 280, p. 1884, 1998.

[19] Y.-H. Zheng, N. Lovsin, and B. Peterlin, "Newly identified host factors modulate HIV replication," *Immunology Letters*, vol. 97, pp. 225–234, 2005.

[20] "Wikimedia commons: Hiv_gross.png," April 2010. [Online]. Available: http://commons.wikimedia.org/wiki/File:Hiv_gross.png#filelinks

[21] Centers for Disease Control and Prevention, "1993 Revised Classification System for HIV Infection and Expanded Surveillance Case Definition for AIDS Among Adolescents and Adults," December 1992. [Online]. Available: http://www.cdc.gov/mmwr/preview/mmwrhtml/00018871.htm

[22] BBC News, "Home HIV help 'could save lives'," February 2008. [Online]. Available: http://news.bbc.co.uk/2/hi/health/7269780.stm

[23] G. Pantaleo, C. Graziosi, and A. Fauci, "New concepts in the immunopathogenesis of human immunodeficiency virus infection," *The New England Journal of Medicine*, vol. 328, pp. 327–335, February 1993.

[24] Lab Tests Online, "HIV Antibody," April 2010. [Online]. Available: http://www.labtestsonline.org/understanding/analytes/hiv_antibody/multiprint.html

[25] J. Mulder, N. McKinney, C. Christopherson, J. Sninsky, L. Greenfield, and S. Kwok, "Rapid and Simple PCR Assay for Quantitation of Human Immunodeficiency Virus Type 1 RNA in Plasma: Application to Acute Retroviral Infection," *Journal of Clinical Microbiology*, vol. 32, no. 2, pp. 292–300, February 1994.

[26] B. van Gemen, T. Kievits, R. Schukkink, D. van Strijp, L. Malek, R. Sooknanan, H. Huisman, and P. Lens, "Quantification of HIV-1 RNA in plasma using NASBA during HIV-1 primary infection," *Journal of Virological Methods*, vol. 43, no. 2, pp. 177–187, July 1993.

[27] M. Segondy, T.-D. Ly, M. Lapeyre, and B. Montes, "Evaluation of the Nuclisens HIV-1 QT Assay for Quantitation of Human Immunodeficiency Virus Type 1 RNA Levels in Plasma," *Journal of Clinical Microbiology*, vol. 36, no. 11, pp. 3372–3374, November 1998.

[28] D. Kern, M. Collins, T. Fultz, J. Detmer, S. Hamren, J. Peterkin, P. Sheridan, M. Urdea, R. White, T. Yeghiazarian, and J. Todd, "An enhanced-sensitivity branched-DNA assay for quantification of human immunodeficiency virus type 1 RNA in plasma," *Journal of Clinical Microbiology*, vol. 34, no. 12, pp. 3196–3202, December 1996.

[29] J. Yao, Z. Liu, L.-S. Ko, G. Pan, and Y. Jiang, "Quantitative detection of hiv-1 rna using nuclisens easyq hiv-1 assay," *Journal of Virological Methods*, vol. 129, pp. 40–46, 2005.

[30] A. Calmy, N. Ford, B. Hirschel, S. Reynolds, L. Lynen, E. Goemaere, F. Garcia de la Vega, L. Perrin, and W. Rodriguez, "HIV Viral Load Monitoring in Resource-Limited Regions: Optional or Necessary?" *Clinical Infectious Diseases*, vol. 44, no. 1, pp. 139–140, January 2007.

[31] J. Parker, "Flow cytometry," in *Hematology, Clinical and Laboratory Practice*. St. Louis: Mosby, 1993, vol. 1, pp. 121 – 133.

[32] G. Marowsky, G. Cornelius, and L. Rensing, "Laser-induced fluorescence studies of intact biological membranes," *Optics Communications*, vol. 22, no. 3, pp. 361 – 364, September 1977.

[33] C. Sacchi, "Laser induced fluorescence of biomolecules," *Optics Communications*, vol. 18, no. 1, p. 141, 1976.

[34] A. Artyunyan, E. Docchio, R. Ramponi, C. Sacchi, G. Bottiroli, and I. Freitas, "Laser-induced fluorescent microscopy: investigation of the interaction of hematoporphyrin derivatives with cells," *Bulletin of the Academy of Sciences of the USSR, Physical Series*, vol. 47, no. 12, pp. 155 – 159, 1983.

[35] R. Alfano, D. Tata, J. Cordero, P. Tomashefsky, F. Longo, and M. Alfano, "Laser induced fluorescence spectroscopy from native cancerous and normal tissue," *IEEE Journal of Quantum Electronics*, vol. 20, no. 12, pp. 1507 – 1511, 1984.

[36] Invitrogen, "Flow cytometry tutorials: Introduction," April 2010. [Online]. Available: http://probes.invitrogen.com/resources/education/tutorials/4Intro_Flow/player.html

[37] S. Crowe, S. Turnbull, R. Oelrichs, and A. Dunne., "Monitoring of human immunodeficiency virus infection in resource-constrained countries," *Clinical Infectious Diseases*, vol. 37, pp. S25–S35, 2003.

[38] M. Fryland, P. Chaillet, R. Zachariah, A. Barnaba, L. Bonte, R. Andereassen, S. Charrondière, R. Teck, and O. Didakus, "The Partec CyFlow Counter® could provide an option for CD4+ T-cell monitoring in the context of scaling-up antiretroviral treatment at the district level in Malawi," *Transactions of the Royal Society of Tropical Medicine and Hygiene*, vol. 100, pp. 980–985, 2006.

[39] K. Srithanaviboonchai, K. Rungruengthanakit, P. Nouanthong, S. Pata, T. Sirisanthana, and W. Kasinrerk, "Novel low-cost assay for the monitoring of CD4 counts in HIV-infected individuals," *J. Acquir. Immune Defic. Syndr.*, vol. 47, no. 2, pp. 135–9, February 2008.

[40] F. Lutwama, R. Serwadda, H. Mayanja-Kizza, H. Shihab, A. Ronald, M. Kamya, D. Thomas, E. Johnson, T. Quinn, R. Moore, and L. Spacek, "Evaluation of Dynabeads and Cytospheres compared with flow cytometry to enumerate CD4+ T cells in HIV-infected Ugandans on antiretroviral therapy," *J. Acquir. Immune Defic. Syndr.*, vol. 48, no. 3, pp. 297–303, July 2008.

[41] J. Holman, *Heat Transfer*, 9th ed. McGraw-Hill, 2002.

[42] M. Unger, H.-P. Chou, T. Thorsen, A. Scherer, and S. Quake, "Monolithic microfabricated valves and pumps by multilayer soft lithography," *Science*, vol. 288, pp. 113–116, April 2000.

[43] T. Thorsen, S. Maerkl, and S. Quake, "Microfluidic large-scale integration," *Science*, vol. 298, pp. 580–584, October 2002.

[44] R. Balagaddé, L. You, C. Hansen, F. Arnold, and S. Quake, "Long-term monitoring of bacteria undergoing programmed population control in a microchemostat," *Science*, vol. 309, pp. 137–140, July 2005.

[45] S. Bae, H. Park, J. Oh, S.-Y. Yoon, D. Park, I. Choi, J. Kim, J. Oh, D. Hur, C. Chung, J. Chang, J. Robinson, and C. Lim, "Absolute CD4+ Cell Count Using a Plastic Microchip and a Microscopic Cell Counter," *Cytometry Part B*, vol. 76B, pp. 354–353, 2009.

[46] W. Rodriguez, N. Christodoulides, P. Floriano, S. Graham, S. Mohanty, M. Dixon, M. Hsiang, T. Peter, S. Zavahir, I. Thior, D. Romanovicz, B. Bernard, A. Goodey, B. Walker, and J. McDevitt, "A Microchip CD4 Counting Method for HIV Monitoring in Resource-Poor Settings," *PLoS Medicine*, vol. 2, no. 7, pp. 663 – 672, 2005.

[47] J. Jokerst, P. Floriano, N. Christodoulides, G. Simmons, and J. McDevitt, "gration of semiconductor quantum dots into nano-bio-chip systems for enumeration of CD4+ T cell counts at the point-of-need," *Lab on a Chip*, vol. 8, pp. 2079–2090, 2008.

[48] J. Jokerst, J. Jacobson, B. Bhagwandin, P. Floriano, N. Christodoulides, and J. McDevitt, "Programmable nano-bio-chip sensors: Analytical meets clinical," *Analytical Chemistry*, vol. 82, pp. 1571–1579, 2010.

[49] X. Li, A. Ymeti, B. Lunter, C. Breukers, A. Tibbe, L. Terstappen, and J. Greve, "CD4+ T lymphocytes enumeration by an easy-to-use single platform image cytometer for HIV monitoring in resource-constrained settings," *Cytometry Part B*, vol. 72B, pp. 397–407, 2007.

[50] A. Ymeti, X. Li, B. Lunter, C. Breukers, A. Tibbe, L. Terstappen, and J. Greve, "A single platform image cytometer for resource-poor settings to monitor disease progression in HIV infection," *Cytometry Part A*, vol. 71A, pp. 132–142, 2007.

[51] X. Cheng, D. Irimia, M. Dixon, K. Sekine, U. Demirci, L. Zamir, R. Tompkins, W. Rodriguez, and M. Toner, "A microfluidic device for practical label-free CD4+ T cell counting of HIV-infected subjects," *Lab on a Chip*, vol. 7, pp. 170–178, 2007.

[52] X. Cheng, D. Irimia, M. Dixon, J. Ziperstein, U. Demirci, L. Zamir, R. Tompkins, M. Toner, and W. Rodriguez, "A microchip approach for practical label-free CD4+ T-cell counting of HIV-infected subjects in resource-poor settings," *Journal of Acquired Immune Deficiency Syndrome*, vol. 45, no. 3, pp. 257–261, 2007.

[53] X. Cheng, A. Gupta, C. Chen, R. Tompkins, W. Rodriguez, and M. Toner, "Enhancing the performance of a point-of-care CD4+ T-cell counting microchip through monocyte depletion for HIV/AIDS diagnostics," *Lab on a Chip*, vol. 9, pp. 1357–1364, 2009.

[54] M. Beck, S. Brockhuis, N. van der Velde, C. Breukers, J. Greve, and L. Terstappen, "On-chip sample preparation by controlled release of antibodies for simple CD4 counting," *Lab Chip*, vol. 12, no. 1, pp. 167–73, 2012.

[55] S. Mtapuri-Zinyowera, M. Chideme, D. Mangwanya, O. Mugurungi, S. Gudukeya, K. Hatzold, A. Mangwiro, G. Bhattacharya, J. Lehe, and T. Peter, "Evaluation of the PIMA point-of-care CD4 analyzer in VCT clinics in Zimbabwe," *J. Acquir. Immune Defic. Syndr.*, vol. 55, no. 1, pp. 1–7, 2010.

[56] I. Jani, N. Sitoe, P. Chongo, E. Alfai, J. Quevedo, O. Tobaiwa, J. Lehe, and T. Peter, "Accurate CD4 T-cell enumeration and antiretroviral drug toxicity monitoring in primary healthcare clinics using point-of-care testing," *AIDS*, vol. 25, no. 6, pp. 807–12, 2011.

[57] C. Chin, V. Linder, and S. Sia, "Commercialization of microfluidic point-of-care diagnostic devices," *Lab on a Chip*, vol. DOI: 10.1039/c2lc21204, 2012.

[58] I. Jani, N. Sitoe, J. Quevedo, J. Lehe, and T. Peter, "Cost comparison of point-of-care and laboratory CD4 testing in resource-limited settings," in *6th IAS Conference on HIV Pathogenesis, Treatment and Prevention*. Rome, Italy: International AIDS Society, 17–20 July 2011.

[59] J. Gohring and X. Fan, "Label free detection of CD4+ and CD8+ T cells using the optofluidic ring resonator," *Sensors*, vol. 10, pp. 5798–5808, 2010.

[60] S. Moon, J. Keles, A. Ozcan, A. Khademhosseini, E. Haeggstrom, D. Kuritzkes, and U. Demirci, "Integrating microfluidics and lensless imaging for point-of-care testing," *Biosensors and Bioelectronics*, vol. 24, pp. 3208–3214, 2009.

[61] Z. Wang, S. Chin, C. Chin, J. Sarik, M. Harper, J. Justman, and S. Sia, "Microfluidic CD4+ T-cell counting device using chemiluminescence-based detection," *Analytical Chemistry*, vol. 82, pp. 36–40, 2010.

[62] N. Mishra, S. Retterer, T. Zieziulewicz, M. Isaacson, D. Szarowski, D. Mousseau, D. Lawrence, and J. Tuner, "On-chip micro-biosensor for the detection of human CD4+ cells based on AC impedance and optical analysis," *Biosensors and Bioelectronics*, vol. 21, pp. 696–704, 2005.

[63] X. Jiang and M. Spencer, "Electrochemical impedance biosensor with electrode pixels for precise counting of CD4+ cells: A microchip for quantitative diagnosis of HIV infection status of AIDS patients," *Biosensors and Bioelectronics*, vol. 25, pp. 1622–1628, 2010.

[64] X. Cheng, Y.-S. Liu, D. Irimia, U. Demirci, L. Yang, L. Zamir, W. Rodriguez, M. Toner, and R. Bashir, "Cell detection counting through cell lysate impedance spectroscopy in microfluidic devices," *Lab on a Chip*, vol. 7, pp. 746 – 755, 2007.

[65] E. Altendorf, D. Zebert, M. Holl, and P. Yager, "Differential blood cell counts obtained using a microchannel based flow cytometer," in *Transducers 97. International Conference on Solid-State Sensors and Actuators*, vol. 1, 1997, pp. 531 – 534.

[66] E. Altendorf, "Microfabrication-based ektacytometer for blood cell deformability measurements," in *Proceedings of the SPIE - The International Society for Optical Engineering*, vol. 2978, 1997, pp. 136 – 144.

[67] N. Pamme, R. Koyama, and A. Manz, "Counting and sizing of particles and particle agglomerates in a microfluidic device using laser light scattering: application to a particle-enhanced immunoassay," *Lab on a Chip*, vol. 3, pp. 187 – 192, 2003.

[68] C.-H. Lin and G.-B. Lee, "Micromachined flow cytometers with embedded etched optic fibers for optical detection," *Journal of Micromechanics and Microengineering*, vol. 13, pp. 447 – 453, 2003.

[69] R. Applegate, Jr., J. Squier, T. Vestad, J. Oakey, D. Marr, P. Bado, M. Dugan, and A. Said, "Microfluidic sorting system based on optical waveguide integration and diode laser bar trapping," *Lab on a Chip*, vol. 6, pp. 422 – 426, 2006.

[70] S.-Y. Yang, S.-K. Hsiung, Y.-C. Hung, C.-M. Chang, T.-L. Liao, and G.-B. Lee, "A cell counting/sorting system incorporated with a microfabricated flow cytometer chip," *Measurement Science and Technology*, vol. 17, pp. 2001 – 2009, 2006.

[71] R. Bernini, E. De Nuccio, F. Brescia, A. Minardo, L. Zeni, P. Sarro, R. Palumbo, and M. Scarfi, "Development and characterization of an

integrated silicon micro flow cytometer," *Analytical and Bioanalytical Chemistry*, vol. 386, pp. 1267 –1272, 2006.

[72] J. Krüger, K. Singh, A. O'Neill, C. Jackson, A. Morrison, and P. O'Brien, "Development of a microfluidic device for fluorescent activated cell sorting," *Journal of Micromechanics and Microengineering*, vol. 12, pp. 486 – 494, 2002.

[73] A. Fu, C. Spence, A. Scherer, F. Arnold, and S. Quake, "A microfabricated fluorescence-activated cell sorter," *Nature Biotechnology*, vol. 17, no. 11, pp. 1109 – 1111, 1999.

[74] B. Yao, G.-A. Luo, X. Feng, W. Wang, L.-X. Chen, and Y.-M. Wang, "A microfluidic device based on gravity and electric force driving for flow cytometry and fluorescence activated cell sorting," *Lab on a Chip*, vol. 4, pp. 603 – 607, 2004.

[75] D. Holmes, H. Morgan, and N. Green, "High throughput particle analysis: Combining dielectrophoretic particle focussing with confocal optical detection," *Biosensors and Bioelectronics*, vol. 21, pp. 1621 – 1630, 2006.

[76] T. Arakawa, Y. Shirasaki, T. Izumi, T. Aoki, H. Sugino, T. Funatsu, and S. Shoji, "High-speed particles and biomolecules sorting microsystem using thermosensitive hydrogel," *Measurement Science and Technology*, vol. 17, pp. 3141 – 3146, 2006.

[77] A. Wolff, I. Perch-Nielsen, U. Larsen, P. Friis, G. Goranovic, C. Poulsen, J. Kutter, and P. Telleman, "Integrating advanced functionality in a microfabricated high-throughput fluorescent-activated cell sorter," *Lab on a Chip*, vol. 3, pp. 22 – 27, 2003.

[78] H. Bang, C. Chung, J. Kim, S. Kim, S. Chung, J. Park, W. Lee, H. Yun, J. Lee, K. Cho, D.-C. Han, and J. Chang, "Microfabricated fluorescence-activated cell sorter through hydrodynamic flow manipulation," *Microsystems Technology*, vol. 12, pp. 746 – 753, 2006.

[79] X. Mao, S.-C. S. Lin, C. Dong, and T. J. Huang, "Single-layer planar on-chip flow cytometer using microfluidic drifting based three-dimensional (3d) hydrodynamic focusing," *Lab on a Chip*, vol. 9, pp. 1583–1589, 2009.

[80] Y.-C. Tung, M. Zhang, C.-T. Lin, K. Kurabayashi, and S. Skerlos, "PDMS-based opto-fluidic micro flow cytometer with two-color, multi-angle fluorescence detection capability using PIN photodiodes," *Sensors and Actuators B: Chemical*, vol. 98, pp. 356 – 367, 2004.

[81] H. Chen and Y. Wang, "Optical microflow cytometer for particle counting, sizing and fluorescence detection," *Microfluidics and Nanofluidics*, vol. 6, pp. 529–537, 2009.

[82] S. Son, Y. Choi, and S. Lee, "Micro-cell counter using photoconductance of boron diffused resistor (BDR)," *Sensors and Actuators A: Physical*, vol. 111, pp. 100 – 106, 2004.

[83] C.-C. Lin, A. Chen, and C.-H. Lin, "Microfluidic cell counter/sorter utilizing multiple particle tracing technique and optically switching approach," *Biomedical Microdevices*, vol. 10, pp. 55–63, 2008.

[84] K.-I. Inatomi, S.-I. Izuo, and S.-S. Lee, "Application of a microfluidic device for counting of bacteria," *Letters in Applied Microbiology*, vol. 40, pp. 296 – 300, 2006.

[85] K. Takahashi, A. Hattori, I. Suzuki, T. Ichiki, and K. Yasuda, "Non-destructive on-chip cell sorting system with real-time microscopic image processing," *Journal of Nanobiotechnology*, vol. 2, no. 5, 2004.

[86] J.-H. Wang, C.-H. Wang, C.-C. Lin, H.-Y. Lei, and G.-B. Lee, "An integrated microfluidic system for counting of cd4(+)/cd8(+) t lymphocytes," *Microfluidics and Nanofluidics*, vol. 10, no. 3, pp. 531–541, Mar. 2011.

[87] W. H. Coulter, "Means for counting particles suspended in a fluid," U.S. Patent no. 2,656,508, October 1953.

[88] M. Koch, A. Evans, and A. Brunnschweiler, "Design and fabrication of a micromachined coulter counter," *Journal of Micromechanics and Microengineering*, vol. 9, pp. 159 – 161, 1999.

[89] J. Hu and J. Zhe, "Coulter counter having a plurality of channels," U.S. Patent no. 7,397,232, 2008.

[90] M. Graham, "The coulter principle: Foundation of an industry," *Journal of the Association for Laboratory Automation*, vol. 8, no. 6, pp. 72–81, 2003.

[91] K. Roberts, M. Parameswaran, M. Moore, and R. Muller, "A silicon microfabricated aperture for counting cells using hte aperture impedance technique," in *Proceedings of the 1999 IEEE Canadian Conference on Electrical and Computer Engineering*, Edmonton, Alberta, Canada, May 1999, pp. 1668–1673.

[92] D. Satake, H. Ebi, N. Oku, K. Matsuda, H. Takao, M. Ashiki, and M. Ishida, "A sensor for blood cell counter using mems technology," *Sensors and Actuators B: Chemical*, vol. 83, pp. 77 – 81, 2002.

[93] D. Lee, S. Yi, and Y.-H. Cho, "A flow rate independent cell concentration measurement chip using electrical cell counters across a fixed control volume," *Journal of Microelectromechanical Systems*, vol. 17, no. 1, pp. 139–146, 2008.

[94] H. Chun, T. Chung, and H. Kim, "Cytometry microchip using polymer-based saltbridge electrodes," in *Proceedings of the 26th Annual International Conference of the IEEE EMBS*, San Francisco, CA, September 2004, pp. 2584–2586.

[95] H. Schwan, "Electrical Properties of Tissue and Cell Suspensions" in Advances in Biological and Medical Physics. New York: Academic, 1957, vol. 5, pp. 147–209.

[96] H. Pauly and H. Schwan, "Über die impedanz einer suspension von kugelförmigen teilchen mit einer schale," *Zeitschrift für Naturforschung B - A Journal of Chemical Sciences*, vol. 14b, pp. 125–131, 1959.

[97] H. Schwan, G. Schwarz, J. Maczuk, and H. Pauly, "On the low frequency dielectric dispersion of colloidal particles in electrolyte solution," *The Journal of Physical Chemistry*, vol. 66, no. 12, pp. 2626–2635, 1962.

[98] H. Schwan, "Electrical properties of bound water," *Annals of the New York Academy of Sciences*, vol. 125, no. 2, pp. 344–354, 1965.

[99] H. Scwhan, "Electrical properties of blood and its consituents: Alternating current spectroscopy," *Blut*, vol. 46, pp. 185–197, 1983.

[100] H. Schwan, "Analysis of dielectric data: Experience gained with biological materials," *IEEE Transactions on Electrical Insulation*, vol. EI-20, no. 6, pp. 913–922, December 1985.

[101] E. Grant, N. Nightingale, R. Sheppard, and S. Gough, *Biological Effects of Nonionizing Radiation*, ser. ACS Symposium Series. American Chemical Society, 1981, ch. 3.

[102] W. Coulter and W. Hogg, "Signal modulated apparatus for generating and detecting resistance and reactive changes in a modulated current passed for particle classification and analysis," U.S. Patent no. 3,502,974, 1970.

[103] R. Hoffman and W. Britt, "Flow-system measurement of cell impedance properties," *Journal of Histochemistry and Cytochemistry*, vol. 27, no. 1, pp. 234–240, 1979.

[104] R. Hoffman, T. Johnson, and W. Britt, "Flow cytometric electronic direct current volume and radiofrequency impedance measurments of single cells and particles," *Cytometry*, vol. 1, no. 6, pp. 377–384, 1981.

[105] T. Sun, D. Holmes, S. Gawad, N. Green, and H. Morgan, "High speed multi-frequency impedance analysis of single particles in a microfluidic cytometer using maximum length sequences," *Lab on a Chip*, vol. 7, pp. 1034 – 1040, 2007.

[106] B. Hart and R. Peekema, "Electrochemical double layer capacitor," U.S. Patent no. 3,652,902, March 1972.

[107] S. Gawad, L. Schild, and P. Renaud, "Micromachined impedance spectroscopy flow cytometer for cell analysis and particle sizing," *Lab on a Chip*, vol. 1, pp. 76 – 82, 2001.

[108] R. Gómez-Sjöberg, "Microfabricated device for impedance-based electronic detectionof bacterial metabolism," Ph.D. dissertation, Purdue University, West Lafayette, IN, December 2003.

[109] A. Bard and L. Faulkner, *Electrochemical Methods*, 2nd ed. John Wiley & Sons, Inc., 2001.

[110] K. Cheung, S. Gawad, and P. Renaud, "Impedance spectroscopy flow cytometry: On-chip label-free cell differentiation," *Cytometry Part A*, vol. 65A, pp. 124 – 132, 2005.

[111] C. Küttel, E. Nascimento, N. Demierre, T. Silva, T. Braschler, P. Renaud, and A. Oliva, "Label-free detection of *Babesia bovis* infected red blood cells using impedance spectroscopy on a microfabricated cytometer," *Acta Tropica*, vol. 102, pp. 63–68, 2007.

[112] A. Pierzchalski, M. Hebeisen, A. Mittag, M. D. Berardino, and A. Tárnok, "Label-free single cell analysis with a chip-based impedance flow cytometer," in *SPIE - International Society for Optics and Photonics*, San Francisco, CA, 2010, pp. 75 861B–11.

[113] G. Schade-Kampmann, A. Huwiler, M. Hebeisen, and M. D. Berardino, "On-chip non-invasive and label-free cell discrimination by impedance spectroscopy," *Cell Proliferation*, vol. 41, no. 5, pp. 830–840, October 2008.

[114] K. Cheung, M. D. Berardino, G. Schade-Kampmann, M. Hebeisen, A. Pierzchalski, J. Bocsi, A. Mittag, and A. Tárnok, "Microfluidic impedance-based flow cytometry," *Cytometry Part A*, vol. 77A, no. 7, pp. 648–666, 2010.

[115] L. Sohn, O. Saleh, G. Facer, A. Beavis, R. Allan, and D. Notterman, "Capacitance cytometry: Measuring biological cells one by one," *PNAS*, vol. 97, no. 20, pp. 10 687 – 10 690, 2000.

[116] G. Benazzi, D. Holmes, T. Sun, M. Mowlem, and H. Morgan, "Discrimination and analysis of phytoplankton using a microfluidic cytometer," *IET Nanobiotechnology*, vol. 1, pp. 94–101, 2007.

[117] D. Holmes, D. Pettigrew, C. Reccius, J. Gwyer, C. van Berkel, J. Holloway, D. Davies, and H. Morgan, "Leukocyte analysis and differentiation using high speed microfluidic single cell impedance cytometry," *Lab on a Chip*, vol. 9, pp. 2881–2889, 2009.

[118] C. van Berkel, J. Gwyer, S. Deane, N. Green, J. Holloway, V. Hollis, and H. Morgan, "Integrated systems for rapid point of care (PoC) blood cell analysis," *Lab on a Chip*, vol. 11, pp. 1249–1255, 2011.

[119] Y. Wang, Y. Kang, D. Xu, C. Chon, L. Barnett, S. Kalams, D. Li, and D. Li, "On-chip counting the number and the percentage of CD4+ T lymphocytes," *Lab on a Chip*, vol. 8, pp. 309–315, 2008.

[120] X. Wu, Y. Kang, Y. Wang, D. Xu, D. Li, and D. Li, "Microfluidic differential resistive pulse sensors," *Electrophoresis*, vol. 29, no. 13, pp. 2754–2759, 2008.

[121] X. Wu, C. Chon, Y. Wang, Y. Kang, and D. Li, "Simultaneous particle counting and detecting on a chip," *Lab on a Chip*, vol. 8, pp. 1943–1949, 2008.

[122] D. Holmes and H. Morgan, "Single cell impedance cytometry for identification and counting of CD4 T-cells in human blood using impedance labels," *Analytical Chemistry*, vol. 82, pp. 1455–1461, 2010.

[123] A. Carbonaro, S. Mohanty, H. Huang, L. Godley, and L. Sohn, "Cell characterization using a protein-functionalized pore," *Lab on a Chip*, vol. 8, pp. 1478–1485, 2008.

[124] A. Adams, P. Okagbare, J. Feng, M. Hupert, D. P. adn J. Gottert, R. McCarley, D. Nikitopoulos, M. Murphy, and S. Soper, "Highly efficient circulating tumor cell isolation from whole blood and label-free enumeration using polymer-based microfluidics with an integrated conductivity sensor," *Journal of the American Chemical Society*, vol. 130, pp. 8633–8641, 2008.

[125] H. Zhu, J. Yan, and A. Revzin, "Catch and release cell sorting: Electrochemical desorption of t-cells from antibody-modified microelectrodes," *Colloids and Surfaces B: Biointerfaces*, vol. 64, pp. 260–268, 2008.

[126] J. Robertus, W. Browne, and B. Feringa, "Dynamic control over cell adhesive properties using molecular-based surface engineering strategies," *Chemical Society Reviews*, vol. 39, pp. 354–378, 2010.

[127] U. Gurkan, T. Anand, H. Tas, D. Elkan, A. Akay, H. Keles, and U. Demirci, "Controlled viable release of selectively captured label-free cells in microchannels," *Lab Chip*, vol. 11, no. 23, pp. 3979–89, Dec 2011.

[128] C. Willyard, "Simpler tests for immune cells could transform AIDS care in Africa," *Nature Medicine*, vol. 13, no. 10, p. 1131, Oct 2007.

[129] D. S. D. Boyle, K. R. Hawkins, M. S. Steele, M. Singhal, and X. Cheng, "Emerging technologies for point-of-care CD4 T-lymphocyte counting," *Trends Biotechnol*, vol. 30, no. 1, pp. 45–54, Jan 2012.

[130] World Health Organization, "Antiretroviral therapy for HIV infection in adults and adolescents: recommendations for a public health approach." March 2010. [Online]. Available: http://whqlibdoc.who.int/publications/2010/9789241599764_eng.pdf

[131] R. Zachariah, S. Reid, P. Chaillet, M. Massaquoi, E. Schouten, and A. Harries, "Viewpoint: Why do we need a point-of-care CD4 test for low-income countries?" *Tropical Medicine & International Health*, vol. 16, no. 1, pp. 37–41, Jan. 2011.

[132] H. Morgan, T. Sun, D. Holmes, S. Gawad, and N. Green, "Single cell dielectric spectroscopy," *Journal of Physics D: Applied Physics*, vol. 40, pp. 61 – 70, 2007.

[133] N. Watkins, B. Venkatesan, M. Toner, W. Rodriguez, and R. Bashir, "A robust electrical microcytometer with 3-dimensional hydrofocusing," *Lab on a Chip*, vol. 9, pp. 3177–3184, November 2009.

[134] H. Shapiro, *Practical Flow Cytometry*, 4th ed. John Wiley & Sons, Inc., 2003.

[135] K. Tang, E. Liao, W. Ong, J. Wong, and A. Agarwal, "Evaluation of bonding between oxygen plasma treated polydimethyl siloxane and passivated silicon," *Journal of Physics: Conference Series*, vol. 34, pp. 155 – 161, 2006.

[136] K. Davis, B. Abrams, S. Iyer, R. Hoffman, and J. Bishop, "Determination of CD4 antigen density on cells: Role of antibody valency, avidity, clones, and conjugation," *Cytometry*, vol. 33, pp. 197–205, 1998.

[137] B. Lee, M. Sharron, L. Montaner, D. Weissman, and R. Doms, "Quantification of CD4, CCR5, and CXCR4 levels on lymphocyte subsets, dendritic cells, and differentially conditioned-derived macrophages," *Proceedings of the National Academy of Sciences of the United States of America*, vol. 96, pp. 5215–5220, April 1999.

[138] H. Morgan, D. Holmes, and N. Green, "High speed simultaneous single particle impedance and fluorescence analysis on a chip," *Current Applied Physics*, vol. 6, no. 3, pp. 367–370, June 2006.

[139] N. Watkins, S. Sridhar, X. Cheng, G. Chen, M. Toner, W. Rodriguez, and R. Bashir, "A microfabricated electrical differential counter for the selective enumeration of CD4+ T lymphocytes," *Lab on a Chip*, vol. 11, pp. 1437–1447, 2011.

[140] B. Young and J. Heath, *Wheater's Functional Histology: A Text and Colour Atlas*, 4th ed. Edinburgh: Churchill Livingstone, 2000.

[141] S. Usami, H.-H. Chen, Y. Zhao, S. Chien, and R. Skalak, "Design and construction of a linear shear stress flow chamber," *Annals of Biomedical Engineering*, vol. 21, no. 1, pp. 77–83, January 1993.

[142] N. Freeman, L. Peel, M. Swann, G. Cross, A. Reeves, S. Brand, and J. Lu, "Real time, high resolution studies of protein adsorption and structure at the solid–liquid interface real time, high resolution studies of protein adsorption and structure at the solid-liquid interface using dual polarization interferometry," *Journal of Physics: Condensed Matter*, vol. 16, pp. S2493–S2496, 2004.

[143] S. Ledis, H. Crews, T. Fischer, and T. Sena, "Lysing reagent system for isolation, identification and/or analysis of leukocytes from whole blood samples," U.S. Patent no. 5,155,044, October 1992.

[144] S. Zuckerman, S. Ackerman, and S. Douglas, "Long-term human peripheral blood monocyte cultures: establishment, metabolism and morphology of primary human monocyte-macrophage cell cultures," *Immunology*, vol. 38, no. 2, pp. 401–11, Oct 1979.

[145] S. Gawad, K. Cheung, U. Seger, A. Bertsch, and P. Renaud, "Dielectric spectroscopy in a micromachined flow cytometer: theoretical and practical considerations," *Lab on a Chip*, vol. 4, pp. 241 – 251, 2004.

[146] N. Li, H. Tang, H. Gai, X. Dong, Q. Wang, and E. Yeung, "Determination of protein surface excess on a liquid/solid interface by single-molecule counting," *Analytical and Bioanalytical Chemistry*, vol. 394, pp. 1879–1885, 2009.

[147] M. Jacob, M. Favre, and J.-C. Bensa, "Membrane cell permeabilization with saponin and multiparametric analysis by flow cytometry," *Cytometry*, vol. 12, no. 6, pp. 550–558, 1991.

[148] B. Wang, A. Weldon, P. K. an dB. Xu, J. Gilchrist, and X. Cheng, "Effect of surface nanotopography on immunoaffinity cell capture in microfluidic devices," *Langmuir*, vol. 27, pp. 11 229–11 237, 2011.

[149] S. Mastoravich, J. Zhang, S. Nicholson-Dykstra, S. Linder, W. Friedrich, K. Siminovitch, and H. Higgs, "Lymphocyte microvilli are dynamic, actin-dependent structures that do not require wiskott-aldrich syndrome protein (wasp) for their morphology," *Blood*, vol. 104, no. 5, pp. 1396–1403, 2004.

[150] K. Rigg, B. Shenton, I. Murray, A. Givan, R. Taylor, and T. Lennard, "A flow cytometric technique for simultaneous analysis of human mononuclear cell surface antigens and DNA," *Journal of Immunological Methods*, vol. 123, pp. 177–184, 1989.

[151] E. Sollier, N. Rostaing, P. Pouteau, Y. Fouillet, and J.-L. Achard, "Passive microfluidic devices for plasma extraction from whole human blood," *Sensors and Actuators B: Chemical*, vol. 141, no. 2, pp. 617–624, 2009.

[152] A. Zipursky, E. Bow, R. Seshadri, and E. Brown, "Leukocyte density and volume in normal subjects and in patients with acute lymphoblastic leukemia," *Blood*, vol. 48, pp. 361–371, 1976.

[153] S. Nagrath, L. Sequist, S. Maheswaran, D. Bell, D. Irimia, L. Ulkus, M. Smith, E. Kwak, S. Digumarthy, A. M. adn P. Ryan, U. Balis, R. Tompkins, D. Haber, and M. Toner, "Isolation of rare circulating tumour cells in cancer patients by microchip technology," *Nature*, vol. 450, pp. 1235–1239, 2007.

[154] S. Murthy, A. Sin, R. Tompkins, and M. Toner, "Effect of flow and surface conditions on human lymphocyte isolation using microfluidic chambers," *Langmuir*, vol. 20, no. 26, pp. 11 649–11 655, November 2004.

[155] S. Stott, C.-H. Hsu, D. Tsukrov, M. Yu, D. Miyamoto, B. Waltman, S. Rothenberg, A. Shah, M. Smas, G. Korir, J. F. Floyd, A. A. Gilman, J. Lord, D. Winokur, S. Springer, D. Irimia, S. Nagrath, L. Sequist, R. Lee, K. Isselbacher, S. Maheswaran, D. Haber, and M. Toner, "Isolation of circulating tumor cells using a microvortex-generating herringbone-chip," *Proceedings of the National Academy of Sciences of the United States of America*, vol. 107, no. 43, pp. 18 392–18 397, Oct. 2010.

[156] N. Watkins, D. Irimia, M. Toner, and R. Bashir, "On a chip," *IEEE Pulse*, vol. 2, no. 6, pp. 19–27, November 2011.

[157] J. Collins and A. Lee, "Microfluidic flow transducer based on the measurement of electrical admittance," *Lab on a Chip*, vol. 4, pp. 7–10, 2004.

[158] H. Pauly, "Über di elektrische kapazität der zellmembran und di leitfähigkeit des zytoplasmas von ehrlich-aszitestumorzellen," *Biophysik*, vol. 1, pp. 143–153, 1963.

[159] J. Maxwell, *A Treatise on Electricity and Magnetism*, 3rd ed. New York: Dover, 1891, vol. 1.

[160] K. Wagner, "Erklärung der dielektrischen nachwirkungsvorgänge auf grund maxwellscher vorstellungen," *Archiv fur Elektrotechnik*, vol. 2, no. 9, pp. 371–387, September 1914.

[161] R. Fomekong, U. Pliquett, and F. Pliquett, "Passive electrical properties of RBC suspensions: changes due to distribution of relaxation time in dependence on the cell volume fraction and medium conductivity," *Bioelectrochemistry and Bioenergetics*, vol. 47, pp. 81–88, 1998.

[162] K. Asami, Y. Takahashi, and S. Takashima, "Frequency domain analysis of membrane capacitance of cultured cells (hela and myeloma) using the micropipette technique." *Biophysical Journal*, vol. 58, no. 1, pp. 143–148, July 1990.

[163] T. Hanai, "Electrial Properties of Emulsions," *in Emulsion Science*. London-New York: Academic Press, 1968, pp. 353–478.

[164] C. Polk and E. Postow, *Handbook of Biological Effects of Electromagnetic Fields*, 2nd ed. Boca Raton, FL: CRC Press LLC, 1996.